UNIVERSITÀ
DI PAVIA

Dipartimento di Biologia e Biotecnologie

“Lazzaro Spallanzani”

Laurea Magistralis in Molecular Biology and Genetics

Fondazione Salvatore Maugeri IRCCS

Computational and biochemical characterization of the C-terminal tail of cardiac CASQ unveils its regulatory role in the Ca^{2+}-dependent assembly

Supervisor:

Prof.ssa Silvia Giuliana Priori

Co-supervisors:

Dott.ssa Chiara Marabelli

Prof. Alfonso Gautieri

Experimental thesis by

Emanuele Pirana

Academic year 2025/2026

Abstract

Cardiac Calsequestrin (CASQ2) is the principal Ca^{2+}-buffering protein of the junctional sarcoplasmic reticulum (jSR) of cardiomyocytes, where it undergoes Ca^{2+}-dependent polymerization and contributes to the regulation of ryanodine receptor 2 (RyR2) gating. Mutations in CASQ2 cause Catecholaminergic Polymorphic Ventricular Tachycardia type 2 (CPVT2), a lethal inherited arrhythmia. The key domain determining CASQ2 Ca^{2+}-dependent behaviour is the C-terminal intrinsically disordered region (IDR), the acidic DEX^{n}-motif, which structure could not be determined by crystallography and whose functional role has remained poorly defined. This thesis investigated how CASQ2 C-terminal tail responds to the multi-ionic environment of the jSR, which contains, in addition to Ca^{2+} that fluctuates (between 0.3 and 1.5 mM) with each contraction, high concentrations of K^{+} (140 – 220 mM) and a stable pool of free Mg^{2+} (0.8 – 1 mM). The work combined in vitro biophysical experiments on wild-type CASQ2 and two C-terminal truncation mutants, E373X (lacking the entire tail) and D383X (retaining only the proximal segment of the tail, residues 373–382), with atomistic molecular dynamics (MD) simulations of the isolated tail and of the full CASQ2 dimer.

Turbidimetric assays revealed that freshly diluted wild-type CASQ2 polymerizes rapidly and extensively in response to Ca^{2+} but progressively loses this responsiveness when allowed to equilibrate in buffer for tens of minutes before Ca^{2+} addition. This time-dependent relaxation is abolished in E373X and altered in D383X, identifying the C-terminal tail as the structural element responsible of this sensitivity to time. Dynamic light scattering confirmed that this effect occurs without any change in the oligomeric size distribution, suggesting a conformational rather than a quaternary rearrangement. A central observation was that Ca^{2+} and Mg^{2+} produce nearly indistinguishable turbidity responses in isolation yet leave the protein in profoundly different states: preincubation with Mg^{2+} preserves the fast, high-amplitude Ca^{2+} response that would otherwise be lost over time. This priming is directional and effectively irreversible, Mg^{2+} can preserve the responsive state but cannot restore it once lost and depends entirely on the presence of the C-terminal tail.

The MD simulations explained the molecular basis of these effects. Both ions are coordinated by the same distributed network of aspartate and glutamate carboxylates, confirming that CASQ2 behaves as a polyelectrolyte rather than possessing ion-selective binding pockets. However, Ca^{2+} coordinates

through inner-sphere contacts, neutralises charge efficiently, and acts as a conformational driver that directs the tail toward a defined attachment against the globular core, whereas Mg^{2+} retains its hydration shell, coordinates through longer-lived outer-sphere interactions, and acts as a conformational brake, slowing the motion of the tail roughly threefold without dictating its position. The kinetic nature of the Mg^{2+} effect was confirmed experimentally by the finding that simply lowering the temperature reproduces the Mg^{2+}-primed state. Zeta-potential measurements validated the prediction that Ca^{2+} neutralises CASQ2 more efficiently than Mg^{2+} and showed that the tail retains Mg^{2+} in low-efficiency outer-sphere interactions; intrinsic tryptophan fluorescence demonstrated that the conformational state of the tail is mechanically coupled to the structured core, moreover. it showed that immediate Ca^{2+} addition, Mg^{2+} preincubation, and cold equilibration generate assemblies sharing an equivalent denaturation profile, distinct from the relaxed buffer-equilibrated state, suggesting that ionic histories preserving the same tail conformation yield polymeric lattices of the same architecture.

Together, these findings sustain that the C-terminal IDR of CASQ2 is not a passive polyanionic scaffold but the molecular substrate of an ionic memory: K^{+} permits free conformational exploration until the energetic minimum is reached, Ca^{2+} drives the tail to an assembly-competent position, and Mg^{2+} preserves whatever conformation the tail occupies, so that the functional state of CASQ2 reflects not only which ion is present but the sequence of ionic conditions experienced. Physiologically, this suggests that the crowded, Mg^{2+}-containing environment of the jSR is functionally necessary to keep CASQ2 in a fast-responsive state: as luminal Ca^{2+} falls during systole. We hypothesize that the persistent Mg^{2+} background in the jSR would prevent CASQ2 from relaxing into a less responsive state, maintaining its readiness to respond to subsequent Ca^{2+} signals and supporting its role within the calcium release unit. By identifying the mechanism by which the C-terminal tail encodes this behaviour, this work provides a framework for understanding how disruption of the tail, through truncation or altered charge organisation rather than single residue substitutions, can compromise the controlled assembly of CASQ2 (a feature observed also through cryo-electron microscopy), and the fidelity of cardiac Ca^{2+} handling.

Riassunto

La Calsequestrina cardiaca (CASQ2) è la principale proteina adibita a tamponare le alte concentrazioni di Ca^{2+} nel reticolo sarcoplasmatico giunzionale (jSR) dei cardiomiociti, dove va incontro a polimerizzazione Ca^{2+}-dipendente e contribuisce a regolare l'apertura del recettore della rianodina di tipo 2 (RyR2). Mutazioni di CASQ2 causano la Tachicardia Ventricolare Polimorfa Catecolaminergica di tipo 2 (CPVT2), un'aritmia ereditaria potenzialmente letale. Una caratteristica distintiva di CASQ2 è la sua regione C-terminale intrinsecamente disordinata (IDR), ricca di acidi aspartici e glutammici, assente in tutte le strutture cristallografiche disponibili e dal ruolo funzionale rimasto finora poco chiaro. Questa tesi ha indagato come tale coda C-terminale risponda all'ambiente multi-ionico del jSR che contiene, oltre al Ca^{2+} che fluttua (tra 0.3 e 1.5 mM) a ogni ciclo di contrazione, elevate concentrazioni di K^{+} (140 - 220 mM) e una riserva stabile di Mg^{2+} libero (0.8 -1 mM). Il lavoro ha combinato esperimenti biofisici in vitro su CASQ2 wild-type e su due mutanti di troncamento C-terminale (E373X, privo dell'intera coda, e D383X, che conserva solo il segmento prossimale) e con simulazioni di dinamica molecolare della coda isolata e del dimero completo di CASQ2. I saggi turbidimetrici hanno mostrato che CASQ2 wild-type, appena diluita, polimerizza in modo rapido e marcato in risposta al Ca^{2+} perdendo progressivamente questa capacità di risposta se lasciata equilibrare in tampone per decine di minuti prima dell'aggiunta di Ca^{2+}. Tale rilassamento tempo-dipendente è abolito in E373X e alterato in D383X, identificando la coda C-terminale come l'elemento strutturale responsabile di questo fenomeno. Analisi granulometriche hanno confermato l'assenza di variazioni nella distribuzione dimensionale degli oligomeri, indicando un riarrangiamento conformazionale e non un cambiamento dello stato quaternario. Un risultato centrale dello studio è che Ca^{2+} e Mg^{2+} producono, se considerati singolarmente, risposte turbidimetriche pressoché indistinguibili, pur lasciando la proteina in stati profondamente diversi: l'incubazione con Mg^{2+} preserva infatti la risposta rapida e di ampia entità al Ca^{2+} che, altrimenti, andrebbe persa nel tempo. Questo effetto di nucleazione, dovuto alla capacità del Mg^{2+} di preservare lo stato reattivo della proteina appena diluita, è unidirezionale e irreversibile: una volta persa, la responsività al Ca^{2+} non può essere ripristinata e l'intero fenomeno dipende dalla presenza della coda C-terminale. Le simulazioni di dinamica molecolare hanno mostrato che entrambi gli ioni vengono coordinati dalla medesima rete diffusa di carbossilati, a conferma del fatto che CASQ2 si comporta come un polielettrolita piuttosto che come una metallo-proteina, ma interagiscono con la coda in modi

profondamente diversi. Il Ca^{2+} stabilisce contatti di coordinazione diretta, neutralizza efficacemente la carica e agisce come un vero e proprio motore conformazionale, indirizzando la coda sulla superficie laterale del dominio globulare. Il Mg^{2+}, al contrario, mantiene prevalentemente il proprio guscio di idratazione e stabilisce interazioni meno efficienti ma più durature nel tempo; il suo effetto è quello di un freno conformazionale, che rallenta di circa tre volte il movimento della coda senza determinarne la posizione, una natura cinetica, e non strutturale, confermata sperimentalmente dall'osservazione che il semplice abbassamento della temperatura riproduce lo stato indotto dal Mg^{2+}. Misure di potenziale zeta hanno confermato la maggiore efficienza del Ca^{2+} nel neutralizzare la carica di CASQ2, mostrando che la coda trattiene il Mg^{2+} in interazioni a bassa efficienza. Saggi di stabilità termica hanno infine dimostrato che lo stato conformazionale della coda è meccanicamente accoppiato al dominio strutturato della proteina, e che l'aggiunta immediata di Ca^{2+}, la pre-incubazione con Mg^{2+} e l'equilibrazione a freddo generano assemblaggi con un profilo di denaturazione equivalente, distinto da quello dello stato rilassato ottenuto per equilibrazione in tampone: ciò suggerisce che condizioni ioniche pregresse, capaci di preservare la medesima conformazione della coda, diano origine a reticoli polimerici della stessa architettura di fondo. Nel loro insieme, questi risultati stabiliscono che la regione C-terminale di CASQ2 non è un'impalcatura polianionica passiva, ma il substrato molecolare di una vera e propria memoria ionica: il K^{+} consente una libera esplorazione conformazionale della coda fino al raggiungimento del minimo energetico, il Ca^{2+} ne guida il posizionamento verso una conformazione competente per l'assemblaggio, e il Mg^{2+} preserva qualunque conformazione la coda occupi al momento del legame. Lo stato funzionale di CASQ2 riflette quindi non solo quale ione sia presente in un dato istante, ma la sequenza delle condizioni ioniche recentemente sperimentate dalla proteina. Dal punto di vista fisiologico, ciò suggerisce che l'ambiente affollato e ricco di Mg^{2+} del jSR sia funzionalmente necessario per mantenere CASQ2 pronta a rispondere al Ca^{2+}: quando, durante la sistole, il Ca^{2+} luminale diminuisce, la concentrazione di fondo persistente di Mg^{2+} impedirebbe a CASQ2 di rilassarsi in uno stato meno reattivo, sostenendo così il suo ruolo all'interno dell'unità di rilascio del calcio. Aver identificato la coda C-terminale come elemento che codifica questo comportamento fornisce un quadro per comprendere come una sua alterazione, per troncamento o per una modificata distribuzione delle cariche, piuttosto che per singole sostituzioni amminoacidiche, possa compromettere l'assemblaggio di CASQ2, come osservato anche tramite microscopia elettronica criogenica, con conseguenze sulla fedeltà della gestione e del rilascio del Ca^{2+} dal jSR.

Summary

Introduction

1.1 Calsequestrin (CASQ)

The Sarcoplasmic Reticulum (SR) is a highly specialized domain of the endoplasmic reticulum dedicated to the fine-tuned regulation of intracellular Ca^{2+} fluxes in striated muscle cells. In cardiomyocytes and skeletal muscle fibres, the SR is subdivided into two morphologically and biochemically distinct sub-compartments: the longitudinal SR (lSR) and the junctional SR (jSR). The lSR is enriched in Sarco-Endoplasmic Reticulum Ca^{2+} ATPase (SERCA) pumps, which are responsible for Ca^{2+} re-uptake from the cytosol following each contraction cycle[1,2]. The jSR constitutes the structural and functional hub for Ca^{2+} release: it hosts the Ryanodine Receptor (RyR) Ca^{2+}-release channel together with its accessory transmembrane proteins Triadin (TRDN) and Junctin (JNT), and the luminal high-capacity Ca^{2+}-binding protein Calsequestrin (CASQ). Together, these proteins constitute what is generally referred to as the Calcium Release Unit (CRU) complex[2] (Figure 1).

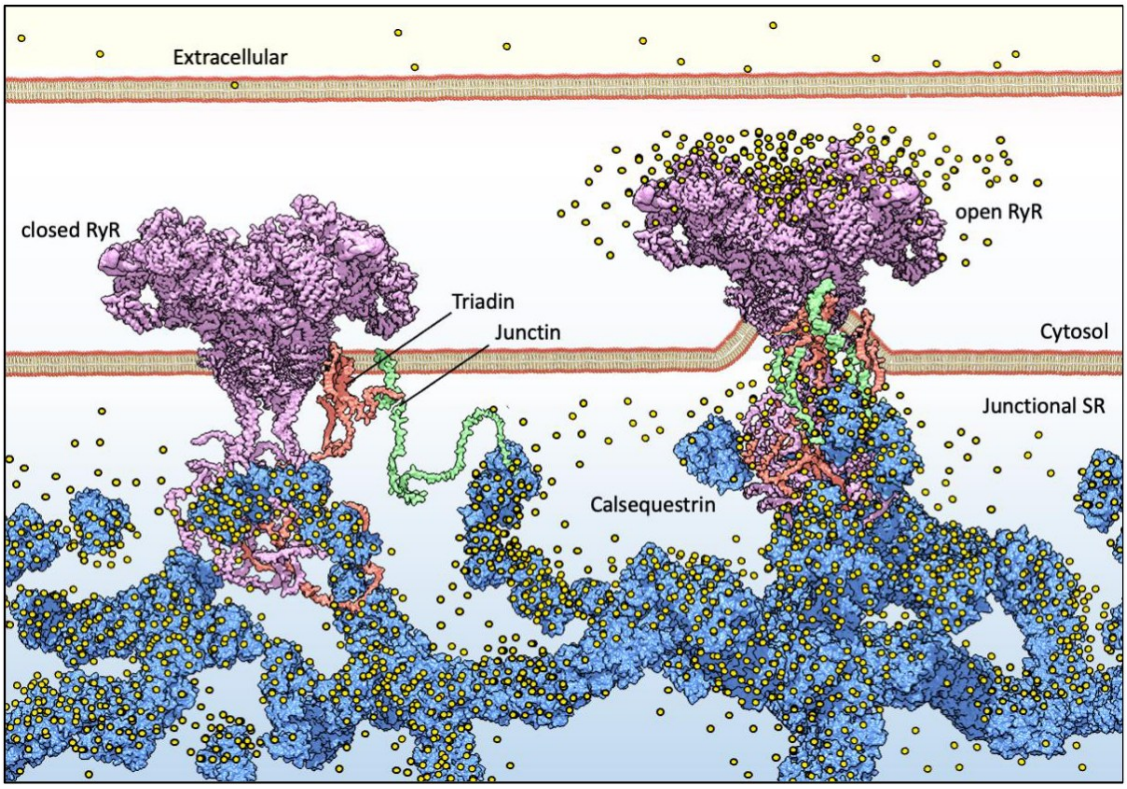

Figure 1. The Calcium Released Unit is an interconnected multiprotein complex. RyR homotetramers (pink) are anchored at the jSR membrane, while CASQ (blue) serves as the primary luminal Ca^{2+} buffer (Ca^{2+} ions shown as yellow spheres). The transmembrane proteins Junctin (green) and Triadin (red) physically tether CASQ to the RyR complex and are thought to act as signalling intermediaries between them. The precise stoichiometry of the JNT:TRDN:RyR assembly has not yet been defined.(Image taken from Marabelli et al, 2023)[2]

Calsequestrin was first isolated from skeletal muscle sarcoplasmic reticulum by MacLennan and Wong in 1971[3]. Despite its relatively modest molecular mass of approximately 45 kDa, CASQ is the most abundantly expressed protein in the lumen of the jSR, reportedly reaching concentrations of up to 100 mg/mL[4,5]. Its extraordinary local concentration, combined with its capacity to bind large quantities of Ca^{2+} with low-millimolar affinity, has led to its widely accepted characterization as the principal intracellular Ca^{2+} storage protein[2,5]. The total Ca^{2+} content within the jSR is estimated to reach up to 20 mM[6], of which 1 mM in the free form[7]. Consistent with this buffering role, studies in CASQ2 knockout mice showed a decrease of Ca^{2+} content in the jSR of roughly 50% compared to the wild-type with a structural remodelling and widening of the jSR cisterna, while changes in the SR proteome are unknown [8].

In mammals, CASQ exists as two distinct isoforms encoded by separate genes: the skeletal isoform CASQ1, predominantly expressed in fast-twitch skeletal muscle fibres, and the cardiac isoform CASQ2, which is the dominant form expressed in cardiomyocytes[9,10]. Both isoforms are co-expressed in slow-twitch skeletal muscle fibres[9]. The functional role of CASQ extends beyond simple Ca^{2+} buffering: available evidence suggests that it participates in the regulation of RyR channel gating, through modulation of luminal Ca^{2+} levels that are sensed by RyR, and through RyR regulation either indirectly, mediated by transmembrane proteins TRDN and JNT[2,11], and/or directly in contact with RyR[12]. The precise molecular basis of these direct and indirect interactions between RyR and CASQ, however, remains an active area of investigation.

The first morphological evidence for CASQ polymer formation *in situ* dates back to landmark electron microscopy studies, revealing electron-dense fibrous arrays within the jSR lumen of ventricular myocytes and skeletal muscle triads[13,14]. These structures are generally interpreted as CASQ in its Ca^{2+}-bound polymeric form, as they disassemble under extreme luminal Ca^{2+} depletion [15]. More recent freeze-fracture and rotary shadowing studies have provided additional detail on the three-dimensional organization of CASQ polymers *in situ*, revealing intricately branched and cross-linked architectures[16] (Figure 2). Notably, the loss of these luminal jSR polymeric structures characterizes certain CASQ-related pathological conditions[2,17], though the physiopathological mechanism of CASQ mutations remains unknown.

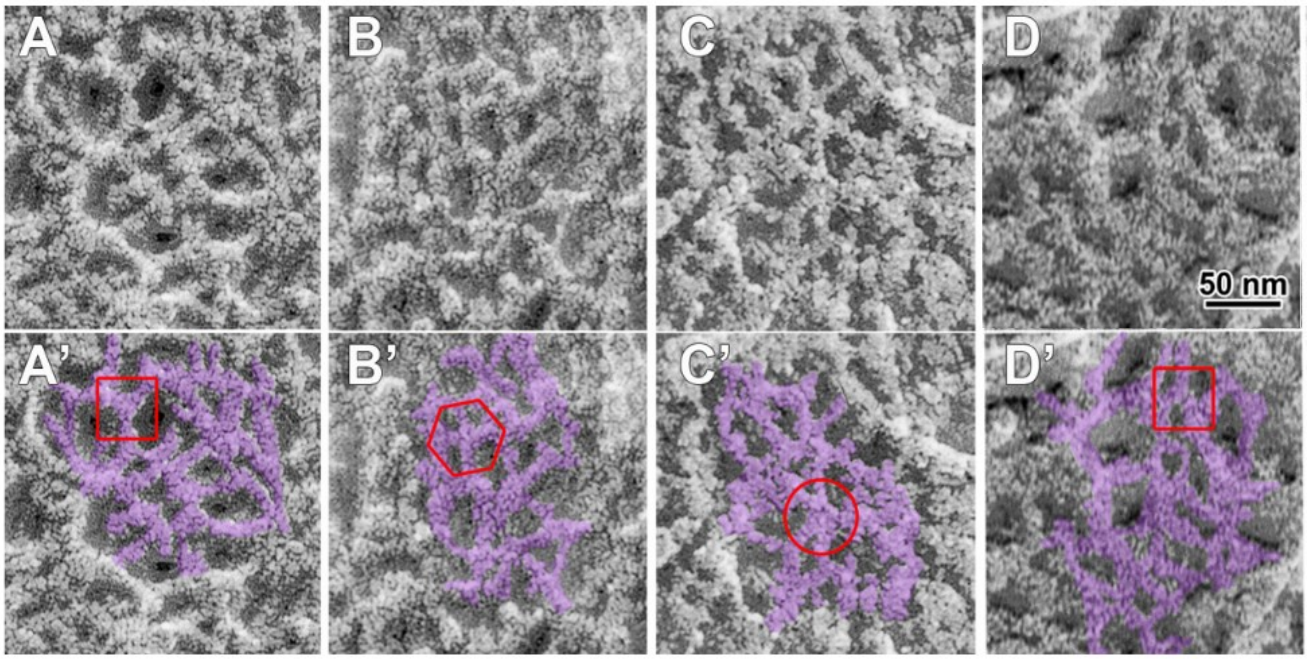

Figure 2. Three-dimensional nodal network architecture of the CASQ1 polymer in situ in snake skeletal muscle. Deep-etched rotary-shadowed freeze-fracture replicas of junctional SR from *Nerodia Sipedon* epaxial muscle, shadowed at 25°. Upper panels (A–D) show raw electron micrographs; lower panels (A'–D') show the same images with CASQ1 polymer strands highlighted in purple. The shallow shadowing angle ensures that only the most superficial layer of the fractured network is decorated, eliminating depth superimposition artefacts and confirming the reality of the nodal points. Red squares indicate tetragonal nodal configurations; red hexagons indicate trigonal configurations; red circles indicate pentagonal configurations, where four or five linear polymer segments converge on a single branching point. (Image adapted from Perni et al, 2013)[16]

1.2 CASQ in the Excitation-Contraction Coupling (ECC)

Excitation-Contraction Coupling (ECC) is the process by which an electrical stimulus at the plasma membrane is transduced into the shortening of the sarcomeres in striated muscle cells. In both cardiac and skeletal muscle, this process depends on the regulated release of Ca^{2+} from the jSR lumen to the cytosol, where it activates the actomyosin contractile machinery. The subsequent active re-sequestration of Ca^{2+} into the SR compartment by SERCA pumps restores the resting low micromolar cytosolic Ca^{2+} concentration and allows sarcomere relaxation[7]. CASQ, as the principal luminal Ca^{2+} buffer of the jSR, is a central participant in this cycle in both muscle types, providing the Ca^{2+} storage capacity that sustains repeated rounds of release[2,5,11].

The structural basis for Ca^{2+} release is a specialized membrane junction formed by the close juxtaposition of the jSR to the sarcolemma or its transverse tubule (T-tubule) invaginations, creating a micro-domain of approximately 10–20 nm distance between membranes. In skeletal muscle, this junction takes the form of a triad, with a central T-tubule flanked by two jSR terminal cisternae; in cardiac muscle, it forms a dyad, with a single jSR sac facing a single T-tubule segment[13,14]. In both cases, voltage-sensing dihydropyridine receptors (DHPRs, Cav1.1 in skeletal and Cav1.2 in cardiac

muscle) on the T-tubule membrane face RyR Ca^{2+}-release channels anchored at the jSR membrane, with CASQ forming the Ca^{2+}-buffering matrix immediately behind them in the jSR lumen[2,11,16].

Despite this shared architectural logic, the molecular trigger that links membrane depolarization to RyR opening differs fundamentally between the skeletal and cardiac muscle types. In fast-twitch skeletal muscle, Cav1.1 and RyR1 are physically coupled through a direct protein-protein interaction: membrane depolarization is transmitted to RyR1 as a conformational signal without requiring Ca^{2+} influx across the sarcolemma[18]. In this context, RyR1 opening is driven by a voltage-dependent mechanical trigger. In cardiac muscle, no equivalent direct physical coupling has been ever demonstrated between Cav1.2 and RyR2. Instead, it is generally accepted that the small Ca^{2+} influx into the dyadic cleft, determined by the voltage-dependent opening of Cav1.2, is the main trigger that activates adjacent RyR2 channels, in a process known as Ca^{2+}-Induced Ca^{2+} Release (CICR) (Figure 3)[7,11].

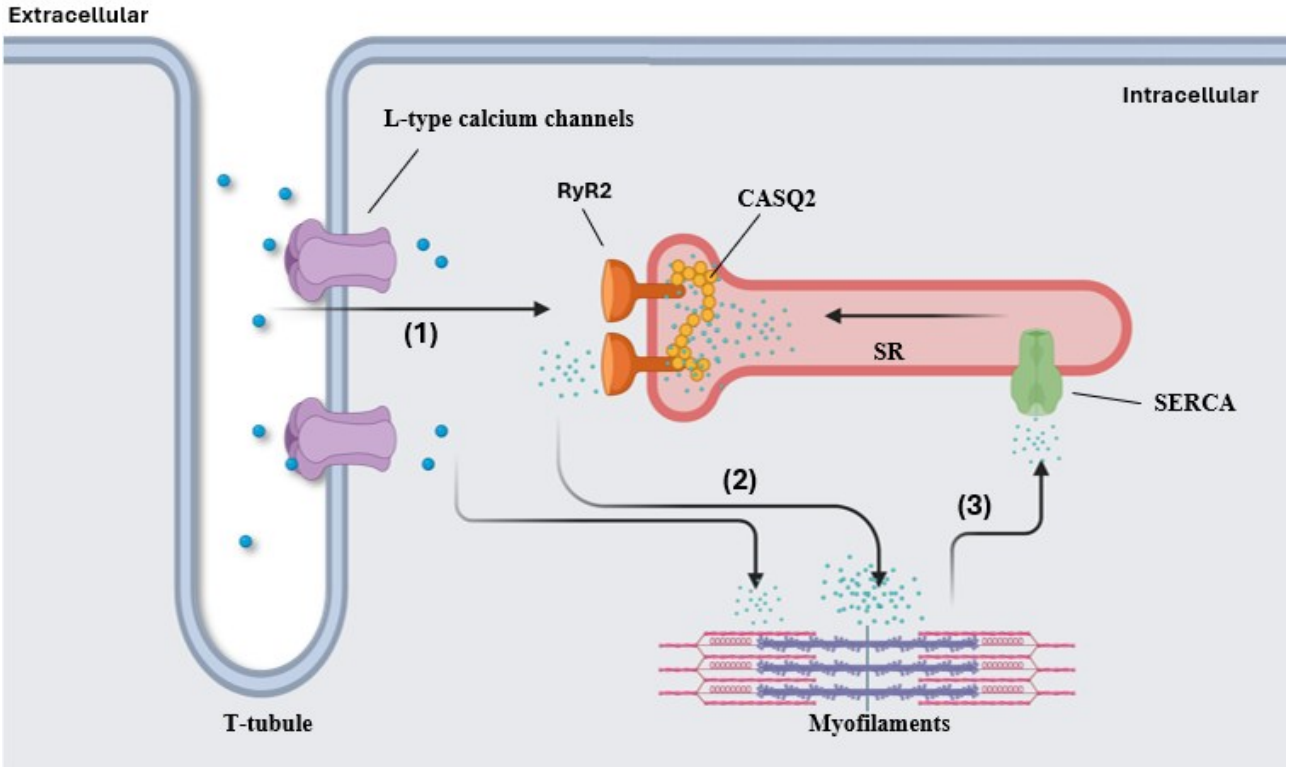

Figure 3. Schematic representation of Ca^{2+} dynamics during cardiac excitation-contraction coupling. Upon membrane depolarization, voltage-dependent opening of L-type Ca^{2+} channels (Cav1.2) generates a small Ca^{2+} influx into the dyadic cleft (1), which initiates Ca^{2+}-induced Ca^{2+} release (CICR) from the jSR lumen through RyR2 channels (2). The resulting cytosolic Ca^{2+} transient activates the contractile apparatus. Relaxation is achieved through re-uptake of cytosolic Ca^{2+} into the SR by SERCA pumps (3), with luminal Ca^{2+} subsequently buffered and stored by CASQ2, supplying the releasable pool for the following contraction cycle. (Image generated with Biorender)

The amplitude, timing, and termination of each RyR1 and RyR2 release event depend on a wealth of regulatory mechanisms converging on the channel from both cytosolic and luminal sides. Within the latter scenario, CASQ1 and CASQ2 are active participants and regulate the gain and termination of Ca^{2+} release through their interaction with the CRU[2,11,15] : it indeed determines the luminal Ca^{2+} content and how RyR senses that content, either through direct signalling interaction with RyR, and/or through RyR luminal partners TRDN and JNT.

An important and often underappreciated aspect of CASQ function in both muscle types is that the jSR lumen contains, beyond Ca^{2+}, monovalent cations, principally K^+, and the divalent cation Mg^{2+}. the amount of K^+ is estimated to fall in the 140-220 mM range, whereas free Mg^{2+} is approximately at 0.8-1 mM. Currently, there are no evidences on fluctuations of the amounts of other ions in the jSR in addition to free Ca^{2+}, which oscillates in the 0.3 to 1.5 mM range[6,19,20]. Biochemical studies have demonstrated that each CASQ isoform differently interacts with Ca^{2+} and Mg^{2+}, with a higher binding affinity for Ca^{2+} versus Mg^{2+} or K^+ but all three ions contributing to the overall ionic environment that shapes CASQ conformation and polymerization[21]. This multi-ionic character of the jSR lumen is not merely a passive backdrop: it is an active regulatory context within which CASQ must distinguish Ca^{2+} signals from the persistent Mg^{2+} and K^+ background[22].

Mutations on CASQ1 have been linked to skeletal muscle pathologies including tubular aggregate myopathy (TAM) and susceptibility to malignant hyperthermia (MH); conditions characterized by structural disorganization of the jSR, impaired Ca^{2+} buffering, and abnormal Ca^{2+} release in skeletal muscle fibres[20]. Mutations in CASQ2 are associated with Catecholaminergic Polymorphic Ventricular Tachycardia (CPVT2) that will be largely discussed in section 1.5.

1.3 CASQ biochemical features and polymerization

1.3.1 Biochemical properties

CASQ1 and CASQ2 share approximately 62% sequence identity and are closely related in their three-dimensional architecture (Figure 4A). Their sequences appear highly conserved across vertebrate species, underscoring the evolutionary importance of this protein family[2]. Both isoforms feature a central globular domain, flanked by the flexible N-terminal and C-terminal portions. The globular part is constituted by three nearly identical thioredoxin-like domains: each is composed of approximately 100 amino acid residues and organized around a hydrophobic core flanked by a five-stranded β-sheet and two pairs of α-helices[2,4].

Unlike canonical Ca^{2+}-binding proteins, CASQ possesses no EF-hand motifs or well-defined acidic Ca^{2+}-binding sites; instead, Ca^{2+} coordination is thought to arise cooperatively from the distributed network of surface carboxylates. Indeed, a defining biochemical characteristic of both CASQ isoforms is the extraordinary abundance of negatively charged acidic residues that decorate the solvent-exposed regions: glutamate (Glu) and aspartate (Asp) together constitute approximately one quarter or more of all residues, giving these proteins a very high density of surface negative charge[22] and isoelectric points of approximately 4.2 (CASQ2) and 4.0 (CASQ1) respectively[2] (Figure 4B). This electronegativity appears to be directly related to the protein's Ca^{2+}-binding capacity: published experiments show that CASQ1 can bind up to 80 Ca^{2+} ions per molecule, whereas CASQ2 up to 60, both isoforms with a moderate affinity in the low-millimolar range[2,4,23].

The folding and assembly of CASQ are profoundly sensitive to the ionic environment. Available evidence suggests that, at near-neutral pH and low ionic strength, mutual repulsion between exposed carboxylate groups causes the polypeptide to adopt an extended, disordered conformation[2]. Increasing ionic strength, whether via monovalent cations (300 mM Na^+ or K^+) or divalent ions (0.1 mM Ca^{2+}), masks these charges and promotes a more compact tertiary structure[2,22]. Ca^{2+} is roughly three orders of magnitude more efficient than monovalent cations to induce this compaction, presumably because of its strong charge density and coordination capacity[2] (Figure 4C). At higher Ca^{2+} concentrations, CASQ is thought to undergo supramolecular assembly: the traditional model proposes, as the first obligatory step, the Ca^{2+}-driven 'front-to-front' dimerization mediated by N-terminal domain swapping[2,23,24] (Figure 4D). This is followed by 'back-to-back' tetramerization and consecutively by formation of higher-order linear polymeric filaments (Figure 4E).

This Ca^{2+}-driven stepwise sequential process is derived largely from turbidimetric assays and crystallographic data[2,4,23].However, turbidimetry carries an intrinsic limitation as it measures bulk light scattering and cannot discriminate between soluble electrostatic oligomers and structured linear filaments. On the other hand, while all crystal structures of CASQ reveal the same, highly conserved dimeric structure, only one crystallographic structure shows CASQ2 quaternary assembly as a linear hexamer (three couple of dimers)[17].

A recent study by our laboratory[22] used an integrated biophysical approach combining single-particle and bulk solution measurements, to provide new evidence that substantially re-examines this classical framework. We report that, in the absence of Ca^{2+} and under physiological ionic conditions, CASQ2 dimerizes at low nanomolar concentrations. This suggests that the dimer, rather than the monomer, is the physiologically relevant Ca^{2+}-sensitive unit. Furthermore, ζ-potential measurements, a proxy of the solvent-exposed net charge, reveal that CASQ2 surface charge approaches electrical neutrality at

near-physiological K^+ concentrations (~194 mM), reframing Ca^{2+} as acting on a protein whose surface charges are already largely screened by the monovalent ionic environment of the jSR. Most conceptually significant, data on CASQ2 particle size distribution suggest that polymerization does not proceed as a gradual concentration-dependent cascade but rather as a sharp, highly cooperative switch between a pre-existing oligomeric phase and a Ca^{2+}-induced high-order polymeric phase, with important implications for understanding how CASQ2 dysfunction leads to arrhythmia (see section 1.6)[22]. Taken together, these observations lead us to propose that CASQ2 polymerization may operate as a Ca^{2+}-triggered switch between an oligomeric and a polymeric state, rather than as a stepwise concentration-dependent cascade[22].

An additional layer of complexity is provided by Mg^{2+}: the second most abundant intracellular divalent cation, maintained at approximately 0.8–1 mM free concentration in the cardiomyocyte. Available evidence indicates that Mg^{2+} reduces the number of Ca^{2+} ions bound to CASQ2[19,21], and that pre-incubation of recombinant CASQ2 with Mg^{2+} prior to Ca^{2+} addition can enhance Ca^{2+}-dependent polymerization *in vitro*. The molecular mechanism underlying this priming effect is not yet understood but may relate to the ability of Mg^{2+} to partially occupy and structurally pre-organize the flexible, charge-dense binding surfaces of CASQ2 prior to Ca^{2+}-triggered assembly[19].

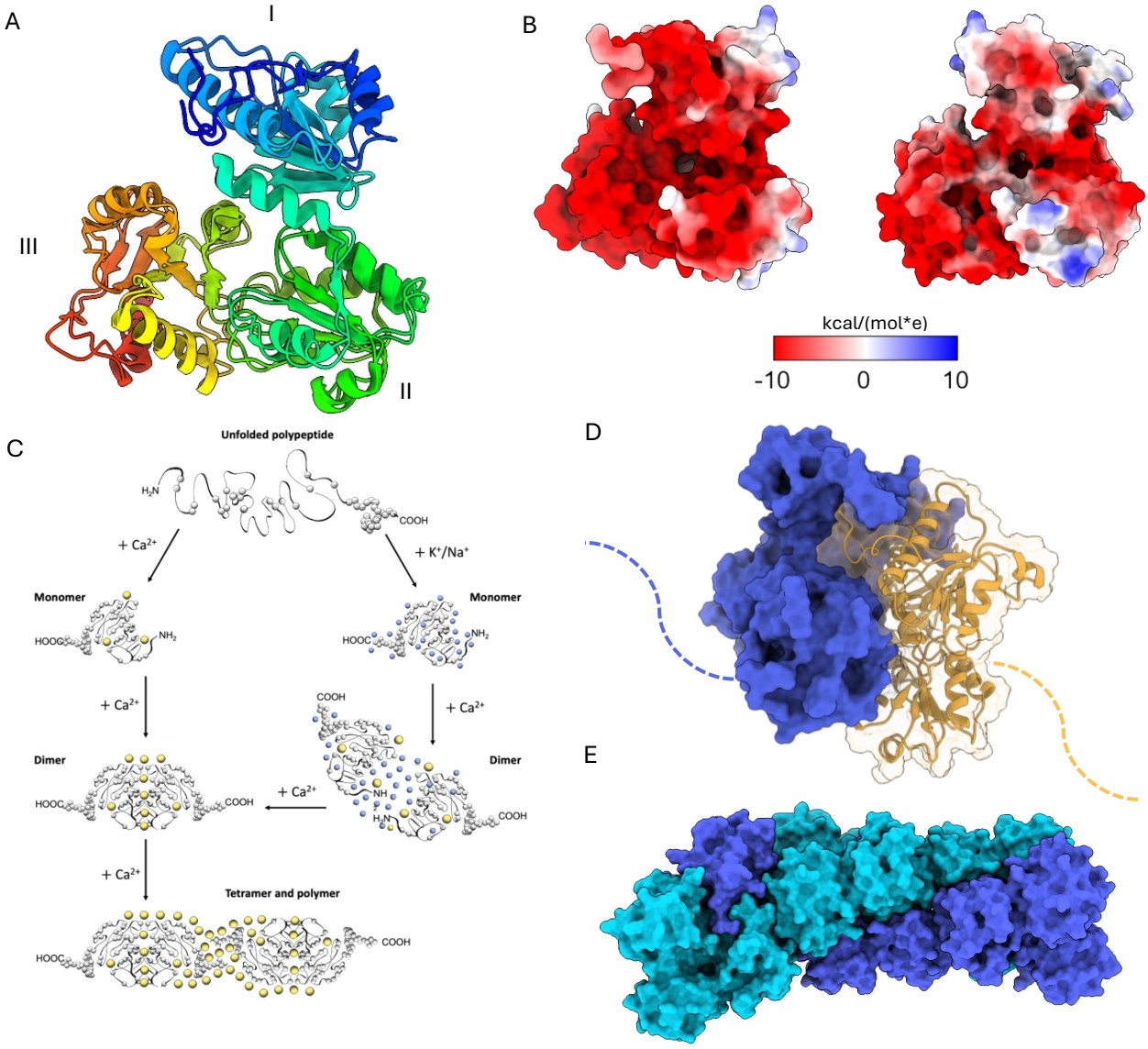

Figure 4. (A) Human CASQ2 (PDB ID: 6OWW) monomer superposed with human CASQ1 (PDB ID: 5CRD) both represented with cartoon visualization. The polypeptide is depicted in a spectrum of colours, transitioning from blue at its N-terminus to red at its C-terminus. Thioredoxin domains are indicated in roman numerals (I, II, III). (B) The surface of human CASQ1 (on the left, PDB ID: 5CRD) and CASQ2 (on the right, PDB ID: 6OWW) are represented with a colour scheme that reflects the values of the coulombic potential, as indicated by the provided colour legend. (C) Schematic of CASQ structural transitions driven by increasing ionic strength: at low ionic strength and near-neutral pH CASQ is unfolded; monovalent (Na^+/K^+) or divalent (Ca^{2+}) cations progressively induce tertiary structure compaction, with Ca^{2+} being approximately three orders of magnitude more efficient, before driving sequential front-to-front dimerization via N-terminal domain swapping and back-to-back tetramerization stabilised by C-terminal structural reorganisation.(Image taken from Marabelli et al, 2023)[2] (D) Human CASQ2 (PDB ID: 6OWW) showed in its dimeric state, the two monomers are represented with the surface and cartoon visualization to emphasize the N-terminal tail swapping of one of the two monomers on the other. The C-terminal tail is not present in the structure and is schematically represented with the dashed lines. (E) Human CASQ2 (PDB ID: 6OWV) hexamer composed of three couple of dimers. For each dimer, one monomer is coloured light blue, and the second monomer is coloured dark blue. A 90 rotation from one dimer to the adjacent one is evident along the polymer axis.

1.3.2 Post-translational modifications

Post-translational modifications (PTMs) further modulate the biochemical properties of CASQ. Both phosphorylation and N-linked glycosylation have been characterized at specific residues of both isoforms[25]. Glycosylation at Asn-316 of CASQ1 has been proposed to serve as a quality-control mechanism during ER-to-jSR trafficking, with initial bulky glycan chains potentially hindering premature multimerization, and subsequent mannose trimming in the jSR expected to restore polymerization competence[26]. Phosphorylation at Thr-353 residue by Casein Kinase 2 (CK2) or at Ser-248 and Ser-369 by the secretory pathway kinase Fam20C has been reported to increase responsiveness to Ca^{2+} of recombinant CASQ1[25,27]. Similarly, in CASQ2, the phosphorylation of Ser-385 by Fam20C and Ser-393 by Casein Kinase 2 lowers the Ca^{2+} threshold for polymerization *in vitro* and increase the Ca^{2+} binding capacity[25,27,28], though the *in vivo* physiological relevance of these modifications remains to be fully clarified. Notably, the C-terminal disordered tail, specifically for CASQ2, is a major PTM hotspot, highlighting the potentially pivotal role of this region in modulating the protein's Ca^{2+}-related properties[2].

1.4 The CASQ C-terminus tail

1.4.1 Sequence features and intrinsic disorder

Beyond the globular core, both CASQ isoforms carry a C-terminal extension that is absent from all currently resolved X-ray crystal structures, having consistently eluded electron density mapping[26]. Despite this structural inaccessibility, growing experimental evidence suggests that this region plays important roles in polymerization, Ca^{2+} sensing, and protein–protein interactions, making it a region of considerable functional interest and active investigation.

Sequence analyses reveal that the C-terminal extensions of CASQ1 and CASQ2 differ not only in length but also in amino acid composition, and this distinction appears conserved in vertebrate evolution from fish to humans[29]. In CASQ1, the C-terminus consists predominantly of aspartic acid residues (approximately 10–12 Asp residues), forming what has been designated a 'D^n-motif'. By contrast, the CASQ2 C-terminus is longer (approximately 28–30 residues) and contains acidic residues (Asp and Glu) interspersed with non-acidic residues such as asparagine (Asn), serine (Ser), and glycine (Gly), forming a 'DEX^n-motif'[29] (Figure 5A). Multiple intrinsic disorder prediction algorithms have classified both motifs as intrinsically disordered regions (IDRs), while the three

thioredoxin domains show low predicted disorder probability[29] (Figure 5B, C). The C-terminal tail is thus an IDR appended to a structured globular core.

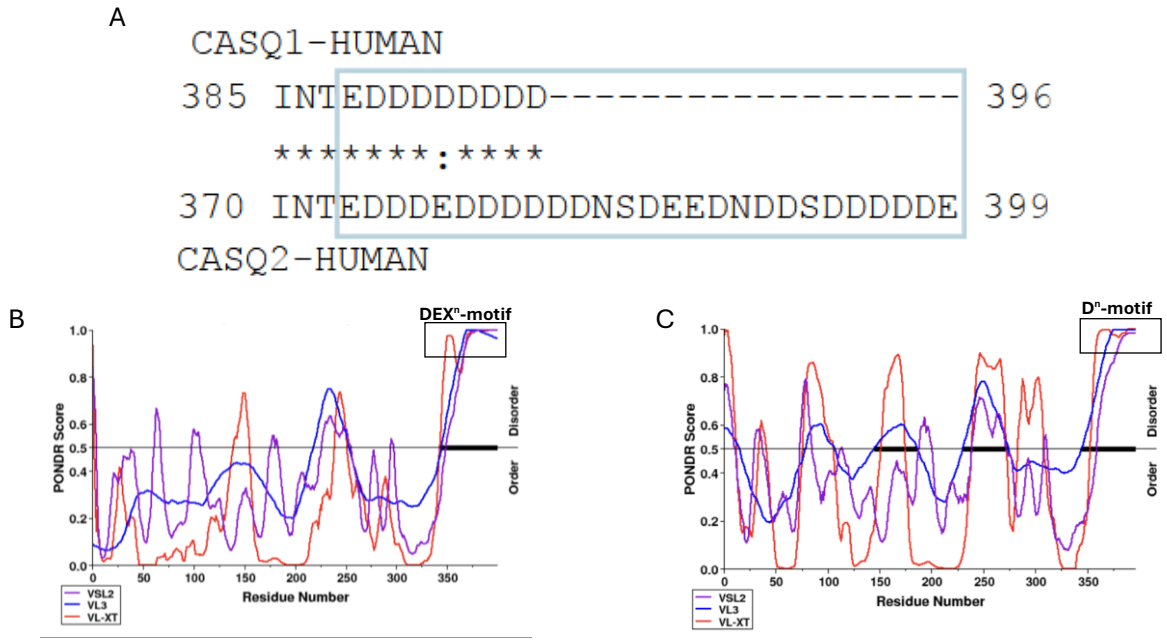

Figure 5. (A) The C-terminal Intrinsically Disordered Region is highlighted in the blue box for skeletal and cardiac CASQ isoforms. (Image taken from Marabelli et al, 2023)[2] The probability of disordered region dispersion in human CASQ2 (B) and CASQ1 (C) sequences. All the online prediction programs tested unanimously show that the C-terminus (D^n and DEX^n motifs) of CASQ isoforms are intrinsically disordered regions, while the domain I, II and III regions of either isoform show low probability of intrinsically disorderedness. (Images adapted from Bal et al, 2015)[29]

The concept of intrinsic disorder in proteins has emerged over the past two decades as a fundamental principle of protein biology. Intrinsically disordered regions (IDRs) are segments that do not adopt a single stable three-dimensional fold, but instead exist as dynamic conformational ensembles[30,31]. They are invisible to conventional structure-determination methods such as X-ray crystallography, which require a well-ordered crystal lattice. Because they escape the classical structure-function paradigm in structural biology, their functional importance was long underappreciated. It is now recognized, however, that IDRs are abundant in eukaryotic proteomes, and that their conformational flexibility endows them with unique functions in fast and non-binary processes in signalling, regulation, and molecular recognition[30–32]. As reviewed by Holehouse and Kragelund (Figure 6)[30], IDRs can mediate diverse molecular functions precisely through their structural malleability: they can adopt transient secondary structures upon binding partners (‘coupled folding and binding’), present multiple interaction surfaces simultaneously through their conformational ensemble, and respond to post-translational modifications or changes in their ionic environment in ways that a rigid folded domain could not.

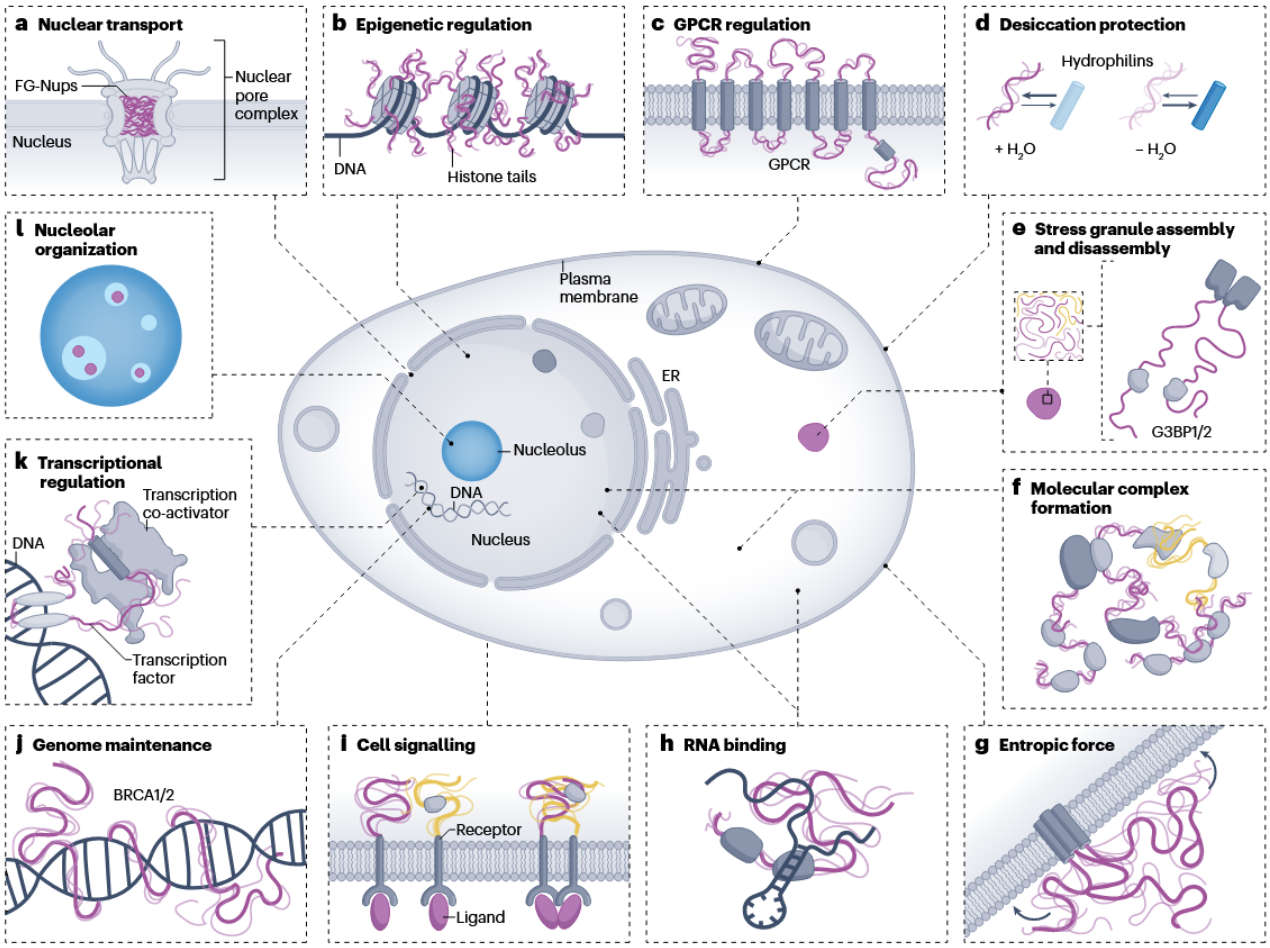

Figure 6. The diverse functional landscape of intrinsically disordered regions (IDRs) across cellular compartments. Representative examples include nuclear pore selectivity (a), histone tail-mediated epigenetic regulation (b), GPCR intracellular loops (c), desiccation resistance proteins (d), stress granule assembly (e), multidomain complex formation (f), entropic force generation at membranes (g), RNA binding (h), transmembrane receptor signalling (i), genome maintenance (j), transcriptional regulation (k), and nucleolar organization (l). (Image taken from Holehouse et al, 2024) [30]

The highly charged nature of the CASQ DEX^{n} / D^{n} motif places it in the category of 'polyelectrolyte IDRs', disordered segments whose conformational behaviour is governed primarily by charge–charge interactions rather than by hydrophobic collapse[30,32]. The conformational ensemble of such regions is expected to be strongly sensitive to ionic conditions, particularly to the concentration and valence of counterions. The charge composition of the CASQ2 DEX^{n}-motif, combining pure acidic clusters with intervening neutral residues, may also be at the origin of an important ionic discrimination function: the available evidence[22] suggests that the electrostatics of the CASQ2 C-terminal IDR integrates sensitivity to multiple ions, not only Ca^{2+} but presumably also Mg^{2+}, within the dynamics of CASQ2 monomer interactions and, expectedly, within the dynamics of CASQ2's functional interactions with the TRDN-JNT-RyR2 complex[19].

1.4.2 Role of the C-terminus in Ca^{2+}-dependent polymerization

The influence of the C-terminal IDR on polymerization kinetics was examined through chimeric protein experiments by Bal and colleagues[29]. When the C-terminal portions of CASQ1 and CASQ2 were swapped (CS-chimera: CASQ2 body + CASQ1 C-tail; SC-chimera: CASQ1 body + CASQ2 C-tail), turbidimetric assays showed a complete reversal of polymerization kinetics: the CS-chimera behaved like CASQ1 (polymerizing at lower Ca^{2+}) and the SC-chimera behaved like CASQ2 (requiring higher Ca^{2+}). Circular Dichroism (CD) spectroscopy and Molecular Dynamics (MD) simulations suggested that the overall secondary and tertiary folding of the monomeric body was not significantly altered by the chimeric swap, leading the authors to propose that the C-terminus specifically modulates the critical back-to-back tetramerization step[29]. The proposed mechanism is a 'tail-to-tail repulsion' model in which the longer and more highly charged DEX^n-motif of CASQ2 imposes a greater electrostatic barrier to back-to-back dimer approach than the shorter D^n-motif of CASQ1, until a sufficient amount of bound Ca^{2+} cations relieves this repulsion. This model remains awaits further validation, particularly at the structural level[29].

Truncation mutants of CASQ1 lacking the C-terminus have been reported to behave as constitutive dimers in solution, failing to multimerize upon Ca^{2+} addition[4], which is consistent with the important role of this segment in enabling the transition from dimer to higher-order assemblies. This observation is particularly interesting in light of the new findings from our group, which suggest that CASQ2 dimerization may itself be a Ca^{2+}-independent intrinsic property. If dimerization would not require the C-terminus, then this region may function specifically in enabling the subsequent Ca^{2+}-triggered cooperative switch to higher-order polymers. In this model, the DEX^n-motif would not act as a general Ca^{2+} sensor for all assembly steps, but rather as a specific gating element for the critical dimer-to-polymer transition[22].

The potential Ca^{2+}-sensitivity of the C-terminal IDRs was also explored by Bal and colleagues[29] using CD spectroscopy on synthetic peptides corresponding to the D^n and DEX^n motifs. The authors suggested that both motifs may undergo Ca^{2+}-induced conformational transitions, with the DEX^n-motif acquiring helical and coiled character upon Ca^{2+} addition. These observations have been widely cited as evidence that the C-terminal IDRs function as Ca^{2+}-sensing elements. It should be noted, however, that these are *in vitro* studies on isolated peptides, and it is not known whether the same conformational behaviour is recapitulated in the context of the full-length protein under physiological ionic conditions.

The CASQ2 C-terminus is also a major site of post-translational modifications that further modulates Ca^{2+} responsiveness. The DEX^n-motif of CASQ2 is reportedly phosphorylated at a markedly higher rate than the D^n-motif of CASQ1[28,33]. Phosphorylation at Ser-385 and Ser-393 by CK2 has been proposed to lower the Ca^{2+} threshold for polymerization in vitro[2,34], potentially by adding negative charges to the tail that alter its conformational response to Ca^{2+}. These observations highlight the C-terminus as a multifunctional region that integrates Ca^{2+} sensing, polymerization control, and post-translational regulation.

1.4.3 The C-terminus tail as a mediator of CRU interactions

In addition to its proposed role in polymerization, a body of evidence suggests that the C-terminal IDR may constitute an important interface mediating CASQ's interactions with the transmembrane components of the CRU: TRDN, JNT, and RyR2. It should be noted that most of this evidence was obtained with the skeletal CASQ1 isoform in reconstituted systems, and direct evidence for the same mechanism in the cardiac context has not yet been conclusively demostrated.

Early biochemical characterisations of the CASQ-TRDN interaction identified a critical binding region within the luminal domain of TRDN as the primary CASQ-binding site[35,36]. This region is characterised by the alternating arrangement of positively charged (lysine, K) and negatively charged (glutamate, E) residues, termed a 'KEKE' motif, which is thought to mediate electrostatic interactions with the complementary acidic surface of CASQ[35,36]. A similar KEKE-containing region was subsequently identified in the luminal domain of JNT[36]. A study by Shin and colleagues[37] subsequently suggested that the aspartate-rich region at the C-terminus of CASQ2 may bind Ca^{2+} and interact with TRDN. More recently, Rossi and colleagues[38] investigated the structural basis of CASQ-JNT interactions in skeletal muscle triads and identified multiple regions within JNT that drive its interaction with CASQ1, suggesting a multi-contact interaction interface.

Further support came from Beard and Dulhunty[39], who reported that C-terminal truncation of skeletal CASQ1 markedly reduced Ca^{2+}-binding capacity and abolished its inhibitory effect on the skeletal RyR in lipid bilayer experiments. These observations led to the suggestion that the C-terminus may act simultaneously as an effector domain for RyR channel regulation.

Wei and colleagues[40] demonstrated that exchanging the C-terminal portions between CASQ1 and CASQ2 switched the isoform specificity of RyR regulation: chimeric proteins bearing the C-terminal region of CASQ2 regulated RyR2 with CASQ2-like properties regardless of the globular body origin, and vice versa, establishing the C-terminal region as a primary determinant of isoform-specific functional interaction with the RyR complex. Since the C-terminal tail alone was sufficient to redirect

isoform-specific regulatory specificity regardless of the globular body origin, these findings validate the C-terminal region as the primary structural determinant of CASQ isoform-specific interaction with the RyR complex and suggest that the interaction interface is not confined to the structured globular domains alone.

A potentially important regulatory dimension is the relationship between CASQ polymerization state and the affinity between its C-terminus and the CRU. It has been proposed that CASQ2 in lower polymerization state may present a more accessible C-terminal tail and thus bind TRDN and JNT with higher affinity than polymeric CASQ2[2]. On the other hand, CASQ2 polymerization also determines CASQ2 permanence in the jSR, preventing its diffusion into the longitudinal SR[2,41]. Consistent with this, several CPVT2 mutations that impair polymerization have been reported to be associated with reduced jSR CASQ2 levels in murine models[24,42]. However, the relationships between C-terminal structure, polymerization, and jSR retention remain incompletely understood.

A particularly important and emerging property is the ability of the cardiac CRU to discriminate between luminal Ca^{2+} and Mg^{2+} at the RyR2 complex. Single-channel experiments on native and reconstituted RyR2 have identified two distinct luminal regulatory mechanisms: a RyR2-intrinsic, CASQ2-independent pathway that responds equally to luminal Ca^{2+} and Mg^{2+}, and a CASQ2-dependent pathway that specifically distinguishes between the two ions, responding to luminal Ca^{2+} but not to luminal Mg^{2+}, and that alters the cytosolic Ca^{2+} sensitivity of the channel[43]. Whether an equivalent mechanism operates at the CASQ1-RyR1 complex in skeletal muscle has not been investigated.

We propose that the C-terminal IDR of CASQ2 is the primary molecular driver of this Ca^{2+}/Mg^{2+} discriminatory interaction, given its demonstrated role in governing both Ca^{2+}-dependent polymerization and the functional interaction with the TRDN-RyR2 complex[19,29,39]. Taken together, the available evidence points to CASQ2 C-terminal IDR as a multifunctional hub at the intersection of Ca^{2+} sensing, Mg^{2+}/Ca^{2+} discrimination, polymerization cooperativity, CRU interaction, and jSR retention. In addition, CPVT2-causative missense mutations of CASQ2 are distributed across the protein's negative surface with the notable exception of the C-terminal segment[2], suggesting that this region may be under a specific selective constraint tied to its key role beyond simple Ca^{2+} buffering capacity. The poorly understood structural-dynamic properties of CASQ2 C-terminal IDR constitute the main focus of the present thesis.

1.5 Catecholaminergic Polymorphic Ventricular Tachycardia (CPVT)

Catecholaminergic Polymorphic Ventricular Tachycardia (CPVT) is a group of inherited cardiac arrhythmia syndromes characterized by the propensity to develop ventricular arrhythmia triggered by physical exercise or acute emotional stress, conditions associated with elevated circulating catecholamines. In clinical practice, the diagnosis is supported by the reproducible induction of bidirectional or polymorphic ventricular tachycardia by exercise stress testing or catecholamine infusion. Although often considered a rare condition with an estimated prevalence of approximately 1 in 10,000 individuals, accumulating evidence suggests this figure may be an underestimate, with CPVT-related gene variants potentially accounting for a significant fraction of unexplained sudden cardiac deaths in young individuals[44].

The two best-characterized genetic forms of CPVT are CPVT type 1 (CPVT1), caused by autosomal dominant gain-of-function missense variants in the *RYR2* gene, and CPVT type 2 (CPVT2), caused by variants in the *CASQ2* gene. CPVT2 was long considered exclusively autosomal recessive. However, since 2016, heterozygous CASQ2 variants have been described in patients with an autosomal dominant inheritance pattern[45]. Other rarer forms of CPVT have been attributed to mutations in genes encoding TRDN, calmodulin isoforms (*CALM1-3*), and the trans-2,3-enoyl-CoA reductase-like protein (*TECRL*)[44]. At the cellular level, CPVT arrhythmias are generally attributed to spontaneous diastolic Ca^{2+} release events that in turn generate inward transient depolarizing currents via the sarcolemma electrogenic Na^{+}/Ca^{2+} exchanger (NCX), producing delayed after depolarizations (DADs). When these DADs reach sufficient amplitude, they may trigger premature action potentials and ventricular ectopic beats, which under catecholaminergic stimulation can degenerate into ventricular tachycardia and fibrillation[44]. Several mechanistic explanations have been proposed for the spontaneous Ca^{2+} release in CPVT, including direct disruption of the RyR2-stabilising complex, destabilization of RyR2 closed state, and lowering of the threshold for RyR2 opening in response to high levels of luminal free Ca^{2+} (Store-Overload-Induced Ca^{2+} Release, SOICR)[44,45]. Specifically, for CPVT2, impaired Ca^{2+} buffering is widely considered the pathological cause, though the precise mechanisms are expectedly different across mutation types within distinct penetrance.

Current therapeutic strategies for CPVT include beta-adrenergic blockers as first-line therapy, flecainide, left cardiac sympathetic denervation (LCSD) for drug-refractory cases, and implantable cardioverter-defibrillators (ICDs) in high-risk patients[44]. The significant variability in penetrance and clinical severity among CASQ2 mutation carriers, even within the same family, highlights the complexity of CPVT2 pathophysiology and the limitations of current genotype–phenotype models[46,47].

1.5.1 CASQ2 mutations involved in CPVT2

To date, dozens of distinct pathological CASQ2 variants have been associated with CPVT2, encompassing missense mutations, nonsense variants, small insertions/deletions, and splice-site changes[46,48]. Crucially, these mutations are distributed across all three thioredoxin domains of CASQ2 and do not cluster at any single structural locus, a distribution that has historically been difficult to reconcile with interface-disruption models[17]. A new mechanistic framework proposed by our group[22] suggests that the mutations, distributed across CASQ2 surface could alter the polymeric properties without necessarily disrupting any specific binding interface.

For the autosomal recessive form of CPVT2, two principal mechanisms have been evoked. The first involves direct disruption of CASQ2–RyR2 functional coupling, such that mutated CASQ2 fails to appropriately inhibit RyR2 at low luminal Ca^{2+} levels[11,43,45]. A prominent example is the CASQ2-R33Q missense variant, the first CPVT2 mutation identified in humans. Studies in a knock-in mouse model suggest that this mutant protein fails to inhibit RyR2 under low luminal Ca^{2+} conditions[43], and the same model reportedly shows a loss of CASQ2 from the jSR together with an absence of the electron-dense polymer, consistent with impaired polymerization and/or jSR retention[42]. The second mechanism invokes a quantitative reduction of CASQ2-mediated Ca^{2+} buffering capacity, which may result either from a decrease in jSR CASQ2 protein levels or from a functional impairment of buffering despite largely normal protein levels, in both cases increasing the amount of free luminal Ca^{2+}, which triggers spontaneous opening of RyR2 and diastolic Ca^{2+} release[44,45].

The question of how the disease penetrance of CASQ2 mutations is encoded at the molecular level has been addressed by recent investigations. A large international multicentre study by Ng and colleagues[46] confirmed the genetic heterogeneity of CPVT2 and highlighted significant variability in penetrance and clinical severity, including unexpected arrhythmic phenotypes in heterozygous carriers. Wleklinski and colleagues[49] examined the dominant K180R variant in a knock-in mouse model and found that, unlike recessive CASQ2 models, this variant did not reduce jSR CASQ2 content or total SR Ca^{2+}; instead, it appeared to alter the dynamic Ca^{2+}-buffering properties of the SR.

The mechanistic classification proposed by our group[2,22] provides a coherent conceptual basis for these observations (Figure 7). Because CASQ2 appears to dimerize intrinsically at physiological ionic conditions, independently of Ca^{2+}, the dimerization competence of a CASQ2 variant may function as a quality-control checkpoint determining whether it is trafficked to, and/or retained within, the jSR. Given that CASQ ability to multimerize is intimately linked with its trafficking[50], those CASQ2 mutations that destabilize the monomer fold or dimerization interface, would be recognized as defective during jSR targeting, leading to loss of total CASQ2 in the homozygosis context.

Dominant-negative CASQ2 variants, are instead proposed to retain dimerization competence but alter higher-order assembly properties: as they are trafficked to the jSR, they co-polymerize with wild-type CASQ2 to form defective polymers with altered Ca^{2+} buffering dynamics[17]. This model is consistent with published murine data: all published animal models of the recessive form feature a major loss of jSR-localized CASQ2 and reduced SR Ca^{2+} content, whereas the only available dominant-negative model (K180R) features a defect in dynamic jSR Ca^{2+} exchange but no loss of total CASQ2 or Ca^{2+} content[17].

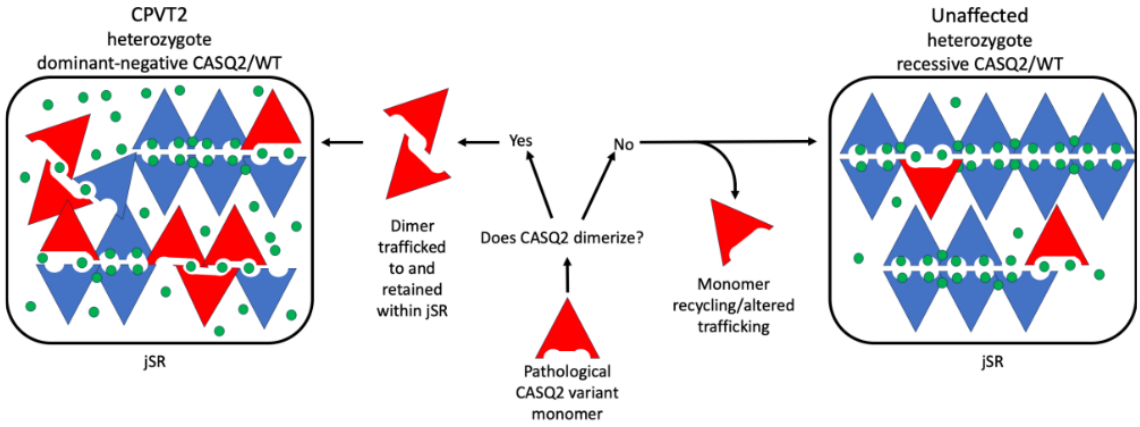

Figure 7. Proposed molecular mechanisms distinguishing recessive and dominant-negative CASQ2 variants. Recessive mutations destabilize the monomer or dimer, preventing jSR trafficking and retention, an effect compensated in heterozygotes by the wild-type allele, whereas dominant-negative variants escape this quality-control checkpoint and incorporate into jSR polymers, sequestering wild-type CASQ2 into dysfunctional hetero-polymers that impair Ca^{2+} buffering, promote aberrant RyR2 opening, and predispose to arrhythmia. Pathological CASQ2 in red, wild type in blue, Ca^{2+} ions in green. (Image taken from Marabelli et al, 2026)[22]

1.6 Molecular dynamics simulation as a tool to study the CASQ2 C-terminus tail

1.6.1 Principles of molecular dynamics simulation

The structural and dynamic properties of biological macromolecules are ultimately governed by the physical interactions between their constituent atoms and the surrounding solvent. Molecular Dynamics (MD) simulation is a computational method that models these interactions over time by numerically integrating Newton's classical equations of motion for each atom in a pre-defined system. Its fundamental premise is that, given the positions and velocities of all atoms at an initial time and an adequate description of the forces acting between them, the subsequent evolution of the system can be calculated step by step[51]. The result is a trajectory, a time-series of atomic coordinates, from which structural, dynamic, and thermodynamic properties of the molecule of interest can be extracted.

The forces acting between atoms in an MD simulation are described by a "force field": a mathematical model that approximates the potential energy of the system as a function of atomic positions. A force field typically decomposes the total potential energy into bonded terms (describing bond stretching, angle bending, and torsional rotation about dihedral angles) and non-bonded terms (describing long-range electrostatic interactions, modelled via Coulomb's law, and short-range van der Waals interactions, modelled via Lennard-Jones potentials). The parameters for these terms are derived from a combination of quantum mechanical calculations and experimental data, and have been refined over decades for the major classes of biological molecules including proteins, nucleic acids, lipids, and small molecules[51]. Widely used biomolecular force fields include CHARMM, AMBER, GROMOS, and OPLS, each with its own parameterization strategy and strengths.

In practice, the system to be simulated (typically a protein surrounded by explicit water molecules and ions) is placed in a simulation box to which periodic boundary conditions (PBC) are applied. PBC means that each face of the simulation box is mathematically connected to the opposite face, effectively creating an infinite periodic system that eliminates artificial surface effects while keeping the computational cost manageable[51]. Before production dynamics, the system is energy-minimized to remove steric clashes, then gradually heated and equilibrated under controlled temperature and pressure conditions. Production simulations are then run in statistical mechanical ensembles, most commonly the NPT ensemble (constant number of particles N, pressure P, and temperature T), which mimics the experimental conditions of a protein in aqueous solution[51] (Figure 8). The timestep used to integrate the equations of motion is typically 2-4 femtoseconds (fs), dictated by the fastest atomic motions in the system (bond vibrations).

The principal strength of MD simulation as a structural biology tool lies in its ability to provide atomically detailed information about protein dynamics, conformational flexibility, and molecular interactions: those pieces of information that, sometimes, are inaccessible to experimental structural methods such as X-ray crystallography, which provides a single structural conformation at an energetic minimum, or NMR spectroscopy, which is strongly limited by the protein's molecular size and other biochemical features[51]. MD simulations are thus a powerful complement to experimental approaches and are increasingly used to interpret experimental data in mechanistic terms. They can reveal how a protein samples its conformational space over time, how binding events occur and what residues are involved, and how mutations or post-translational modifications alter protein dynamics.

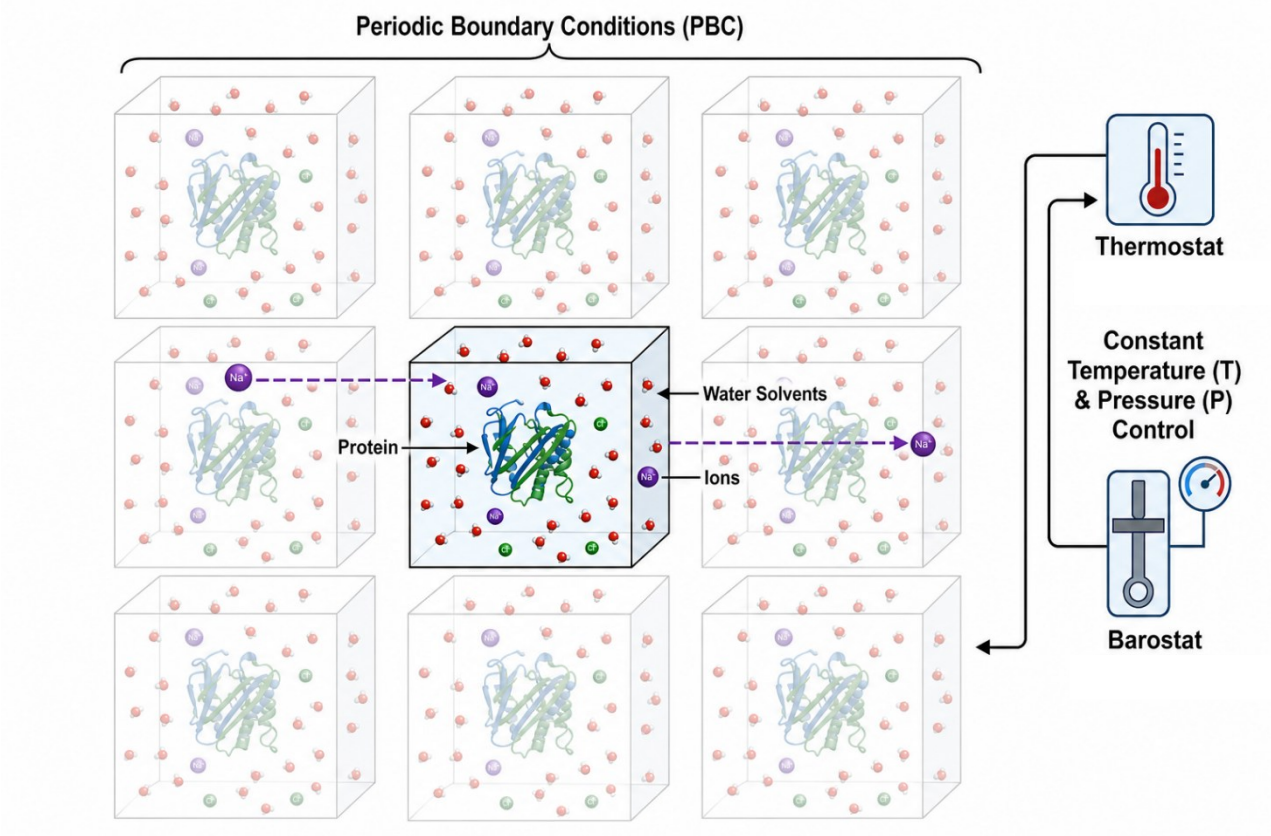

Figure 8. Schematic representation of a typical MD simulation setup. A protein of interest is placed in an explicit solvent box containing water molecules and ions, to which Periodic Boundary Conditions (PBC) are applied: each face of the simulation box is connected to its opposing face, creating an effectively infinite periodic system that eliminates artificial surface effects. Temperature and pressure are maintained constant throughout the simulation by coupling to a thermostat and a barostat respectively, corresponding to the NPT ensemble. The dashed arrows illustrate how an ion exiting one face of the central box re-enters from the opposite face of an adjacent periodic image. (Figure created using Google Gemini 2.5 Flash Image (Nano Banana))

1.6.2 Challenges and opportunities for MD simulation of IDRs: application to the CASQ2 C-terminus

While MD simulation has been successfully applied to folded proteins for decades, its application to intrinsically disordered regions presents unique technical challenges. The fundamental difficulty is that IDRs do not occupy a single energy minimum but instead sample a broad, relatively flat conformational energy landscape[30,52]. Adequate characterization of this conformational ensemble requires that the simulation samples a sufficient number of distinct conformational states, a requirement that can be difficult to satisfy because the timescales for interconversion between distant conformations in the ensemble may require a computational power that is not achievable.

A second major challenge is the accuracy of the force field and water model. It has been extensively documented that conventional MD force fields, developed primarily for folded proteins, tend to over-compact disordered proteins, generating simulated ensembles that are more collapsed than experimentally observed[52,53]. This bias arises at least in part from inadequate modelling of water–

protein dispersion interactions: Piana and colleagues[53] showed that conventional water models underestimate London dispersion interactions, the weak but ubiquitous attractive forces arising from transient fluctuations in electron density that govern the solvation of solute molecules, including unfolded and disordered protein chains, causing artificial compaction of disordered states. The development of the TIP4P-D water model, which approximately corrects for these dispersion deficiencies, was shown to substantially improve the agreement between simulated and experimental properties of disordered proteins[53]. Similarly, the CHARMM36m force field was developed specifically to better reproduce both folded and disordered protein states[54] and has become widely adopted for intrinsically disordered proteins (IDPs) simulations.

For highly charged IDRs such as the CASQ2 DEX^{n}-motif, an additional layer of complexity is introduced by the need to accurately model ion–protein electrostatic interactions. As discussed throughout this introduction, the conformational behaviours of the CASQ2 C-terminus is expected to be strongly sensitive to the concentrations of Ca^{2+}, Mg^{2+}, and K^{+} in the simulation environment, reflecting the polyelectrolyte-like character of this region[2,19,22]. The parameterization of divalent cations such as Ca^{2+} and Mg^{2+} in biomolecular force fields is a known source of inaccuracy: standard parameters may not correctly reproduce both the hydration free energy and the binding preferences of divalent cations with carboxylate groups simultaneously[55]. Given that the C-terminal DEX^{n}-motif is proposed to be the primary locus of Ca^{2+}/Mg^{2+} discrimination[19], and that this discrimination is physiologically crucial for the prevention of diastolic Ca^{2+} release, optimized divalent cation parameters developed specifically for use with modern water models represent an important consideration in the design of MD simulations of the CASQ2 C-terminus[55].

Despite these challenges, MD simulation has emerged as an important tool for investigating also IDR structure and dynamics, complementing experimental approaches such as NMR, SAXS, and single-molecule fluorescence[30,56]. Kasahara and colleagues reviewed the use of MD simulations for IDPs and their fuzzy complexes, highlighting the ability of MD to reveal the transient secondary structure elements, preferred conformational states, and interaction surfaces that characterize disordered regions at the atomic level. Henriques and Skepö[52] demonstrated that, with appropriate water model and force field choices, MD can reproduce experimental observables for disordered proteins with reasonable accuracy. For the specific case of the CASQ2 C-terminus, MD simulation offers the unique opportunity to characterize the conformational ensemble of the DEX^{n}-motif in the context of different ionic condition.

Purpose of research

The physio-pathological mechanisms underlying CASQ2 dysfunction and the variable penetrance of CPVT2 remain incompletely understood. A deeper characterization of the biochemical properties of CASQ2, and in particular of how its polymerization behaviour and ionic environment shape its regulatory function within the jSR, is essential to advance our understanding of the molecular basis of CPVT2 and related cardiac Ca^{2+} handling disorders.

A distinctive and largely unexplored structural feature of CASQ2 is its intrinsically disordered C-terminal tail, the DEX^{n}-motif, a 29-residue segment absent from all available crystal structures and enriched in acidic residues. Available evidence suggests that this region contributes to Ca^{2+}-dependent polymerization, to interactions with the Ca^{2+} release unit, and to the discrimination between Ca^{2+} and Mg^{2+} signals at the RyR2 luminal complex. However, the molecular basis of these functions under the multi-ionic conditions of the jSR lumen, which contains not only Ca^{2+} but also physiologically persistent concentrations of Mg^{2+} and K^{+}, had not been directly investigated.

The present thesis addresses this gap through an integrated experimental and computational approach. The specific aims were: (i) to characterize the functional contribution of the CASQ2 C-terminal tail to Ca^{2+} and Mg^{2+} responsiveness using turbidimetric assays on wild-type CASQ2 and two C-terminal truncation mutants (E373X and D383X) designed to dissect the proximal and distal sub-segments of the tail; (ii) to investigate the atomic-resolution conformational and dynamic properties of the tail under K^{+}, Ca^{2+}, and Mg^{2+} conditions through molecular dynamics simulations of both the isolated tail peptide and the full CASQ2 homodimer; and (iii) to validate the computational findings through complementary in vitro biophysical approaches including ζ-potential measurements, intrinsic tryptophan fluorescence thermal stability assays, dynamic light scattering, and cryo-electron microscopy.

Material and methods

3.1 Expression and purification of cardiac calsequestrin and C-terminus deleted mutants

pET28a-based expression constructs were transformed into the BL21 (DE3) *E. coli* strain. Overnight starter cultures were used to inoculate large-scale cultures (750 mL of broth per 2.8 L flask), which were grown at 37 °C to an optical density (OD_{600nm}) of 0.5 before induction with 1 mM IPTG. Following induction, cultures were incubated for an additional 3 hours at 30°C. All cultures were grown in standard LB medium supplemented with 25 µg/mL kanamycin and 50 µg/mL chloramphenicol. Cells were harvested by centrifugation at 3,500 rpm for 20 minutes, and the resulting cell pellets were collected and stored at -80 °C.

Frozen cell pellets were resuspended in resuspension buffer (20 mM KPi, pH 7.4, 500 mM NaCl, 20 mM imidazole, 1 mM β-mercaptoethanol) and lysed mechanically using a Minilys® bead-beater (Bertin Technologies) at maximum speed (5000 rpm) for four cycles of 30 seconds. The lysate was clarified by centrifugation at 8,900 rpm for 1 hour at 4 °C. The supernatant was then filtered through a 0.45 µm membrane, and Calsequestrin-containing fractions were isolated via immobilized metal affinity chromatography (IMAC) using a 5 mL HisTrap FF column on an ÄKTA go FPLC system. The IMAC buffers were as follows: Buffer A (20 mM KPi, pH 7.4, 500 mM NaCl, 20 mM imidazole) and Buffer B (20 mM KPi, pH 7.4, 500 mM NaCl, 300 mM imidazole). Protein was eluted in a three step of Buffer B concentration (2% - 10% - 100%) and subsequently dialyzed overnight at 4 °C in dialysis buffer (20 mM HEPES, pH 7.3, 100 mM NaCl, 5 mM EDTA, 1 mM β-mercaptoethanol).

Anion exchange chromatography was performed using a 5 mL HiTrap Capto Q column with Buffer A (20 mM HEPES, pH 7.3, 100 mM NaCl) and Buffer B (20 mM HEPES, pH 7.3, 1 M NaCl). Protein was eluted using a continuous gradient from 0% to 100% Buffer B , with Calsequestrin consistently eluting at 40–50%. The Calsequestrin-rich fractions were pooled and concentrated using an Amicon® centrifugal filter unit with a 10 kDa molecular weight cut-off until the sample volume was reduced to less than 5 mL.

Size-exclusion chromatography (SEC) was performed by loading the sample into a 10 mL loop using a 5 mL syringe and allowing it to flow through a HiLoad 26/600 Superdex 200 pg column equilibrated with gel filtration (GF) buffer (20 mM HEPES, pH 7.3, 50 mM KCl). Calsequestrin-rich fractions were pooled, concentrated using the previously described filtration method, aliquoted, and stored at -80 °C.

3.2 C terminus tail design with RosettaRemodel

The structural model of the CASQ2 dimer (PDB ID: 6OWW)[17], used as the starting point, spans residues 22–370, leaving the intrinsically disordered C-terminal tail (residues 371–399, 29 amino acids) unresolved in both the chains of the dimer. To model this region, we employed the RosettaRemodel framework[57], which enables de novo loop and tail construction within the context of a fixed protein scaffold.

Modelling was performed sequentially on each chain of dimeric assembly to preserve the biological context of the homodimer throughout the process. The globular core of each chain was held fixed, with the backbone and side-chain conformations of residues 22–370 constrained to their crystallographic coordinates. The C-terminal tail (residues 371–399) was treated as a fully flexible region and sampled de novo using blueprint-guided fragment assembly. Hydrogen atoms were optimized during each run, and enhanced rotamer sampling was applied via expanded $\chi 1$ and $\chi 2$ rotamer libraries.

For each chain, 1,000 independent structural models were generated, each corresponding to one of 10 independent trajectories. The model with the lowest Rosetta total energy score was selected as the representative conformation for that chain. This procedure was first applied to chain A, and the resulting lowest-energy model served as the updated template for the subsequent modelling of the C-terminal tail of chain B, maintaining the integrity of the dimeric interface throughout. Following completion of both modelling rounds, the final dimeric structure, comprising both fully modelled C-terminal tails, was selected based on the overall lowest Rosetta energy score among all generated models.

Despite treating the C-terminal tail as a fully flexible region in the blueprint specification, all 1,000 models, in both the chains, generated by RosettaRemodel converged on α-helical conformations for the tail sequence. This outcome is a known tendency of fragment-based assembly methods, which draw on secondary structure propensities encoded in the fragment library and can impose helical bias on sequences with moderate helix-forming potential even when no explicit secondary structure constraint is specified. Since the DEX^n-motif of CASQ2 is predicted to be intrinsically disordered by multiple algorithms and its helical assignment by RosettaRemodel was therefore considered artefactual, a dedicated structural relaxation step was introduced.

The final lowest-energy dimeric model, with both C-terminal tails in their RosettaRemodel-assigned helical conformations, was subjected to a high-temperature MD simulation designed to relax the tail structures while preserving the crystallographic validated globular core. The simulation was

performed with all backbone heavy atoms of the globular region (residues 22–370) restrained by positional harmonic constraints, preventing any reorganization of the structured core while allowing the C-terminal tails to explore their conformational space freely. The system was neutralized with counterions, but no additional salt was added, to avoid ionic effects on the relaxation trajectory. The simulation temperature was set to 380 K to provide sufficient thermal energy to overcome the helical energy barriers imposed by the Rosetta fragment assembly and accelerate the relaxation of the tail toward a disordered ensemble on a computationally tractable timescale.

The resulting high-temperature trajectory was monitored for the loss of α-helical content in the tail region and for the stabilization of a disordered conformational ensemble. Representative structures extracted from the converged portion of this trajectory, in which the tails had fully lost their initial helical geometry and were sampling extended and collapsed coil conformations, were used as the starting structures for all subsequent simulations: both the isolated C-terminal tail peptide simulations and the full dimeric CASQ2 simulations.

3.3 Molecular dynamics simulations

All molecular dynamics simulations were performed using NAMD 3.0[58] with the CHARMM36m[54] force field for proteins and ions. Two distinct simulation systems were constructed: one consisting of the isolated CASQ2 C-terminal tail peptide (residues 371–399) and one consisting of the complete CASQ2 homodimer including the modelled C-terminal tails. The two systems differed in size, ionic composition, simulation duration, and starting structure selection strategy, and are described separately below.

3.3.1 System preparation

All systems were solvated in an explicit water box using the TIP3P[59] water model. All residues were kept in their default protonation states as defined by the CHARMM36m topology, and histidine residues were modelled in their neutral tautomeric form. System preparation was performed using VMD[60]. Hydrogen mass repartitioning (HMR) was applied to enable a 4 fs integration timestep, and all bonds involving hydrogen atoms were constrained using the SHAKE algorithm[61]. Each system was energy-minimized and subsequently equilibrated for 1 ns under harmonic position restraints of 1 kcal/(mol·Å²) applied to protein backbone atoms. Production simulations were carried out in the NPT ensemble at 310 K and 1 atm using periodic boundary conditions. Temperature and pressure were controlled using a Langevin thermostat and Langevin barostat respectively.

3.3.2 Isolated C-terminal tail simulations

The C-terminal tail (residues 371–399) was modelled as described in the preceding section, and the high-temperature relaxation structures were used as starting conformations for all production simulations. The CASQ2 DEX^{n} peptide (residues 371–399) solvated in a water box of dimensions 58 × 50 × 53 Å, for a total system size of approximately 14,000 atoms. Four ionic conditions were simulated, each corresponding to a different divalent cation concentration: 0, 50, 100, and 200 mM $CaCl_2$ or $MgCl_2$, all in a background of 100 mM KCl. The background KCl was present in all conditions, and the divalent cation concentration was varied by adjusting the number of Ca^{2+} or Mg^{2+} and the corresponding Cl^- ions added to the system in order to guarantee the neutrality of the system. Each ionic condition was simulated in triplicate, with all three replicates initiated from the same starting conformation of the C-terminal tail peptide extracted from the high-temperature relaxation trajectory described in the preceding section. Each replicate was run for 400 ns.

3.3.3 Full CASQ2 dimer simulations

The dimeric human cardiac CASQ2 structure with the modelled and relaxed C-terminus tail, as described in section 3.2, was used as the initial structural model for the simulation systems. The crystallographic structure experimentally resolved in complex with 15 ytterbium (Yb^{3+}) ions located at the interfacial region between the two monomers. The atomic coordinates of the Yb^{3+} sites were retained as reference positions for the placement of alternative cations (K^+, Ca^{2+} or Mg^{2+}) in the dimer simulations, as described below. The full dimer simulation system was solvated in a water box whose dimensions varied between conditions from 96 × 96 × 112 Å to 114 × 129 × 139 Å, for a total system size ranging from approximately 97,000 to 196,000 atoms depending on C-terminus tails positions.

Three ionic conditions were simulated for the full dimer: KCl only, with $CaCl_2$, and $MgCl_2$. In all conditions, a background ionic strength of 100 mM KCl was maintained. For the divalent cation conditions (Ca^{2+} and Mg^{2+}), a total of 46 molecules of $CaCl_2$ or $MgCl_2$ were added to the system in addition to the background KCl. This number was chosen based on the stoichiometry of the C-terminal tail: the DEX^{n}-motif of each chain contains 23 aspartate and glutamate residues, and since the homodimer contains two C-terminal tails, 46 divalent cation molecules were considered appropriate to provide sufficient ions to fully interact with all tail carboxylate groups simultaneously. Additionally, 15 divalent cation ions were placed at the crystallographic positions of the Yb^{3+} ions at the inter-monomer interface, following the atomic coordinates resolved in the crystallographic structure. For the K^+-only condition, 46 additional KCl molecules were added to maintain equivalent total ion counts relative to the divalent cation conditions, together with the 15 K^+ ions placed at the interfacial Yb^{3+} reference positions.

Each ionic condition was simulated in triplicate, with the three replicates initiated from three distinct starting conformations of the C-terminal tails extracted from the high-temperature relaxation trajectory. The three starting conformations were selected to sample three different ranges of the centre-of-mass (COM) distance between each C-terminal tail and the globular core of the dimer, in order to ensure that the production simulations sampled the conformational space of the tail without bias toward any particular starting geometry. The selected COM distance ranges were: near (36 Å and 45 Å for the two tails respectively), intermediate (56 Å and 59 Å), and far (55 Å and 66 Å). These distances were measured between the COM of the tail (residues 371–399) and the COM of the globular core (residues 22–370) for each chain independently, and the three starting frames were identified from the high-temperature relaxation trajectory as representative structures within each distance range. Each replicate was run for 750 ns.

3.4 Molecular dynamics simulations analysis

Unless otherwise specified, all structural and dynamic analyses of the MD simulation trajectories were performed using standard tools available within the VMD software packages. This includes root mean square fluctuation (RMSF) calculations, centre-of-mass (COM) distance measurements, solvent-accessible surface area (SASA) analysis, secondary structure assignment, and radius of gyration (Rg) calculations. Principal component analysis (PCA) and free energy landscape (FEL) construction, and autocorrelation function (ACF) analysis are described separately in sections 3.4.1 and 3.4.2 respectively. Ion-protein coordination occupancy and net charge of the protein were calculated by measuring the number of ions present within a defined cutoff distance from the carboxylate oxygens of aspartate (OD1, OD2) and glutamate (OE1, OE2) residues throughout the simulation trajectories. The cutoff distances used for each ion were determined from the first coordination shell peak of the radial pair distribution function (g(r)) computed between each ion and the relevant carboxylate oxygen atom types. For the isolated C-terminal tail simulations, cutoff distances of 2.5 Å for Ca^{2+} and 4.0 Å for Mg^{2+} were applied. For the full dimer simulations, cutoff distances of 2.5 Å for Ca^{2+} and 2.1 Å for Mg^{2+} were applied. The net charge of the protein at each simulation frame was calculated as the intrinsic charge of the protein at pH 7.3 minus the number of coordinated ions multiplied by their respective charge, averaged over the production trajectory.

The average number of water molecules in the first coordination shell of Ca^{2+} and Mg^{2+} ions was calculated using a cutoff distance of 2.3 Å between the ion and the oxygen atoms of water molecules (OW). This cutoff was determined from the first minimum of the radial pair distribution function g(r)

between each ion and water oxygen, which defines the boundary of the first hydration shell for both Ca^{2+} and Mg^{2+} under the simulation conditions used. In the full dimer simulation the coordination events were defined as frames in which at least one carboxylate oxygen of an aspartate or glutamate residue was simultaneously within the ion-specific cutoff distance defined above, and the water coordination number was averaged exclusively over such frames to provide a direct comparison of solvation state between free and protein-coordinated ions.

3.4.1 Principal Component Analysis and Free Energy Landscape Construction

Principal component analysis (PCA) of the C-terminal tail conformational dynamics was performed using the cpptraj module of the AmberTools software package[62]. All nine production trajectories, three replicates for each of the three ionic conditions (Ca^{2+}, Mg^{2+}, K^{+}), were loaded simultaneously to construct a pooled covariance matrix capturing the full conformational space sampled across all conditions.

Prior to PCA, each trajectory frame was re-imaged to correct for periodic boundary condition artefacts, and all frames were aligned by root mean square fitting of the backbone atoms (C, Cα, N, O) of the globular core residues of both monomers to remove rigid-body translational and rotational motion of the structured core while preserving the conformational dynamics of the disordered tails. The covariance matrix was computed exclusively over the Cα atoms of the C-terminal tail residues (371-399) of both monomers simultaneously, treating the two tails as statistically equivalent samples of the same conformational ensemble. Mass-weighted covariance was used. The covariance matrix was diagonalized to extract the first 20 eigenvectors, and each ionic condition was then projected independently onto the first two principal components (PC1 and PC2) of this shared eigenvector space. The use of a shared eigenvector space derived from the pooled trajectories of all three conditions ensures that the resulting PC1–PC2 projections are directly comparable across ionic conditions.

Free energy landscapes (FELs) for each ionic condition were constructed from the PC coordinate distributions using a two-dimensional histogram approach. The free energy at each point in PC1–PC2 space was calculated as:

$$F(PC1, PC2) = -k_b N_A T ln P(PC1, PC2)$$

where P(PC1, PC2) is the normalized probability density estimated from the histogram of sampled PC coordinates, k_b is the Boltzmann constant, N_A is the Avogadro number and T is the simulation

temperature (310 K). The three FELs were normalized to a shared global reference defined as the lowest free energy minimum observed across all three conditions, corresponding to the Mg^{2+} simulation (F_min = 0.00 kJ/mol), to enable direct quantitative comparison of the relative stability of the dominant conformational states across ionic conditions. The overlaid contour representation of the three FELs was generated in Python, all three conditions were projected onto the same PC1–PC2 coordinate space to allow direct visual comparison of the conformational regions sampled under each ionic condition.

3.4.2 Autocorrelation Function Analysis

The conformational memory of the CASQ2 C-terminal tail under each ionic condition was quantified through autocorrelation function (ACF) analysis of the center-of-mass (COM) distance between the C-terminal tail (residues 371–399) and the globular core of the dimer (residues 22–370), sampled at 1 ns intervals over the production trajectories. For each replicate and each ionic condition, the two per-chain COM distance traces, one per C-terminal tail of the homodimer, were averaged to produce a single representative trace per condition per replicate. The normalized ACF C(τ) was computed for each averaged trace as:

$$C(\tau) = [\delta x(t) \cdot \delta x(t+\tau)] \,/\, [\delta x(t)^2]$$

where $\delta x(t) = x(t) - \langle x \rangle$ is the mean-subtracted COM distance and τ is the lag time in nanoseconds. The computation was performed using full cross-correlation, extracting the positive-lag half and normalizing to C(0) = 1. The maximum lag analyzed was 300 ns, corresponding to less than half the trajectories length (753/2 ≈ 376 ns), ensuring statistical reliability of the estimates at all reported lags. The integrated autocorrelation time τ_int was computed as:

$$\tau int = \int_0^T C(\tau)\ d\tau$$

where T is the lag time at which C(τ) first crosses zero. This integral represents the total area under the ACF curve and has a direct physical interpretation: it quantifies the total duration of positional memory of the C-terminal tail, independently of the specific functional form of the ACF decay. The integral was evaluated numerically using the trapezoidal rule with a timestep of Δt = 1 ns. τ_int values were computed independently for each of the three replicates and are reported as mean ± SD. Statistical comparison between ionic conditions was performed using a two-tailed t-test. All computations were performed in Python 3 using NumPy.

3.5 Turbidimetric analysis

Turbidimetric assays were performed to monitor Ca^{2+}- and Mg^{2+}-dependent polymerization of wild-type CASQ2 and C-terminal truncation mutants (E373X and D383X) in real time. All measurements were carried out in a 1 mL cuvette using a GENESYS UV-Vis Spectrophotometer (Thermo Fisher Scientific), monitoring absorbance at 350 nm with a time resolution of 6 seconds. Proteins were diluted from concentrated stock solutions to a final concentration of 2.5 µM in assay buffer consisting of 20 mM HEPES pH 7.3 and 50 mM KCl at room temperature (20°C), for a final volume of 1 mL. Immediately after dilution, the sample was gently resuspended by pipetting. The blank was recorded on the protein sample immediately after dilution, prior to any salt addition, and was subtracted from all subsequent absorbance readings. Depending on the specific assay, one of the following protocols was applied:

In the immediate addition assay (0 minutes equilibration), 1 mM $CaCl_2$ or 2 mM $MgCl_2$ was added directly to the cuvette immediately after protein dilution and blank acquisition, and turbidity was monitored continuously from the moment of salt addition.

In the time-dependent equilibration assay, the protein was allowed to equilibrate in buffer for 10 or 40 minutes at room temperature before salt addition. Turbidity was recorded continuously throughout the equilibration period and following subsequent addition of 1 mM $CaCl_2$ or 2 mM $MgCl_2$.

In the Mg^{2+} preincubation assay, 2 mM $MgCl_2$ was added immediately after protein dilution and the sample was incubated for 45 minutes, after which 1 mM $CaCl_2$ was added and turbidity recording continued. A parallel condition in which Mg^{2+} was added after 45 minutes of buffer-only equilibration was also tested to assess the directionality of the Mg^{2+} priming effect.

In the cold temperature equilibration assay, the assay buffer was pre-cooled to 4°C prior to protein dilution. The protein was diluted into the cold buffer and incubated at 4°C for 45 minutes, after which 1 mM $CaCl_2$ was added and turbidity was monitored at room temperature.

In all conditions, each salt addition was followed by gentle resuspension by pipetting before resuming data acquisition. All assays were performed at room temperature (20°C) in triplicate using independently prepared protein samples, results are presented as the mean of three independent experiments.

3.6 Thermal stability assay

Thermal stability assays based on intrinsic tryptophan fluorescence were performed using a Tycho NT.6 instrument (NanoTemper Technologies), which monitors the fluorescence emission ratio at 350/330 nm as a function of temperature during a thermal ramp from 35°C to 95°C at a rate of 30°C per minute. This ratio provides a sensitive reporter of the tryptophan microenvironment: a higher ratio indicates greater solvent exposure of tryptophan residues, while a lower ratio reflects a more buried, hydrophobic environment. To characterize the effect of increasing Ca^{2+} or Mg^{2+} concentrations on the tryptophan environment of wild-type CASQ2 and CASQ2-E373X, proteins were diluted to a final concentration of 30 µM in assay buffer containing 20 mM HEPES pH 7.3 and 150 mM KCl. $CaCl_2$ or $MgCl_2$ was then added to the desired final concentration, ranging from 0 to 20 mM. Following ion addition, samples were incubated on ice for 40 minutes in ice to allow equilibration. Immediately before measurement, each sample was gently resuspended by pipetting, loaded into standard Tycho capillaries, and analysed.

To assess whether distinct ionic history conditions produce equivalent or distinct assembled protein states as detected by thermal stability, the same sample preparation protocol described for the turbidimetric assays was applied. Briefly, wild-type CASQ2 was diluted to 2.5 µM in 20 mM HEPES pH 7.3 and 50 mM KCl to match the ionic conditions of the turbidimetric experiments, and subjected to the same equilibration conditions, immediate 1mM $CaCl_2$ addition (0 minutes equilibration), 40-minute buffer equilibration at 20°C followed by 1mM $CaCl_2$, 2mM $MgCl_2$ preincubation for 40 minutes followed by 1mM $CaCl_2$, and 40-minute equilibration at 4°C followed by 1mM $CaCl_2$, as described in section 3.5. Following the respective treatment, samples were loaded into Tycho capillaries and measured. The lower protein concentration used in this assay (2.5 µM versus 30 µM) was chosen to maintain direct comparability with the turbidimetric experiments rather than to optimize signal intensity. All measurements were performed in triplicate using independently prepared samples.

3.7 Dynamic light scattering (DLS) analysis

Dynamic light scattering (DLS) measurements were performed using a Nanotrac Flex instrument (Microtrac) to monitor the oligomeric size distribution of wild-type CASQ2, CASQ2-E373X, and CASQ2-D383X over a 40-minute equilibration period at room temperature.

Proteins were diluted to a final concentration of 2.5 µM in assay buffer containing 20 mM HEPES pH 7.3 and 50 mM KCl at 20°C, for a total sample volume of 1 mL, matching the protein concentration, buffer composition, and temperature used in the turbidimetric assays to allow direct comparison between the two datasets. Immediately after dilution, the sample was gently resuspended by pipetting. A 20 µL aliquot was withdrawn immediately after dilution (0 minutes) and subsequently at 10, 20, 30, and 40 minutes of equilibration at room temperature, with the remaining sample maintained at 20°C throughout the experiment. Each aliquot was measured independently to obtain particle size distribution at the corresponding timepoint. All measurements were performed in triplicate using independently prepared protein samples, and results are presented as mean ± SD of three independent experiments.

3.8 Z-potential measurements

ζ-potential measurements were performed to characterize the surface charge of wild-type CASQ2, CASQ2-E373X, and CASQ2-D383X as a function of divalent cation concentration. Measurements were carried out using a Stabino Zeta instrument (Microtrac) equipped with a 0.2 µm cutoff piston. Proteins were diluted to a final concentration of 2.5 µM in assay buffer containing 20 mM HEPES pH 7.3 and 50 mM KCl at room temperature (20°C), for a total sample volume of 10 mL. Following dilution, the protein was allowed to equilibrate in buffer for 10 minutes before the start of the measurement. ζ-potential was then recorded as a function of increasing $CaCl_2$ or $MgCl_2$ concentration, titrated from 0 to 100 mM. At each concentration point, the ζ-potential was recorded continuously for 40 seconds and the reported value represents the average over this acquisition window. All measurements were performed in triplicate using independently prepared protein samples, and results are presented as mean ± SD of three independent experiments.

3.9 Cryo-EM images

Sample grids were prepared by applying 3.5 µL of purified CASQ2, CASQ2-E373X, and CASQ2-D383X protein at a concentration of 2 mg/mL to glow-discharged QuantiFoil r1.2/1.3 Cu grids. Prior to grid preparation, a concentrated CASQ2 sample was incubated for 40 minutes in buffer [20 mM HEPES pH 7.3, 50 mM KCl and 2 mM $MgCl_2$] before final dilution into the same buffer with the addition of 1 mM $CaCl_2$ final concentration. The grids were blotted for 5 or 30 seconds using a Vitrobot Mark IV (Thermo Fisher Scientific) and subsequently plunge-frozen in liquid ethane cooled by liquid nitrogen. Frozen grids were stored in liquid nitrogen until imaging. Cryo-electron microscopy (cryo-EM) data were acquired on a Talos Arctica operating at 198 kV, equipped with a Falcon 3 camera (Thermo Fisher Scientific)

Results and discussion

4.1 Turbidimetric analysis highlights the C-terminal IDR role in Ca^{2+} and Mg^{2+} responsiveness

To investigate the functional role of the intrinsically disordered C-terminal tail of CASQ2 in Ca^{2+}-dependent polymerization, turbidimetric assays were performed on wild-type CASQ2 and two C-terminal truncation mutants, CASQ2-E373X, which lacks the entire DEX^n tail, and CASQ2-D383X, which retains only the proximal ten residues of the tail (residues 373–382) while lacking the distal segment. All experiments were performed at 2.5 μM protein concentration in 50 mM KCl buffer, with Ca^{2+} or Mg^{2+} additions as indicated.

4.1.1 A Ca^{2+} and Mg^{2+} time-dependent response is lost in the CASQ2ΔCter mutants

A first important observation concerns the time-dependence of the Ca^{2+} response of wild-type CASQ2 following dilution from a concentrated stock. When Ca^{2+} (1 mM $CaCl_2$) was added immediately after dilution to 2.5 μM, wild-type CASQ2 produced a rapid and high-amplitude turbidity increase. In contrast, when the protein was allowed to equilibrate in buffer at room temperature (rt), for 10 or 40 minutes before Ca^{2+} addition, the subsequent Ca^{2+} response was progressively attenuated, both in initial rate and in the final turbidity plateau reached, following the rank order 0’ > 10’ > 40’ (Figure 9A). This time-dependent loss of Ca^{2+} responsiveness indicates that freshly diluted CASQ2 exists in a conformational state that is primed for Ca^{2+}-driven polymerization, and that this state relaxes gradually toward a less responsive one over tens of minutes at rt.

The two truncation mutants dissect the tail’s contribution to this behaviour in a spatially resolved manner. CASQ2-E373X (Figure 9B), which lacks the tail entirely, shows a markedly reduced Ca^{2+}-dependent turbidity response compared to wild-type under all three-time conditions. Crucially, in E373X the time-dependence of the Ca^{2+} response is abolished, the responses at 0’, 10’, and 40’ are nearly superimposable, indicating that conformational relaxation over time is a property specific to the C-terminal tail and does not occur for the globular core alone. This result demonstrates that the tail is not merely a passive structural element but is the locus of the time-dependent priming state that governs the amplitude and kinetics of the subsequent Ca^{2+} response. CASQ2-D383X (Figure 9C), retaining the proximal ten residues (373–382), displays an intermediate behaviour: it recovers a fast Ca^{2+} response at 0’, but the kinetics of polymerization is not significantly affected by the duration of

incubation, with 40’ incubation causing a modest reduction in the magnitude of polymerization. This suggests that the proximal sub-segment contributes specifically to the priming function, whereas the distal portion leads the time-dependent lowering of CASQ2 responsiveness. Taken together, these data suggest that the full-length C-terminal tail encodes a metastable state that is kinetically accessible immediately after dilution from high concentration but becomes thermodynamically unfavourable under prolonged exposure to lower than physiological ionic-strength conditions.

Turbidity experiments performed with Mg^{2+} as the sole divalent cation (i.e. used as polymerization trigger instead than Ca^{2+}) also show a time-dependent response analogous to that observed for Ca^{2+}: wild-type (Figure 9D) and D383X (Figure 9F) CASQ2 shows a slower and smaller turbidity increase following the same rank order of 0’ > 10’ > 40’. While the polymerization response to either Ca^{2+} or Mg^{2+} features distinctive properties (where the Mg^{2+}-dependent polymerization of the D383X protein is causes a larger turbidity increase than the wild-type), the time-dependent conformational relaxation globally reduces the protein’s responsiveness to both divalent cations. CASQ2 E373X (Figure 9E) differs, as it is completely insensible to the presence of Mg^{2+} at each equilibration time condition. Overall, these data indicate that the distal portion of the C-terminus tail inhibits the strong Mg^{2+}-dependent polymerization effect, which is exclusively mediated by the proximal portion of the tail, but not of the globular core.

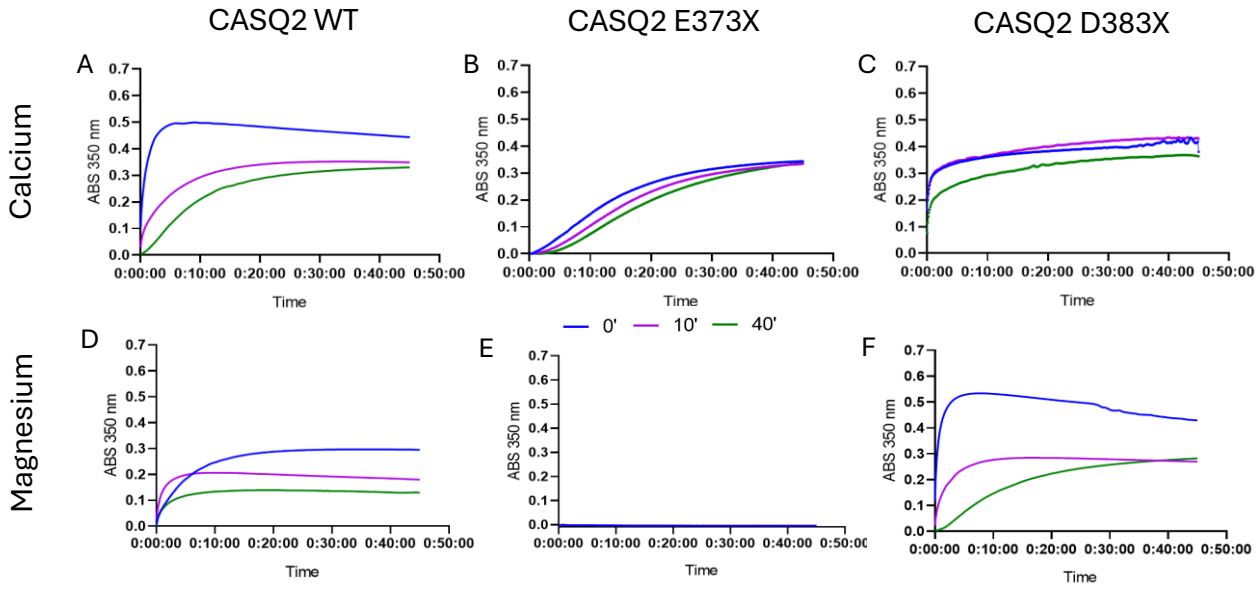

Figure 9. Time-dependent attenuation of Ca^{2+} and Mg^{2+} responsiveness in CASQ2 WT and C-terminal truncation mutants. Turbidimetric assays (absorbance at 350 nm) of wild-type CASQ2 (A, D), CASQ2-E373X (B, E), and CASQ2-D383X (C, F) at 2.5 µM in 50 mM KCl. Proteins were equilibrated at 20°C for 0 (blue), 10 (magenta), or 40 (green) minutes prior to addition of 1 mM $CaCl_2$ (A–C) or 2 mM $MgCl_2$ (D–F). Data are mean of three independent experiments. Wild-type CASQ2 shows progressive attenuation of both Ca^{2+} (A) and Mg^{2+} (D) responsiveness with equilibration time (rank order 0' > 10' > 40'), indicating time-dependent relaxation from a primed conformational state. This time-dependence is abolished in E373X for Ca^{2+} (B) and entirely absent for Mg^{2+} (E), demonstrating that both properties depend on the C-terminal IDR. D383X shows intermediate behaviour for both ions (C, F), partially recovering the time-dependent response through its proximal tail sub-segment (residues 373–382).

An important alternative interpretation of the time-dependent attenuation of Ca^{2+} and Mg^{2+} responsiveness must be considered before attributing this phenomenon exclusively to conformational changes within the C-terminal tail. This is the possibility that the 40-minute equilibration period may produce a progressive redistribution of the native oligomeric population of CASQ2 toward less polymerization-competent species, independently of any tail-specific conformational change. To exclude this alternative, particle size distribution measurements were performed by dynamic light scattering (DLS) on wild-type CASQ2, E373X, and D383X at 2.5 µM in 50 mM KCl, the same protein concentrations and buffer conditions used in the turbidimetric assays, with particle size measured at 0, 10, 20, 30, and 40 minutes of equilibration (Figure 10).

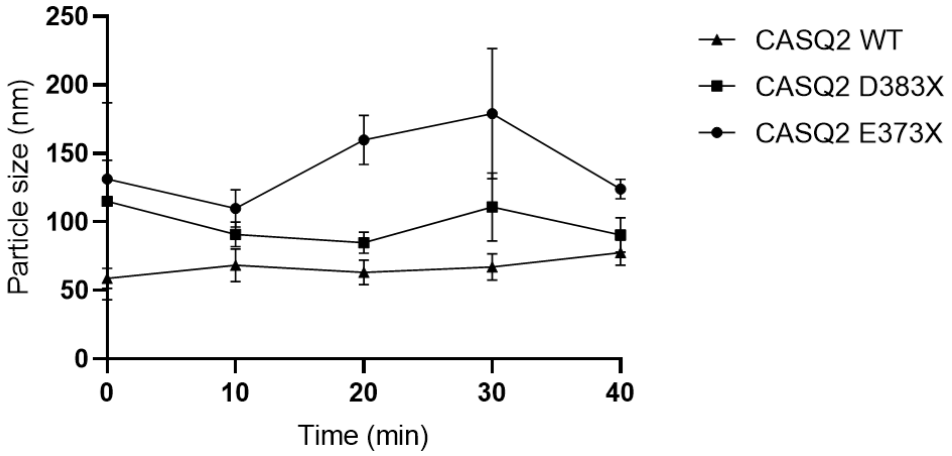

Figure 10. Oligomeric size distribution of CASQ2 WT and C-terminal truncation mutants remains stable during equilibration. Dynamic light scattering measurements of particle size for wild-type CASQ2 (triangles), CASQ2-D383X (squares), and CASQ2-E373X (circles) at 2.5 µM in 50 mM KCl, measured at 0, 10, 20, 30, and 40 minutes of equilibration at 20°C without a constant mixing of the sample during the measurement. Data means ± SD of three independent experiments. None of the three proteins shows a systematic change in average particle diameter over the 40-minute observation window. The three proteins differ in their resting particle size, wild-type ~55–75 nm, D383X ~85–115 nm, E373X ~110–180 nm consistent with the progressive increase in globular surface exposure and decrease of negative charges.

The DLS data show that the particle size distributions of all three proteins remain stable throughout the entire 40-minute observation window, with no systematic directional change in the average particle diameter for any of the three constructs. Wild-type CASQ2 maintains particles in the 55–75 nm range, D383X in the 85–115 nm range, and E373X shows slightly larger particles around 110–180 nm, differences that likely reflect the altered electrostatic surface properties of the truncated proteins relative to wild-type. Crucially, none of the three proteins shows a progressive shift in particle size over the 40-minute window that could account for the time-dependent attenuation of Ca^{2+} or Mg^{2+} responsiveness. The oligomeric composition of the sample is therefore stable on the timescale of the turbidimetric relaxation experiments, and the progressive loss of Ca^{2+} and Mg^{2+} responsiveness

observed in Figure 9 cannot be attributed to a redistribution between oligomeric states. Instead, these data are consistent with the interpretation that the time-dependent relaxation reflects a change occurring within a stable oligomeric ensemble, hence most likely within the C-terminal tail, rather than a change in the stoichiometry of higher-order assemblies.

4.1.2 The CASQ2 C-terminal tail feels different ionic environments

The Mg^{2+} effect on the CASQ2 polymerization in response to Ca^{2+} was already analysed by other groups and it is discussed in the section 1.3.1, here we analyse specifically if the C-terminal tail IDR is involved in this phenomenon.

To address the question, Ca^{2+} responses were compared between wild-type CASQ2 and the two truncation mutants following either buffer-only preincubation or Mg^{2+} preincubation (2 mM $MgCl_2$, 45 minutes), in each case followed by addition of 1 mM $CaCl_2$ (Figure 10A). When Mg^{2+} is present from the moment of dilution, wild-type CASQ2 maintains its fast-responsive state throughout the entire preincubation period, and the subsequent Ca^{2+} response is dramatically amplified relative to the buffer-only equilibrated condition. This observation extends unpublished data from our lab demonstrating that Mg^{2+} stabilizes a distinct CASQ2 dimeric conformation that serves as a productive nucleation platform for Ca^{2+}-driven polymerization. More specifically, the present data add an important mechanistic dimension: in stabilizing a specific state more competent for Ca^{2+}-driven assembly, Mg^{2+} prevents the time-dependent conformational relaxation towards a lower Ca^{2+}-polymerization competent state.

The contribution of specific segments of the C-terminal tail to Mg^{2+} sensing and ion discrimination is revealed by the behaviour of the two truncation mutants in the same experiment. CASQ2-E373X, which lacks the entire DEX^n tail, shows no detectable turbidity response to Mg^{2+} during preincubation and no amplification of the subsequent Ca^{2+} response the Mg^{2+}-preincubated and buffer-only curves are virtually superimposable. In the complete absence of the tail, preincubation with Mg^{2+} is entirely invisible to the protein and only the intrinsic Ca^{2+} sensitivity of the globular core is maintained in CASQ2-E373X. This prove that Mg^{2+} responsiveness is not a property of the CASQ2 globular core but depends on the essential presence of the C-terminal IDR.

CASQ2-D383X, retaining only the proximal ten-residue segment of the tail (residues 373–382), occupies a functionally intermediate position. During Mg^{2+} preincubation, CASQ2-D383X reaches substantially higher turbidity than wild-type, demonstrating that the proximal segment alone is sufficient to restore Mg^{2+} sensitivity, but does so in an exaggerated and presumably unregulated manner in the absence of the distal segment. Following Ca^{2+} addition, CASQ2-D383X shows a fast

turbidity increase under Mg^{2+} preincubation conditions that is clearly larger than the buffer-only response, confirming that the proximal segment also restores the capacity to accommodate the Mg^{2+} preincubation effect, and thus distinguish between different ionic histories. However, the magnitude of Ca^{2+}-specific amplification is substantially smaller than in wild-type, also because polymerization is largely sustained already during Mg^{2+}-preincubation. Together, these observations define a two-component functional architecture within the C-terminal tail: the proximal segment (residues 373–382) is necessary and sufficient for Mg^{2+} sensitivity, functioning as the primary Mg^{2+} sensor of the protein; the distal segment (residues 383–399) provides directional regulatory control, suppressing unproductive Mg^{2+}-driven preincubation assembly and channelling the Mg^{2+} priming signal into supporting a maximal Ca^{2+}-amplifying competent state. The distal segment therefore acts not as a redundant extension of the proximal sensor but as a regulatory governor that converts a raw sensitivity to divalent cations such as Mg^{2+}, into a precisely directed priming output.

A deeper implication of mutant data emerges when the sequential ionic response experiments are considered alongside. In wild-type CASQ2, Mg^{2+} alone and Ca^{2+} alone produce comparable turbidity levels, appearing superficially equivalent as polymerization stimuli. Yet these two conditions generate fundamentally different downstream states: a protein preincubated with Mg^{2+} responds to subsequent Ca^{2+} addition with a large, fast amplification that a Ca^{2+}-preincubated protein cannot reproduce (Figure 11B, blue dashed line). The ionic history is therefore encoded in the protein in a form that is invisible in turbidity, but that determines the quantitative outcome of subsequent Ca^{2+} stimulation. CASQ2-E373X collapses this distinction entirely: without the C-terminal tail, the protein cannot register Mg^{2+} exposure, and Ca^{2+}-dependent polymerization kinetics become indistinguishable, regardless of prior ionic history. The C-terminal tail is therefore the structural element through which CASQ2 acquires the capacity to distinguish between presumably electrostatically equivalent ionic conditions that diverge fundamentally in their consequences for subsequent Ca^{2+}-driven assembly.

The directionality and irreversibility of the Mg^{2+} priming effect are directly tested in Figure 10B. To determine whether Mg^{2+} can restore the fast-responsive state once it has been lost rather than merely preserve it, two conditions were compared that deliver identical total Mg^{2+} exposure and identical total incubation time but differ only in whether Mg^{2+} was present during or after the conformational relaxation window. When Mg^{2+} was added after 45 minutes of buffer equilibration, after the protein had already completed its conformational relaxation, it failed entirely to rescue the fast Ca^{2+} response. Despite a further 45-minute incubation in the presence of Mg^{2+}, the subsequent Ca^{2+} response remained small and slow, closely resembling the buffer-only equilibrated condition rather than the Mg^{2+}-primed one. This asymmetry evidence that the two conformational states accessible to wild-

type CASQ2 are not freely interconvertible by Mg^{2+}. The conformational transition driven by buffer equilibration produces a state that is kinetically trapped and refractory to Mg^{2+} rescue on the timescales tested, implying that the two states are separated by an energy barrier that Mg^{2+} coordination alone is insufficient to overcome once the relaxed conformation has been demostarted. This conformational memory encoded in the C-terminal tail therefore has a defined temporal window during which Mg^{2+} can exert its priming function.

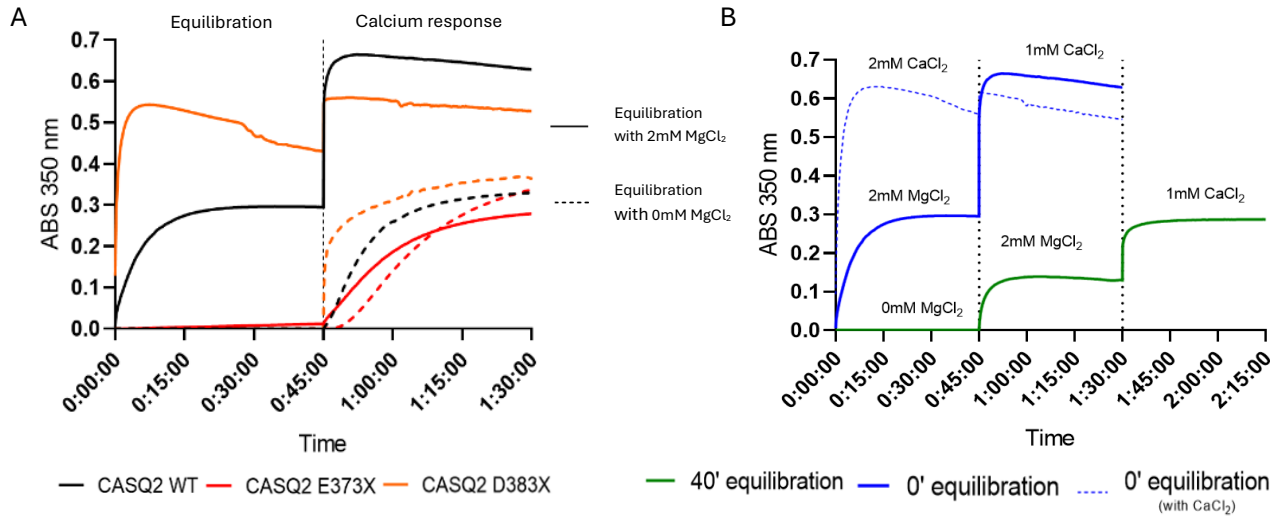

Figure 11. Mg^{2+} priming of Ca^{2+} responsiveness requires the C-terminal tail and is directionally irreversible. (A) Turbidimetric assays (absorbance at 350 nm) of wild-type CASQ2 (WT, black), CASQ2-E373X (red), and CASQ2-D383X (orange) at 2.5 µM in 50 mM KCl. Proteins were preincubated for 45 minutes in the presence (solid lines) or absence (dashed lines) of 2 mM $MgCl_2$, followed by addition of 1 mM $CaCl_2$ (the timepoint in which Calcium was added is highlighted by the dotted vertical line). Wild-type CASQ2 shows dramatically enhanced Ca^{2+} responsiveness following Mg^{2+} preincubation relative to the same protein incubated in buffer only, confirming that Mg^{2+} preserves the fast-responsive primed state. E373X shows no amplification of the Ca^{2+} response regardless of Mg^{2+} preincubation, demonstrating that Mg^{2+} responsiveness depends absolutely on the C-terminal IDR. D383X shows an exaggerated Mg^{2+}-driven turbidity during preincubation and a partial but unregulated Ca^{2+} amplification, consistent with the proximal tail segment (373–382) conferring Mg^{2+} sensitivity and uncontrolled Mg^{2+}-dependent polymerization in the absence of the distal regulatory governor (383–399). Data are mean of three independent experiments. (B) Directionality and irreversibility of Mg^{2+} priming in wild-type CASQ2. The protein was equilibrated for 45 minutes either in the absence of Mg^{2+} (0 mM, green) or in the presence of 2 mM $MgCl_2$ (blue), followed by addition of 1 mM $CaCl_2$ (first dotted vertical line), for the $MgCl_2$ pre-incubated condition, or a 2mM of $MgCl_2$ for the $MgCl_2$-free equilibration condition, followed by an addition of 1mM $CaCl_2$ to both samples (second dotted line). Mg^{2+} added after 45 minutes of buffer equilibration fails to rescue the fast Ca^{2+} response, while Mg^{2+} present since the moment of protein dilution in the experimental buffer fully preserves it. This demonstrates that Mg^{2+} can preserve but not restore the primed, concentration-dependent conformational state of CASQ2 once lost through thermal relaxation. The incubation of fresh diluted CASQ2 with 2mM $CaCl_2$ with subsequent addition of 1mM $CaCl_2$ doesn't reproduce the same effect of magnesium, the fast increase in turbidity is achieved only in the pre-incubation phase but is lost in a subsequent addition of $CaCl_2$. Data are mean of three independent experiments.

Taken together, the turbidimetric data validate that the intrinsically disordered C-terminal tail of CASQ2 is not a passive polyanionic scaffold but the molecular substrate of ionic memory. It endows the protein with three distinct and hierarchically organized properties. First, time-dependent conformational relaxation encodes the protein's recent ionic history within the tail's dynamical ensemble, generating a primed state that is progressively lost upon dilution over tens of minutes in the absence of stabilizing Mg^{2+} ions. Second, a two-component ion-sensing architecture within the

tail, the proximal segment is sufficient for Mg^{2+} sensing whereas the distal regulatory segment confers a directional priming signal to an otherwise Mg^{2+}-blind globular core. Third, the capacity to generate qualitatively distinct Ca^{2+}-responsive states from two ionic conditions (without and with Mg^{2+}), that diverge fundamentally in downstream polymerization competence. The C-terminal tail is therefore the structural element through which CASQ2 encodes not merely which ion is present, but which ion was bound first, translating ionic sequence rather than a simple ratio between distinct ion abundancies into polymerization-competent conformational states.

4.2 The C-terminal tail encodes information via electrostatic self-organization rather than stable secondary structure

To characterize the conformational response of the isolated CASQ2 C-terminal tail to divalent cations at the atomistic level, molecular dynamics simulations were performed on a peptide corresponding to residues 371–399, the full DEX^n-motif, across a titration range of 50 to 200 mM $CaCl_2$ or $MgCl_2$, all in a background of 100 mM KCl. The first and important question was whether the C-terminal tail acquires any stable secondary structure upon ion binding, as it has been proposed on the basis of circular dichroism studies on isolated CASQ C-terminal peptides. Secondary structure analysis of the simulation trajectories across the full concentration range tested did not reveal the formation of stable α-helical elements under either Ca^{2+} or Mg^{2+} conditions at any concentration tested.

To capture the underlying conformational preferences, we quantified the fraction of residues whose backbone dihedral angles (φ, ψ) fall within the right-handed α-helical region (φ between −100° and −30°, ψ between −67° and −7°) of the Ramachandran map (Figure 12A). This metric reports the transient tendency of the backbone to sample helical geometry, regardless of whether a cooperative hydrogen-bonded helix is formed. In the divalent-free reference (0 mM divalent, 100 mM K^+) only ~11% of residues occupy the α-helical region at any instant. Upon addition of divalent cations this occupancy increases in every condition examined, reaching pooled averages of ~20% with Ca^{2+} and ~16% with Mg^{2+}. This enhancement should nonetheless be interpreted with caution: the replica-to-replica variability is large, no monotonic concentration dependence is resolved within the explored range, and the propensity is broadly distributed along the sequence rather than confined to a discrete helical segment. The data therefore indicate a modest but reproducible increase in transient helical sampling in the presence of divalent ions, while providing no evidence for the nucleation of a stable secondary structure. The C-terminal tail remains structurally disordered throughout the simulation, populating a dynamic ensemble of coil and extended conformations without converging on a defined folded state.

Despite the absence of an ordered secondary structure, increasing the divalent ion concentration produced a clear and progressive reduction in the overall dimensions of the tail, consistent with a coil-to-globule compaction transition. The radius of gyration (Rg) of the tail decreases monotonically with increasing ion concentration for both Ca^{2+} and Mg^{2+}, but the magnitude of compaction differs markedly between the two ions: Ca^{2+} produces a substantially larger reduction in Rg than Mg^{2+} at any equivalent concentration tested, and this divergence becomes increasingly pronounced at higher concentrations. At 200 mM $CaCl_2$ the tail reaches a highly compact state, whereas at 200 mM $MgCl_2$ compaction is more limited, leaving the tail in a partially extended conformation that retains significantly more conformational freedom than the Ca^{2+}-compacted state (Figure 12B).

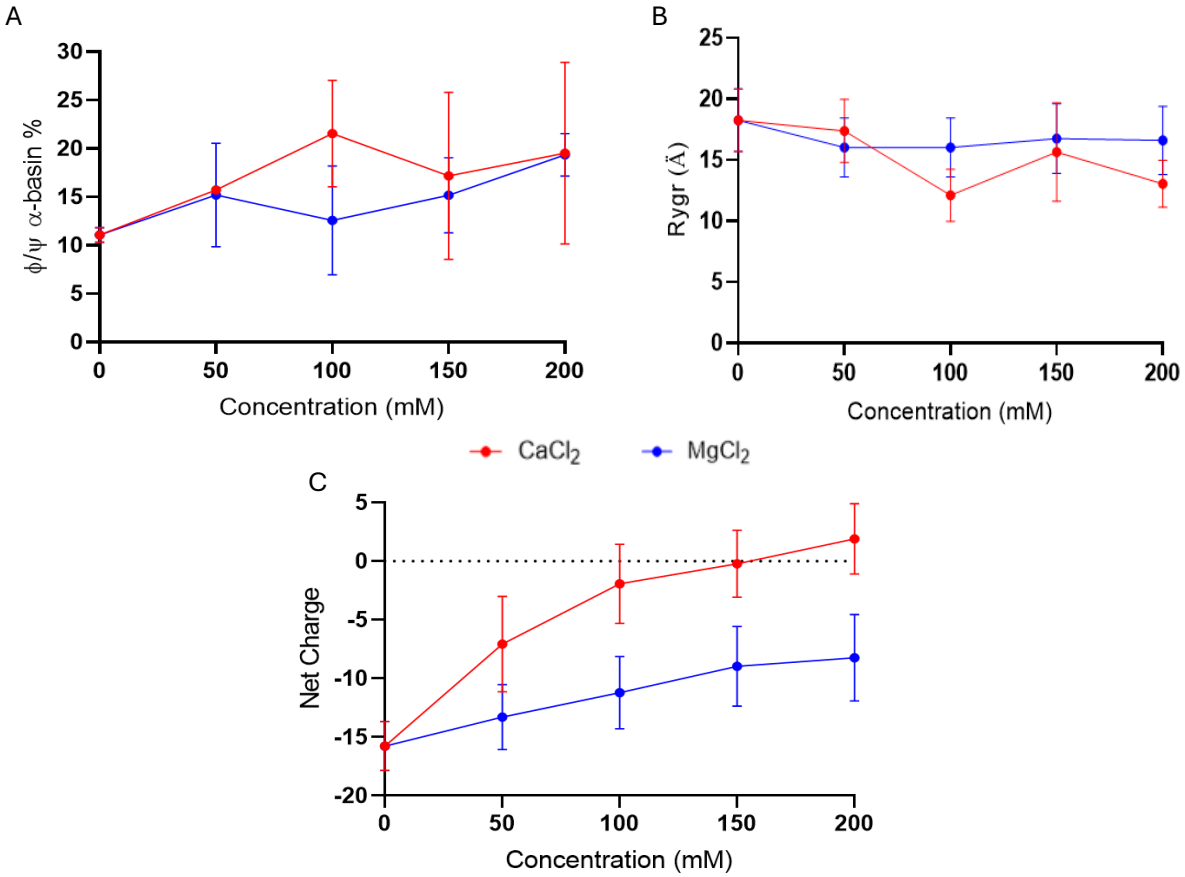

Figure 12. MD simulations of the isolated CASQ2 C-terminal tail reveal a concentration-dependent coil-to-globule transition without stable secondary structure formation. (A) Fraction of backbone φ/ψ angles falling within the α-helical basin of the Ramachandran plot. Neither Ca^{2+} nor Mg^{2+} induces a systematic increase in helical content across the concentration range tested, confirming that the C-terminal tail does not acquire stable α-helical secondary structure in response to either ion. The low and concentration-independent helical fraction (~10–20%) is consistent with transient, non-stable helical sampling. (B) Radius of gyration (Rg) of the C-terminal tail peptide as a function of divalent cation concentration. Both ions induce a progressive reduction in Rg, indicating a coil-to-globule compaction transition, but the effect is substantially more pronounced for Ca^{2+} than Mg^{2+}. Ca^{2+} drives the tail toward a more compact state at all concentrations tested, while Mg^{2+} produces a smaller and less consistent reduction, reflecting the less efficient inner-sphere coordination capacity of Mg^{2+} at the flexible disordered tail. (C) Net charge of the C-terminal tail peptide as a function of divalent cation concentration, calculated from ion coordination analysis. In the absence of divalent cations, the tail carries a net charge of approximately −15 in the presence of 100 mM KCl background, confirming that monovalent screening alone is insufficient to neutralize the tail. Ca^{2+} progressively neutralizes the tail charge and achieves charge inversion at approximately 150 - 200 mM, while Mg^{2+} reduces the net charge more slowly and does not achieve full neutralization within the concentration range tested, leaving a residual net negative charge of approximately −8 at 200 mM. The differential charge neutralization efficiency of the two ions directly accounts for the divergent compaction behaviour shown in panel B. Data are mean ± SD across three independent replicates.

The physicochemical basis for this difference in compaction efficiency is directly connected to the distinct charge neutralization capacities of the two ions. The net charge of the isolated C-terminal peptide in the absence of any counterions is −23 at pH 7.3, reflecting the high density of aspartate and glutamate residues in the DEX^n-motif. In the presence of 100 mM KCl alone, without any divalent cation, the net charge is reduced to approximately −15, confirming that monovalent K^+ provides meaningful but incomplete charge screening and is not sufficient on its own to drive self-compaction of the tail. The addition of divalent cations produces a further concentration-dependent reduction in net charge, but the two ions differ substantially in their neutralization efficiency. At 200 mM $CaCl_2$, complete charge neutralization is achieved, and charge inversion is observed, the tail acquires a net positive charge as an excess of Ca^{2+} ions associate with its surface. Mg^{2+} at the equivalent concentration does not achieve full neutralization, leaving a residual net negative charge on the tail that maintains electrostatic repulsion between segments and limits the degree of compaction that can be attained. The progressive charge neutralization curves for the two ions (Figure 12C) therefore provide a direct electrostatic explanation for the divergent Rg responses observed in Figure 12B: Ca^{2+} compacts the tail more efficiently because it neutralizes its charge more efficaciously.

The reason Ca^{2+} is more effective than Mg^{2+} at charge neutralization of CASQ2 C-terminal tail resides in the fundamentally different coordination chemistry of the two ions, which is directly visualized through radial pair distribution function (g(r)) analysis of the simulations' trajectories (Figure 13A). For Ca^{2+}, the g(r) between the ion and the carboxylate oxygens of aspartate and glutamate residues displays a sharp primary peak at approximately 2.5 Å. This distance is characteristic of direct inner-sphere coordination, in which Ca^{2+} forms a direct electrostatic bond with the carboxylate oxygen without intervening water molecules. This mode of coordination allows Ca^{2+} to simultaneously interact with two or more acidic residues on the same or adjacent segments of the tail, forming inter-residue electrostatic bridges that physically draw chain segments together and drive compaction. For Mg^{2+}, the g(r) displays a broader and lower-amplitude peak centred near 4 Å, a distance that does not corresponds to direct contact with the carboxylate oxygen but to second-shell coordination, in which the ion-residue interactions is mediated by the intervening layer of hydration water molecules retained in the Mg^{2+} coordination sphere.

This difference arises from the intrinsic physical chemistry of the two divalent cations. Mg^{2+} has a smaller ionic radius and a substantially higher charge density than Ca^{2+}, which generates a much stronger electrostatic interaction with surrounding water molecules. The result is the formation of an exceptionally stable octahedral hexahydrate coordination shell, whose disruption requires a large energetic investment. The solvation analysis of the simulation trajectories confirms this picture

quantitatively (Figure 13B): throughout the titration, the average number of water molecules retained in the first coordination shell of Mg^{2+} when it interacts with carboxylate groups remains stable at approximately 6, indicating that the hexahydrate shell is largely preserved even during interaction with the protein surface (Figure 13C). By contrast, Ca^{2+} retains on average only approximately 3 water molecules in the first shell during carboxylate coordination, reflecting the partial de-solvation that accompanies its transition to inner-sphere binding (Figure 13D).

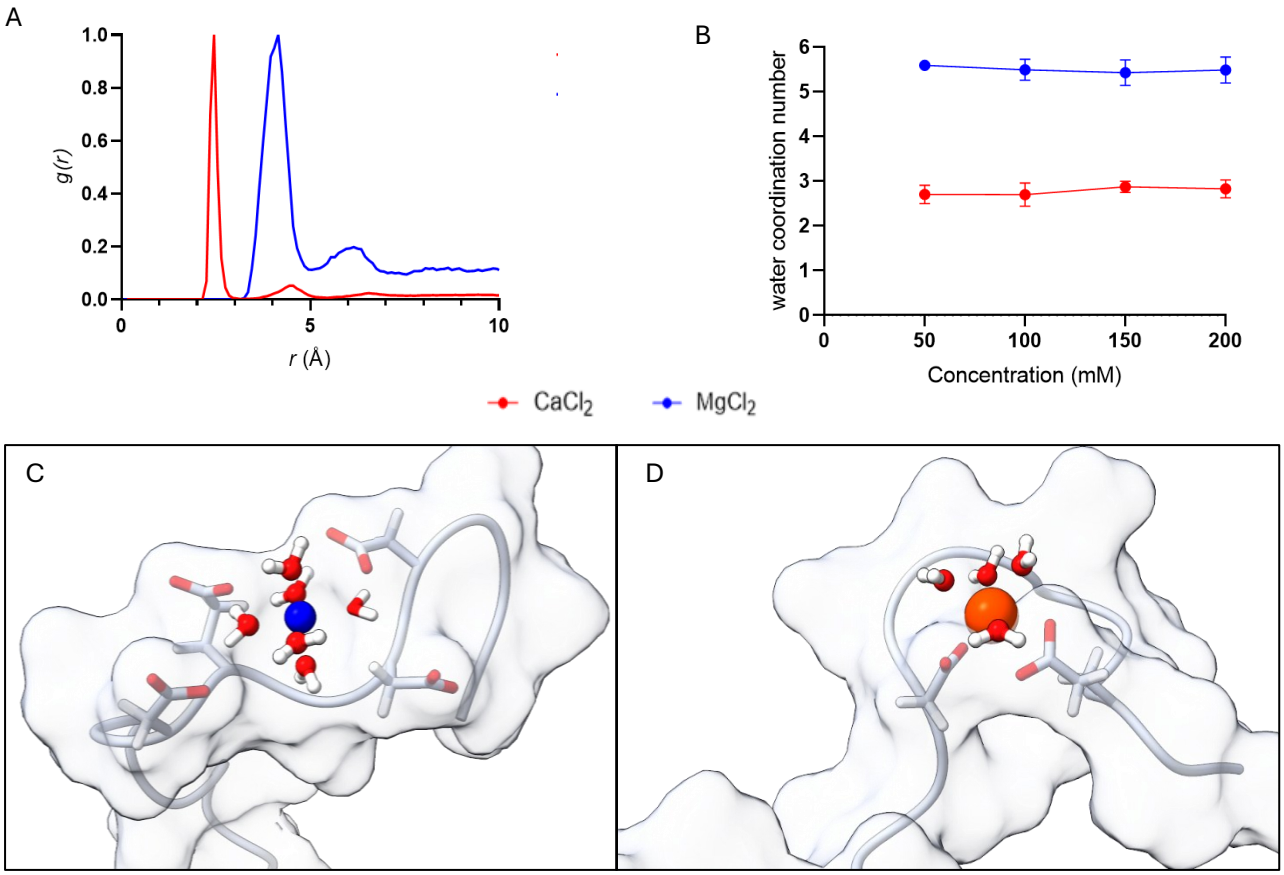

Figure 13. Ca^{2+} and Mg^{2+} display distinct coordination geometries at the CASQ2 C-terminal tail. (A) Radial pair distribution function g(r) between coordinated ions and carboxylate oxygens of aspartate and glutamate residues of the C-terminal tail, calculated from MD simulations at 100 mM $CaCl_2$ (red) or $MgCl_2$ (blue) in 100 mM KCl background. Ca^{2+} displays a sharp primary peak at approximately 2.5 Å, consistent with direct inner-sphere coordination to carboxylate oxygens. Mg^{2+} displays a broader peak centred near 4 Å, indicative of predominantly outer-sphere coordination mediated by retained hydration water molecules. (B) Average number of water molecules retained within 2.3 Å of the coordinated ion during carboxylate interactions, as a function of divalent cation concentration. Ca^{2+} (red) retains approximately 2.7–3.0 water molecules throughout the titration, reflecting partial de-solvation upon inner-sphere coordination. Mg^{2+} (blue) retains approximately 5.3–5.5 water molecules, consistent with maintenance of its octahedral hexahydrate coordination shell during outer-sphere interactions. Both values are stable across the concentration range tested. (C-D) Representative MD simulation snapshots illustrating the coordination geometry of Mg^{2+} (C, blue sphere) and Ca^{2+} (D, orange sphere) at the C-terminal tail. Mg^{2+} is surrounded by a full octahedral shell of hydration water molecules (red and white sticks) that mediate its interaction with the tail carboxylate groups, while Ca^{2+} coordinates directly with carboxylate oxygens with fewer intervening water molecules, enabling inter-residue crosslinking and promoting tail compaction. Data are mean ± SD across three independent replicates.

The water exchange rate of Mg^{2+} is known to be 3–4 orders of magnitude slower than that of Ca^{2+}[55], making the energetic cost of displacing even a single water molecule from the Mg^{2+} hydration shell particularly high. The structural reorganization of CASQ2 flexible C-terminal tail does not overcome

the energy barrier for Mg^{2+} de-solvation, and Mg^{2+} remains in outer-sphere coordination mode throughout the titration. Ca^{2+}, with its more labile solvation shell, can readily form direct inner-sphere coordination bonds with the carboxylate groups of the DEX^{n}-motif, enabling the inter-residue crosslinking that drives efficient compaction. The slow compaction and incomplete charge neutralization observed for Mg^{2+} are therefore the result of a coordination geometry where hexahydrate Mg^{2+} cannot bridge between tail residues as efficiently as Ca^{2+} inner-sphere interactions.

4.3 Ca^{2+} and Mg^{2+} interact with CASQ2 through distinct coordination dynamics

Having characterised the conformational response of the isolated C-terminal tail to Ca^{2+} and Mg^{2+}, we next investigated how the two ions interact with the complete CASQ2 dimer, where the structured globular core provides a preorganised and less flexible electrostatic environment alongside the disordered tail. Molecular dynamics simulations were performed on the full homo-dimeric structure including the modelled C-terminal tail under three ionic conditions: potassium only, calcium, and magnesium, all in a background of 100 mM KCl. The primary question addressed in this section is whether CASQ2 possesses ion-selective binding sites that structurally discriminate between Ca^{2+} and Mg^{2+}, or whether the two ions interact with the same regions of the protein surface through physiochemically distinct mechanisms.

To map the distribution of ion-protein contacts across the full dimer sequence, the coordination occupancy of Ca^{2+} and Mg^{2+} was calculated at a threshold distance of 3 Å from the carboxylate oxygens of all aspartate and glutamate residues throughout the simulation trajectories (Figure 14A). The resulting contact maps reveal that both ions are coordinated primarily by the negatively charged residues (Aspartic and Glutamic amino acids) distributed across the three thioredoxin domains and the C-terminal tail, with no concentration of contacts at structurally specialized or geometrically defined binding sites. Quantitative comparison of the sets of residues contacted by each ion reveals a 93% overlap: of all the acidic residues that interact with either ion, the vast majority are contacted by both Ca^{2+} and Mg^{2+}. Ca^{2+} additionally contacts seven residues that are not sampled by Mg^{2+}, a difference that reflects its higher surface mobility and capacity to explore a larger fraction of the protein's acidic surface through faster exchange dynamics rather than binding at Ca^{2+}-selective recognition sites. This strong convergence in coordination sites further demonstrate that CASQ2 does not function as a metalloprotein with dedicated ion-selective binding pockets: the structured core does not discriminate between Ca^{2+} and Mg^{2+} at the level of which residues are contacted.

Despite the near-identical distribution of contact sites, the dynamics of ion-protein interaction differ substantially. Ca^{2+} displays a high degree of surface mobility, rapidly exchanging between coordination sites and frequently sliding across the negatively charged protein surface. This behaviour is consistent with its labile solvation shell and fast water exchange rate, which allow it to transiently coordinate carboxylate groups without committing to long-lived stable interactions at any individual site. Mg^{2+} presents a qualitatively different picture: once coordinated to an acidic residue, it remains localized at that site for substantially longer periods, producing more persistent but fewer simultaneous contacts. This is directly quantified by the average coordination occupancy, the fraction of simulation time during which a given residue is found within 3 Å of a coordinated ion, which is approximately twofold higher for Mg^{2+} than for Ca^{2+} across the protein surface (Figure 14B). This twofold difference in residence time reflects the intrinsically slower coordination exchange kinetics of Mg^{2+} and is a property of the ion itself rather than of specific protein binding geometries.

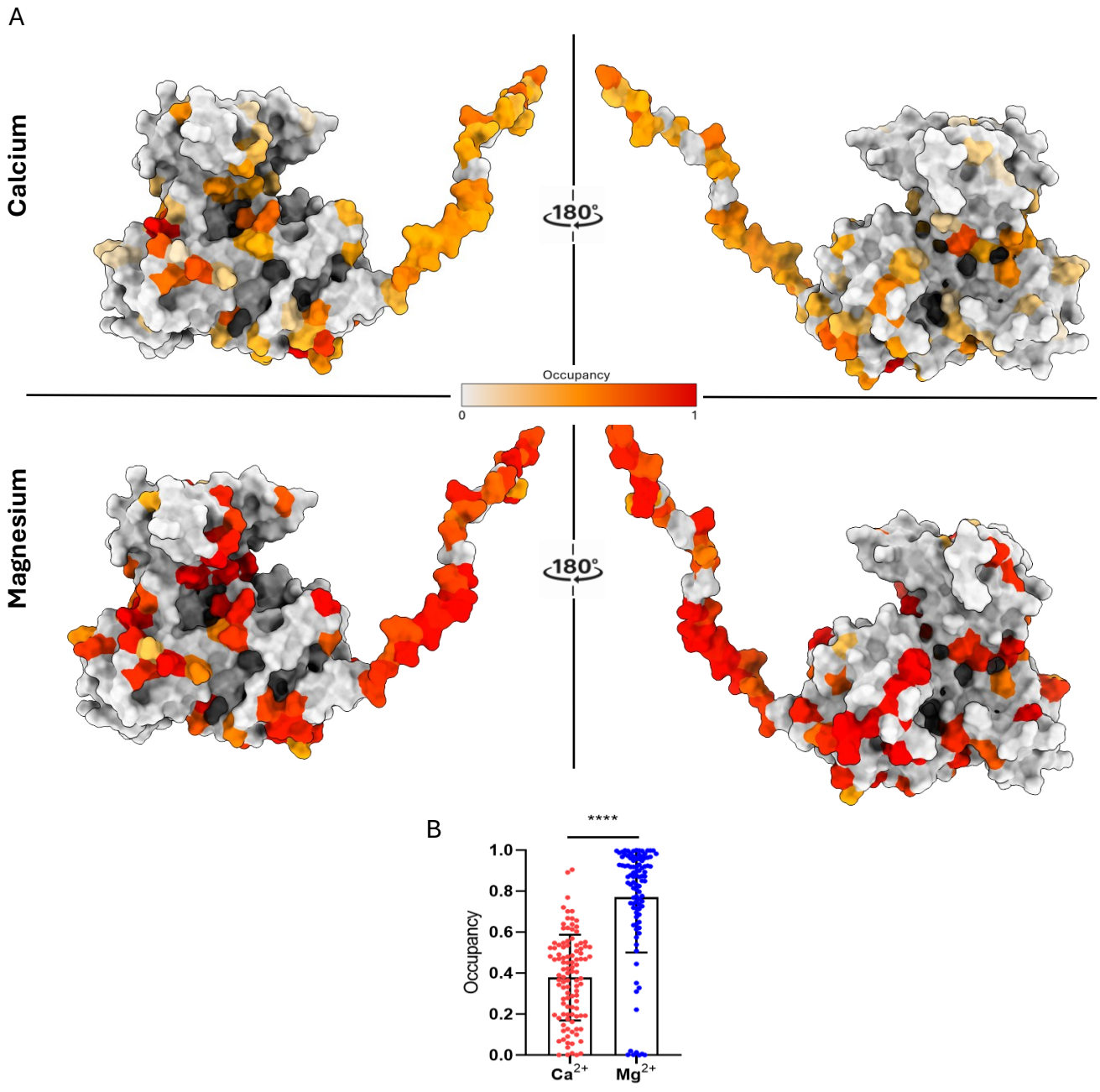

Figure 14. Ion-protein contact occupancy maps reveal overlapping but dynamically distinct coordination patterns for Ca^{2+} and Mg^{2+} across the CASQ2 dimer surface. (A) Surface representation of the CASQ2 monomer coloured by ion coordination occupancy (colour scale: white = 0, red = 1), shown from two opposing views (180° rotation) for Ca^{2+} (top row) and Mg^{2+} (bottom row). The C-terminal tails are shown as extended surface representations flanking the globular core. Both ions contact predominantly negatively charged residues distributed across all three thioredoxin domains and the C-terminal tail, with no evidence of spatially restricted ion-selective binding sites. The C-terminal tail appears to be the highest binding occupancy spot for both ions. Mg^{2+} (bottom) shows a more uniformly high and spatially extensive occupancy pattern across the globular surface relative to Ca^{2+} (top), consistent with its longer coordination residence times and more persistent site-specific interactions, while Ca^{2+} shows a more heterogeneous occupancy distribution reflecting its higher surface mobility and faster exchange dynamics. (B) Quantification of per-residue coordination occupancy for Ca^{2+} (red dots) and Mg^{2+} (blue dots) across all acidic residues of the dimer. Mg^{2+} shows a significantly higher mean occupancy than Ca^{2+} (approximately 0.75 vs 0.38), with a narrower distribution concentrated at high values, while Ca^{2+} shows a broader distribution spanning the full occupancy range. This approximately twofold difference in mean occupancy directly reflects the longer coordination residence times of Mg^{2+} relative to Ca^{2+}, consistent with the known difference in water exchange rates between the two ions.

An important and unexpected finding emerged from the analysis of solvation behaviours in the context of the full dimer (Figure 15A). While in the isolated C-terminal tail simulations, Mg^{2+} was observed to coordinate exclusively through outer-sphere interactions, in the full dimer, a different behaviour was observed: upon coordination to the protein surface of the globular domains, Mg^{2+} undergoes partial de-solvation, allowing a degree of direct inner-sphere coordination with carboxylate groups of aspartate and glutamate residues. Free Mg^{2+} in solution retains six water molecules in its octahedral coordination shell; when coordinated at globular domain sites, this number drops to an average of 3.42 water molecules, a loss of approximately 2.6 water molecules per coordination event, reflecting the ability of the structured globular acidic clusters to provide sufficient electrostatic stabilization to partially overcome the energetic cost of Mg^{2+} de-solvation. Ca^{2+} follows a qualitatively similar pattern but with less pronounced domain-dependence, with 3.89 water molecules retained for binding at the globular domain compared to 4.15 at the C-terminal tail. Here the difference in number of water molecules retained when binding at the protein core Vs. the flexible C-terminus is only 0.26, much smaller than the 1.0 difference observed for Mg^{2+}. This comparison reveals a striking asymmetry: the degree to which Mg^{2+} coordination behaviour differs between the structured globular core and the disordered C-terminal tail is approximately four times greater than the equivalent difference for Ca^{2+}. The structural organisation of the globular domains, with their dense, geometrically arranged clusters of acidic residues, provides the electrostatic preorganization required to partially de-solvate Mg^{2+} and allow inner-sphere-like coordination, while the conformationally flexible and less organized C-terminal tail cannot achieve the same stabilization.

These differences in coordination dynamics between the two ions translate into a measurable difference in the total number of ions simultaneously associated with the dimer surface at any given moment. Under identical ionic concentrations, the CASQ2 dimer coordinates on average approximately 53 Ca^{2+} ions (with a maximum of 58) compared to approximately 44 Mg^{2+} ions (maximum 49) (Figure 15B). The higher number of simultaneously coordinated Ca^{2+} ions reflect its faster exchange dynamics, Ca^{2+} rapidly samples more sites per unit time, while the fewer but longer-lived Mg^{2+} contacts result in a lower instantaneous global surface occupancy. The net consequence is a clear difference in overall surface charge neutralisation between the two conditions (Figure 15C): Ca^{2+} achieves a substantially higher degree of charge compensation of the CASQ2 dimer surface than Mg^{2+} under equivalent ionic conditions.

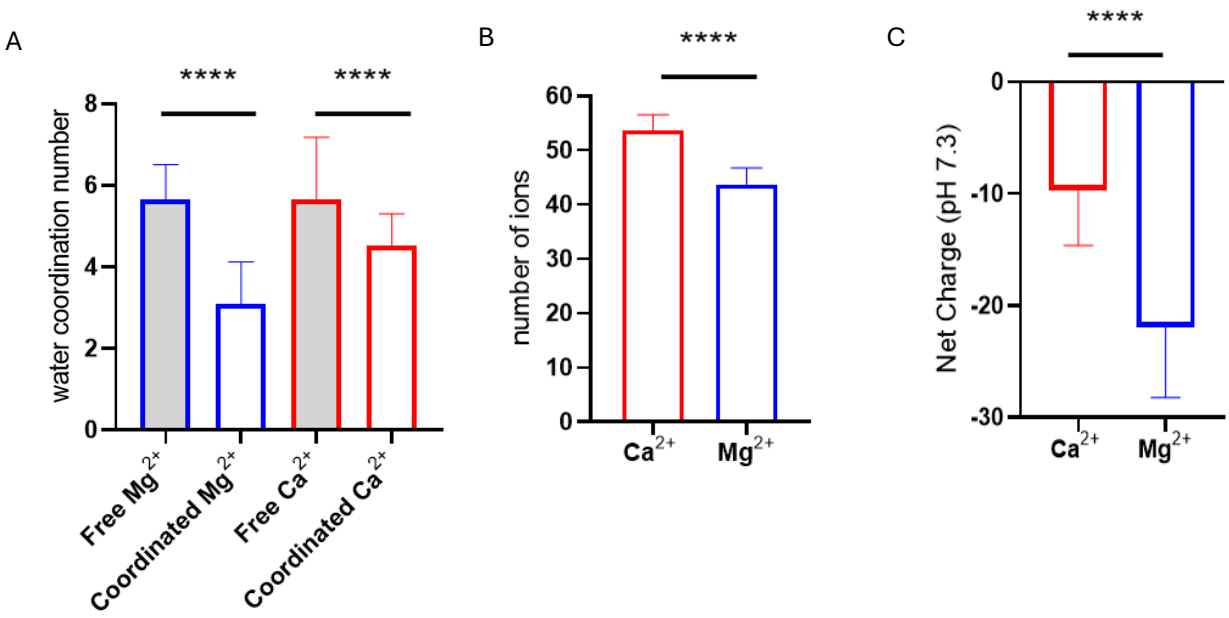

Figure 15. Distinct solvation, surface occupancy, and charge neutralization of the CASQ2 dimer by Ca^{2+} and Mg^{2+}. (A) Average number of water molecules in the first coordination shell (2.3 Å) of free (bulk solution) and protein-coordinated Mg^{2+} (blue) and Ca^{2+} (red) ions, calculated from MD simulations of the full CASQ2 dimer (globular core + C-terminal tail, see Figure 13 panel B). Free Mg^{2+} retains approximately 5.7 water molecules in solution, consistent with its stable octahedral hexahydrate geometry. Upon coordination to the protein surface, Mg^{2+} retains approximately 3.0 water molecules, indicating partial but incomplete desolvation. Free Ca^{2+} retains approximately 5.6 water molecules in solution, comparable to Mg^{2+}, but upon protein coordination retains approximately 4.5 water molecules, substantially more than coordinated Mg^{2+}. This counter-intuitive result, in which the coordinated state of Mg^{2+} is more desolvated than that of Ca^{2+} in the context of the full dimer, reflects the ability of the organized globular acidic clusters to provide appropriate coordination geometry and sufficient electrostatic stabilization to overcome the energetic cost of partial Mg^{2+} desolvation, differently from the disordered C-terminal tail. (B) Average number of Ca^{2+} (red) and Mg^{2+} (blue) ions simultaneously coordinated (in a range of 3.0 Å from the carboxylate group of aspartic and glutamic amino acid) to the CASQ2 dimer surface under identical ionic concentrations (100mM KCl). Ca^{2+} coordinates approximately 53 ions on average (maximum 58) compared to approximately 44 for Mg^{2+} (maximum 49), reflecting the higher surface mobility and faster exchange dynamics of Ca^{2+} relative to Mg^{2+}. Data are mean ± SD across three independent replicates. (C) Net charge of the CASQ2 dimer (pH 7.3) in the presence of 75mM of Ca^{2+} (red) or Mg^{2+} (blue), calculated from ion coordination analysis. Ca^{2+} achieves substantially greater charge neutralization of the dimer surface than Mg^{2+} under equivalent ionic conditions. All the data are mean ± SD across three independent replicates. Significance assessed by unpaired two-tailed Student's t-test; **** $p < 0.0001$.

This computational result is in direct quantitative agreement with the ζ-potential measurements performed in vitro on the wild-type CASQ2 and deleted C-terminus tail mutants. In the $CaCl_2$ panel, all three proteins display nearly identical charge neutralisation curves throughout the entire concentration range tested (Figure 16A). All three CASQ2 variants cross the zero potential threshold at approximately 20 mM $CaCl_2$ and reach the same positive plateau of approximately +20 mV at 100 mM, indicating complete charge inversion at high Ca^{2+} concentrations. The $MgCl_2$ panel presents a more complex and mechanistically informative picture (Figure 16B). Consistent with the MD simulation data, all three constructs require substantially higher Mg^{2+} concentrations to achieve charge neutralization than Ca^{2+}, with neutralization (0 mV) occurring at approximately 50 mM $MgCl_2$ compared to ~20 mM for Ca^{2+}, and a lower plateau reached at approximately +10mV. This behaviour

confirms MD data on the fact that Mg^{2+} is inherently less efficient than Ca^{2+} at neutralizing CASQ2 surface charges regardless of tail length.

The main difference in neutralization behaviour across CASQ2 variants resides at low Mg^{2+} concentrations (1–20 mM). Wild-type CASQ2 and D383X follow nearly identical trajectories throughout the entire concentration range, while E373X shows a markedly faster charge neutralization between approximately 1 and 20 mM Mg^{2+}. The E373X curve rises more steeply in this region, crossing the wild-type and D383X curves before all three converge at higher divalent concentrations. This behaviour can be precisely interpreted in terms of the coordination chemistry described after the MD analysis. As demonstrated by the radial pair distribution function and solvation analysis of the MD simulations, Mg^{2+} coordinates to the disordered C-terminal tail primarily through outer-sphere interactions, retaining approximately 4–5 water molecules in its first coordination shell at this flexible, structurally unorganized segment. These outer-sphere interactions sequester Mg^{2+} ions at the C-terminal tail. In turn, Mg^{2+}-buffering by the tail segment delays net surface charge neutralization, especially at low concentrations. In E373X, this outer-sphere buffer is absent: Mg^{2+} ions that would have been partially sequestered at the proximal tail in non-productive outer-sphere interactions are instead immediately available to coordinate the globular domain acidic residues where, as shown in the MD analysis, Mg^{2+} achieves substantially stronger de-solvation and more efficient inner-sphere-like coordination, resulting in faster charge neutralization at low concentrations.

The near-identical wild-type and D383X Mg^{2+} curves establishes that the Mg^{2+} outer-sphere buffering effect is a property specific to the proximal segment (residues 373–382), with the distal segment (383–399) contributing no additional buffering beyond what the proximal segment already provides. Strikingly the turbidimetric experiments presented in section 4.1 identified exactly the proximal segment as the primary Mg^{2+} sensor, necessary and sufficient to confer Mg^{2+} responsiveness on the Ca^{2+} assembly response. The co-localization of these two functions, Mg^{2+} sensing and Mg^{2+} charge buffering, suggests they may arise from the same molecular property: the capacity of this segment to engage Mg^{2+} in outer-sphere.

A systematic difference between the three CASQ2 variants tested (in both $MgCl_2$ and $CaCl_2$ condition) is their ζ-potential in the absence of divalents in 50Mm KCl: wild-type, D383X, and E373X CASQ2 net surface charge is respectively −109 mV, −99 mV, and −79 mV. This progressive reduction in surface negativity mirrors the successive removal of C-terminal tail segments. The ~30 mV difference between wild-type and E373X reflects the direct contribution of the DEX^n-motif to

the total surface charge of the intact protein. The identical zero-crossing point and identical final plateau for all three proteins confirms that Ca^{2+} binds primarily through the distributed acidic surface of the globular core regardless of whether the C-terminal tail is present. Hence the tail contributes to the initial charge density but does not alter the mechanism or capacity of Ca^{2+} coordination.

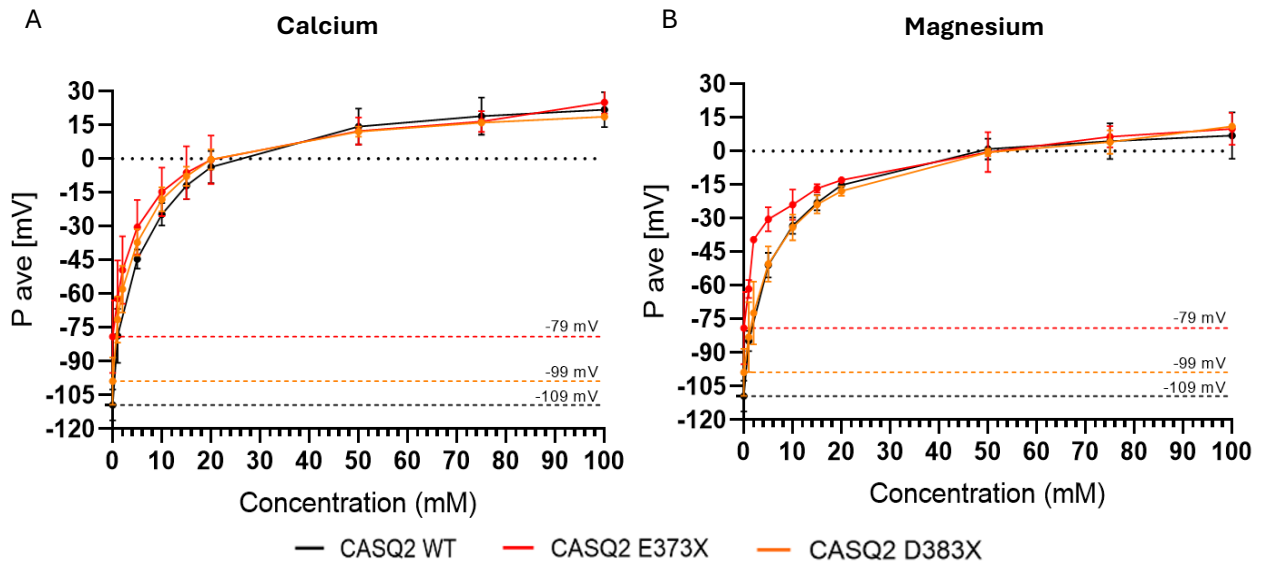

Figure 16. ζ -potential measurements confirm differential charge neutralization efficiency of Ca^{2+} and Mg^{2+} across CASQ2 WT and C-terminal truncation mutants. ζ-potential (mV) of wild-type CASQ2 (black), CASQ2-E373X (red), and CASQ2-D383X (orange) at 2.5 µM in 50 mM KCl as a function of increasing $CaCl_2$ (A) or $MgCl_2$ (B) concentration (0–100 mM). Horizontal dashed lines indicate the resting ζ-potential of each protein in the absence of divalent cations: −109 mV (WT), −99 mV (D383X), and −79 mV (E373X), reflecting the progressive reduction in surface negative charge upon successive removal of C-terminal tail segments. For Ca^{2+} (A), all three proteins display nearly identical sigmoidal neutralization curves, crossing zero at approximately 20 mM and reaching the same positive plateau (~+15 mV) at 100 mM, confirming that Ca^{2+} achieves equivalent charge neutralization and inversion regardless of tail length. The tail contributes to the initial surface charge density but does not alter the Ca^{2+} binding mechanism or capacity of the globular core. For Mg^{2+} (B), all three proteins cross zero at approximately 50 mM, substantially higher than for Ca^{2+}, and converge on the same positive plateau at 100 mM, confirming that Mg^{2+} is less efficient than Ca^{2+} at charge neutralization regardless of tail length. Wild-type and D383X follow nearly identical trajectories throughout, while E373X shows faster charge neutralization at low concentrations (1–15 mM), consistent with the proximal tail segment (residues 373–382) acting as an outer-sphere Mg^{2+} charge buffer that delays net charge neutralization. Data are mean ± SD of three independent experiments.

Taken together, the ion-protein contact analysis of the full dimer corroborate a coherent and physically grounded picture of how Ca^{2+} and Mg^{2+} interact with CASQ2. Both ions are distributed across the same surface residues with no evidence of ion-selective binding pockets, confirming the polyelectrolyte-like rather than metalloprotein character of CASQ2 ion binding. The differences between the two ions arise entirely from their intrinsic physicochemical properties, coordination geometry, solvation shell stability, and water exchange rate, rather than from any selective structural recognition motif. Ca^{2+} achieves higher surface distribution, greater charge neutralization, and more efficient compaction through its capacity for rapid inner-sphere coordination and inter-residue crosslinking. Mg^{2+} achieves lower surface occupancy and less charge neutralization but forms longer-

lived individual contacts, with a solvation behaviour that is strongly dependent on the structural organization of the binding environment, inner-sphere-like at the globular domains, outer-sphere at the disordered C-terminal tail.

4.4 The vibrational state of the CASQ2 C-terminal tail is differentially influenced depending on the type of ion present.

The distinct interaction modes of Ca^{2+} and Mg^{2+} with the CASQ2 dimer surface, confirmed in the previous section, raise the question of whether these physicochemical differences translate into measurable differences in the conformational and dynamical behaviours of the protein itself, and in particular of its C-terminal tail. To address this, I analysed the root mean square fluctuation (RMSF) of every residue in the CASQ2 sequence across the three ionic conditions, providing a residue-resolved map of backbone flexibility under K^+, Ca^{2+}, and Mg^{2+} (Figure 17A).

Within the globular region of the dimer (residues 22–370), the RMSF profiles under the three conditions are broadly comparable. Both Ca^{2+} and Mg^{2+} produce a modest reduction in backbone flexibility relative to K^+ alone, consistent with a general electrostatic stabilization of the structured core upon divalent cation binding, but the magnitude of this effect is similar for the two ions and does not differ substantially between individual domains. The three thioredoxin domains maintain their characteristic fold and flexibility profile regardless of whether Ca^{2+} or Mg^{2+} is present, confirming that the ionic environment does not fundamentally reorganize the structured core of the dimer.

A strikingly different picture emerges at the C-terminal tail (residues 370–399). Here, the three ionic conditions produce clearly divergent RMSF profiles. In the K^+-only condition, the tail exhibits the highest backbone fluctuations of any region in the entire protein sequence, reflecting its intrinsically disordered character and the absence of charge screening sufficient to constrain its dynamics. Both Ca^{2+} and Mg^{2+} reduce backbone fluctuations within the tail substantially relative to K^+, indicating ion-dependent vibrational stabilization of this disordered segment. Crucially, the degree of stabilization is not equivalent between the two ions: Mg^{2+} produces a markedly more pronounced reduction in RMSF values across most of the tail than Ca^{2+}, resulting in a more constrained dynamical ensemble despite its lower charge neutralization efficiency. This apparent paradox, Mg^{2+} stabilizes tail dynamics more strongly than Ca^{2+} even though Ca^{2+} neutralizes its charges more completely, is directly explained by the longer coordination residence times of Mg^{2+} established in the previous section. Once Mg^{2+} coordinates a carboxylate group on the tail, it persists at that site for substantially longer than Ca^{2+}, imposing a more durable mechanical constraint on the backbone motion of the

coordinated residue and its neighbours. Ca^{2+}, with its faster exchange dynamics, provides charge neutralization that is more thermodynamically efficient but kinetically more transient, and therefore less effective at suppressing backbone fluctuations on the timescale of the simulation. The ion-dependent modulation of tail backbone flexibility is accompanied by a corresponding change in the average spatial relationship between the C-terminal tail and the globular core of the dimer. Analysis of the centre-of-mass (COM) distance between the tail and the dimer core over the simulation trajectories (Figure 17B) shows that in the K^+-only condition the tail samples broadly distributed and predominantly extended conformations, remaining on average significantly more distal from the globular surface. The distribution of COM distances under K^+ is wider than in presence of divalents, reflecting the high conformational freedom of the unscreened tail as it explores a large volume of conformational space around the dimer. In the presence of Ca^{2+} or Mg^{2+}, the average COM distance decreases substantially, i.e. more than 10 Å, indicating that divalent cation coordination promotes closer and more persistent association of the tail with the globular core surface.

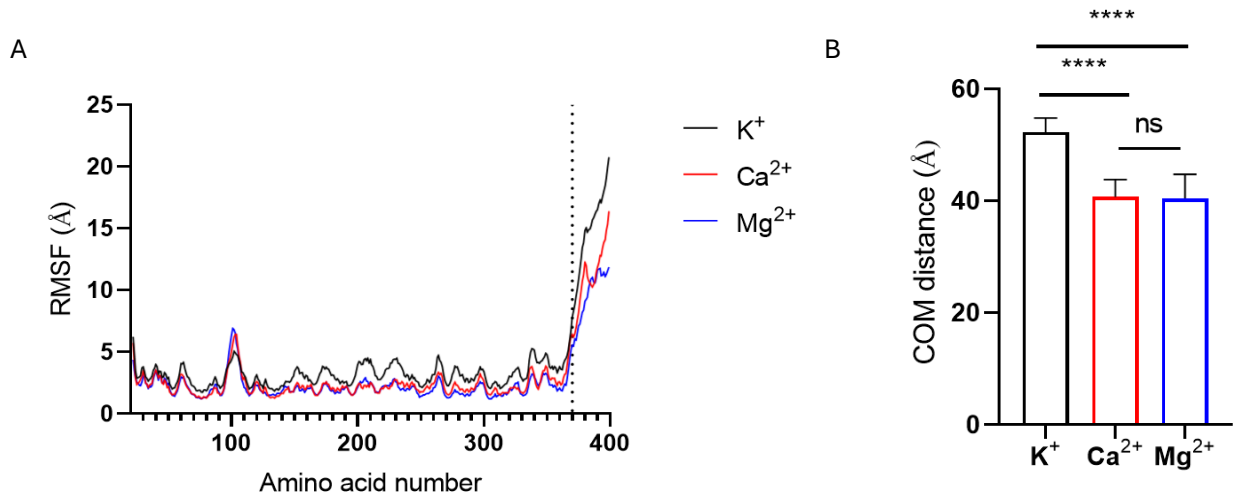

Figure 17. Divalent cations differentially reduce C-terminal tail backbone flexibility and promote tail-core association in the CASQ2 dimer. (A) Root means square fluctuation (RMSF) per residue of the CASQ2 homodimer under K^+ (black), Ca^{2+} (red), and Mg^{2+} (blue) conditions, calculated from full dimer MD simulations. The vertical dotted line marks the boundary between the globular core (residues 22–370) and the C-terminal tail (residues 371–399). Within the globular region, the three ionic conditions produce comparable RMSF profiles with only modest and equivalent reductions in flexibility induced by either divalent cation. At the C-terminal tail, pronounced ion-dependent differences emerge, both Ca^{2+} and Mg^{2+} substantially reduce backbone fluctuations relative to K^+, with Mg^{2+} producing a more marked reduction than Ca^{2+} across most tail residues, consistent with its longer coordination residence times imposing more persistent mechanical constraints on tail backbone motion. (B) Average centre-of-mass (COM) distance between the C-terminal tail (residues 371–399) and the globular core (residues 22–370 calculated on both the chains) under K^+, Ca^{2+}, and Mg^{2+} conditions. In the K^+-only condition the tail samples more extended conformations and remains on average more distal from the globular surface (~51 Å). Both Ca^{2+} and Mg^{2+} promote closer tail-core association (~41 Å), reflecting electrostatic-driven recruitment of the tail toward the globular surface as divalent cation coordination reduces the net negative charge of the tail and relieves inter-domain electrostatic repulsion. Data are mean ± SD across three independent replicates. Significance assessed by unpaired two-tailed Student's t-test; **** $p < 0.0001$.

An unexpected but important consequence of the C-terminal tail's dynamical state on the structured core is revealed by comparing the solvent-accessible surface area (SASA) of the five tryptophan residues, exclusively located within the third thioredoxin-like domain, between the wild-type CASQ2 dimer and a dimer model deleted of the C-terminal tails, both simulated in the K^+-only condition (Figure 18A). Counterintuitively, removal of the C-terminal tail results in a significant reduction of tryptophan SASA rather than an increase. This means that the hydrophobic core of the third domain is more solvent-exposed when the C-terminal tail is present than when it is absent. This finding is most accurately interpreted in terms of mechanical coupling between the disordered tail and the structured core: in the K^+-only condition, the C-terminal tail is highly dynamic, sampling a broad conformational space with large-amplitude fluctuations as defined by the RMSF analysis.

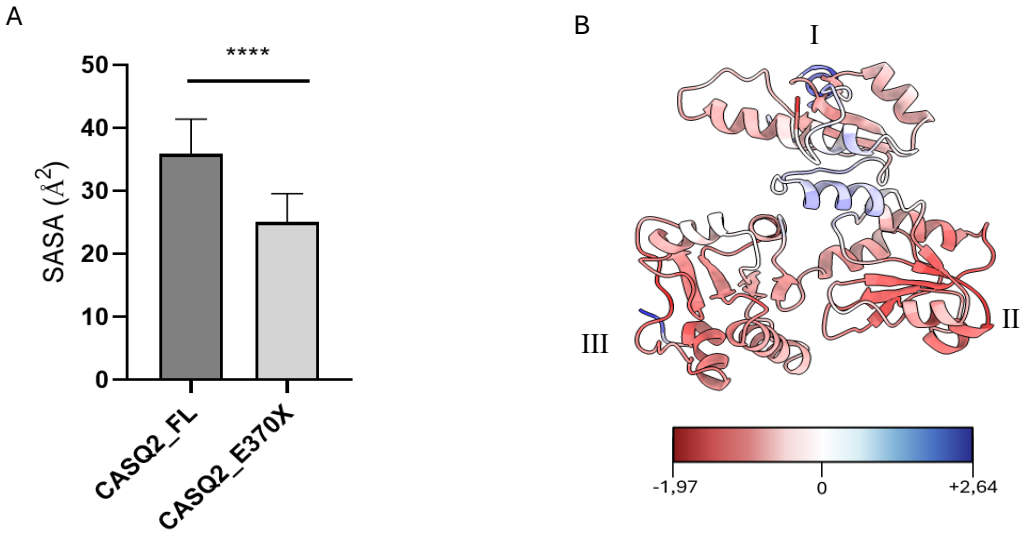

Figure 18. The C-terminal tail increases solvent exposure of the third thioredoxin domain and globally enhances conformational flexibility of the CASQ2 globular core. (A) Solvent-accessible surface area (SASA) of the five tryptophan residues, exclusively located within the third thioredoxin domain, in full-length CASQ2 (CASQ2_FL, dark grey) and the C-terminal tail-truncated model (CASQ2_E370X, light grey), both simulated under K^+-only conditions. Full-length CASQ2 shows significantly higher tryptophan SASA (~35 Å²) than the truncated model (~25 Å²), indicating that the presence of the highly charged C-terminal tail promotes greater solvent exposure of the third domain. (B) RMSF difference map between full-length CASQ2 and the C-terminal tail-truncated model, displayed on the ribbon structure of one CASQ2 monomer. Colour scale represents the RMSF difference per residue: red indicates regions of higher flexibility in full-length CASQ2 relative to the truncated model, blue indicates regions of lower flexibility. A consistent reduction in backbone flexibility is observed across all three domains upon tail removal, with the most pronounced differences concentrated in domain I and at the domain II–III interface, confirming that the electrostatic influence of the C-terminal IDR propagates globally across the entire globular structure rather than being restricted to the third domain adjacent to the tail attachment point. Significance assessed by unpaired two-tailed Student's t-test; **** $p < 0.0001$.

These fluctuations are transmitted to the globular core effectively transferring vibrational energy into the third thioredoxin domain and destabilising it toward a more open, solvent-exposed conformation.

When the tail is removed, this source of mechanical perturbation is eliminated and the third domain behaves as a more compact structure. The tail therefore acts as a vibrational mechanical lever that propagates conformational energy from the disordered segment into the structured core, an effect that divalent cations modulate by damping tail fluctuations.

This interpretation is further supported by RMSF comparison between the full-length and tail-truncated dimer (Figure 18B). The RMSF difference map reveals that removal of the C-terminal tail produces a consistent decrease in backbone flexibility beyond the third thioredoxin domain only, and throughout the entire globular structure. This global dampening of core flexibility upon tail truncation confirms that the conformational dynamics of the intrinsically disordered tail are mechanically coupled to the flexibility of the structured core through electrostatic interactions, and that the tail's dynamical state under different ionic conditions should be expected to produce corresponding modulations of core dynamics.

The MD simulation results suggest also that the regulation provided by the divalent ions on the C-terminal tail modify the flexibility of the globular core and the hydrophobic core exposure to the solvent (Figure 19A), showing that bot Ca^{2+} and Mg^{2+} can modulate and decrease the solvent exposure of the five tryptophan residues in the third thioredoxin-like domain. To directly test whether the ion-dependent changes in tail positioning and dynamics predicted by the MD simulations produce measurable consequences at the level of the third-domain tryptophan environment in the intact protein, thermal stability assays based on intrinsic tryptophan fluorescence were performed on both wild-type CASQ2 and the complete C-terminal deletion mutant E373X in presence of 150mM KCl only or in addition of equivalent concentrations of Ca^{2+} or Mg^{2+} separately tested (Figure 19B). The initial fluorescence emission ratio at 350/330 nm measured at the start of the thermal ramp, before any thermally induced unfolding, provides a sensitive reporter of the average tryptophan microenvironment at resting temperature: a higher ratio indicates tryptophan residues in a more polar, solvent-exposed environment, while a lower ratio reflects a more hydrophobic, buried environment.

In the complete absence of divalent ions, wild-type CASQ2 and E373X already exhibit different basal fluorescence ratios at 35°C: ~ 0.86 for wild-type and ~ 0.81 for E373X. This difference confirms the MD prediction: the C-terminal tail, in the absence of charge screening by divalent cations, promotes a more open and solvent-exposed third-domain tryptophan environment. Its removal in E373X produces the more compact, less solvent-exposed state predicted by the SASA analysis, manifested as a lower baseline fluorescence ratio.

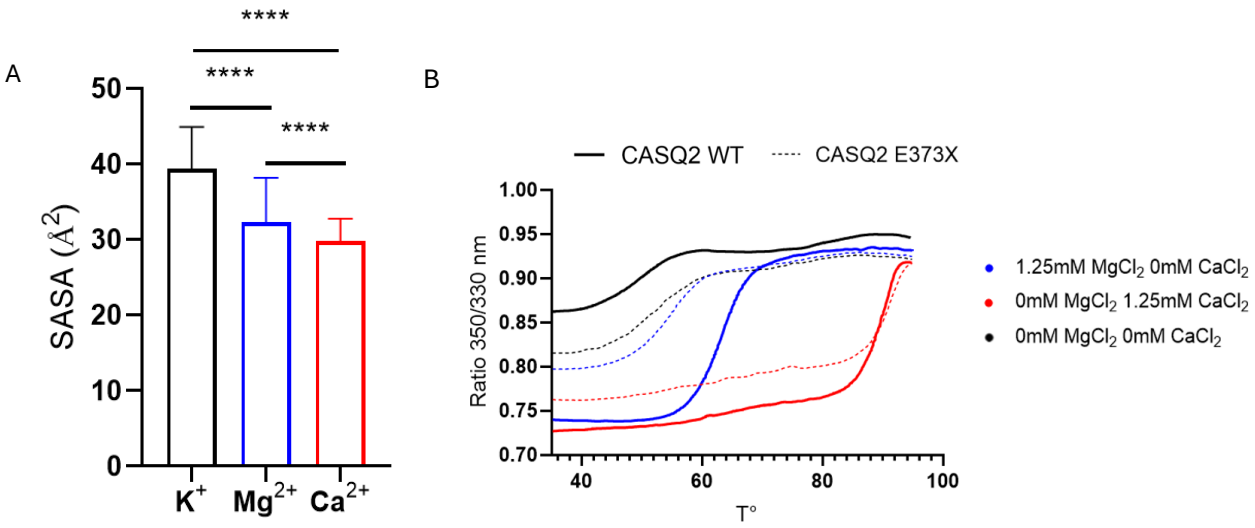

Figure 19. Divalent cations modulate third-domain solvent exposure and thermal stability of CASQ2 in a C-terminal tail-dependent manner. (A) Solvent-accessible surface area (SASA) of the five tryptophan residues of the third thioredoxin domain in full-length CASQ2 under K^+ (black), Mg^{2+} (blue), and Ca^{2+} (red) conditions, from full dimer MD simulations. Both divalent cations reduce tryptophan SASA relative to K^+ alone. Ca^{2+} produces a slightly greater reduction than Mg^{2+}. (B) Intrinsic tryptophan fluorescence thermal stability assay of wild-type CASQ2 (solid lines) and CASQ2-E373X (dashed lines) in the absence of divalent ions (black), in the presence of 1.25 mM $MgCl_2$ (blue), or 1.25 mM $CaCl_2$ (red). The fluorescence ratio 350/330 nm is plotted as a function of temperature from 35°C to 100°C. In the absence of divalent ions, wild-type CASQ2 shows a higher basal ratio at 35°C than E373X (~0.86 vs ~0.81), providing in vitro confirmation of the MD SASA prediction that the C-terminal tail promotes greater tryptophan solvent exposure in the intact protein. Both Ca^{2+} and Mg^{2+} produce a downward shift in the basal fluorescence ratio in wild-type relative to the ion-free condition, with Ca^{2+} producing a larger shift than Mg^{2+} at equivalent concentration. In E373X, the response to both ions is substantially attenuated and asymmetrically so, more pronounced for Mg^{2+} than Ca^{2+}. Significance assessed by unpaired two-tailed Student's t-test; **** $p < 0.0001$.

When 1.25 mM Ca^{2+} or Mg^{2+} are present, a clear downward shift in the initial fluorescence ratio in wild-type CASQ2 indicates progressive compaction and burial of the tryptophan environment. This is consistent with the vibrational stabilization of the tail and recruitment toward the globular core as its charges are neutralized and its electrostatic repulsion on the globular domain is reduced. Importantly, Ca^{2+} produces a larger downward shift than Mg^{2+} at the same concentration, confirming a clear potency difference between the two ions in modulating the third-domain tryptophan environment. Also, Ca^{2+} is more effective than Mg^{2+} at promoting third-domain compaction not only in the intact protein but in the C-terminal tail deleted mutant. This observation appears to stand in tension with the RMSF analysis of the full dimer (Figure 17A), in which Mg^{2+} produced a stronger reduction in C-terminal tail backbone fluctuations than Ca^{2+}. however, the two results are reconcilable in a more complex yet complete picture: Mg^{2+} more effectively suppresses the vibrational dynamics of the tail, whereas Ca^{2+} is the better compactor of the overall dimeric globular core. These are distinct physical phenomena, and the two experimental and computational readouts are sensitive to different aspects of the same underlying ion-tail-core interaction. The tryptophan fluorescence assay reports more specifically on the latter effect: the degree to which the third domain is shielded from solvent because of tail-core association and charge neutralization, which is driven

more efficiently by Ca^{2+}. In E373X, the fluorescence response to both Ca^{2+} and Mg^{2+} is substantially attenuated relative to wild-type. The downward shift in fluorescence ratio upon divalent cation addition is considerably smaller than in the full-length protein, indicating that the absence of the C-terminal tail reduces the sensitivity of the third domain to the ionic environment. Crucially, this desensitization is not symmetric between the two ions: E373X retains a partial compaction response to Ca^{2+}, reflecting the ability of the globular core to respond directly to Ca^{2+} through its own structured acidic clusters, while the Mg^{2+} response is more severely blunted. Without the tail, Mg^{2+} loses much of its ability to modulate the third-domain environment because the primary structural element through which Mg^{2+} exerts its conformational influence on the full-length protein, the long-lived outer-sphere coordination of the flexible DEX^{n}-motif, is absent. In order to better analyse the stabilization of CASQ2 in presence of Ca^{2+} or Mg^{2+}, and how the C terminal IDR is involved in this modulation, I performed a thermal stability analysis over a concentration range of these two divalent ions, from 0 to 20 mM (Figure 20).

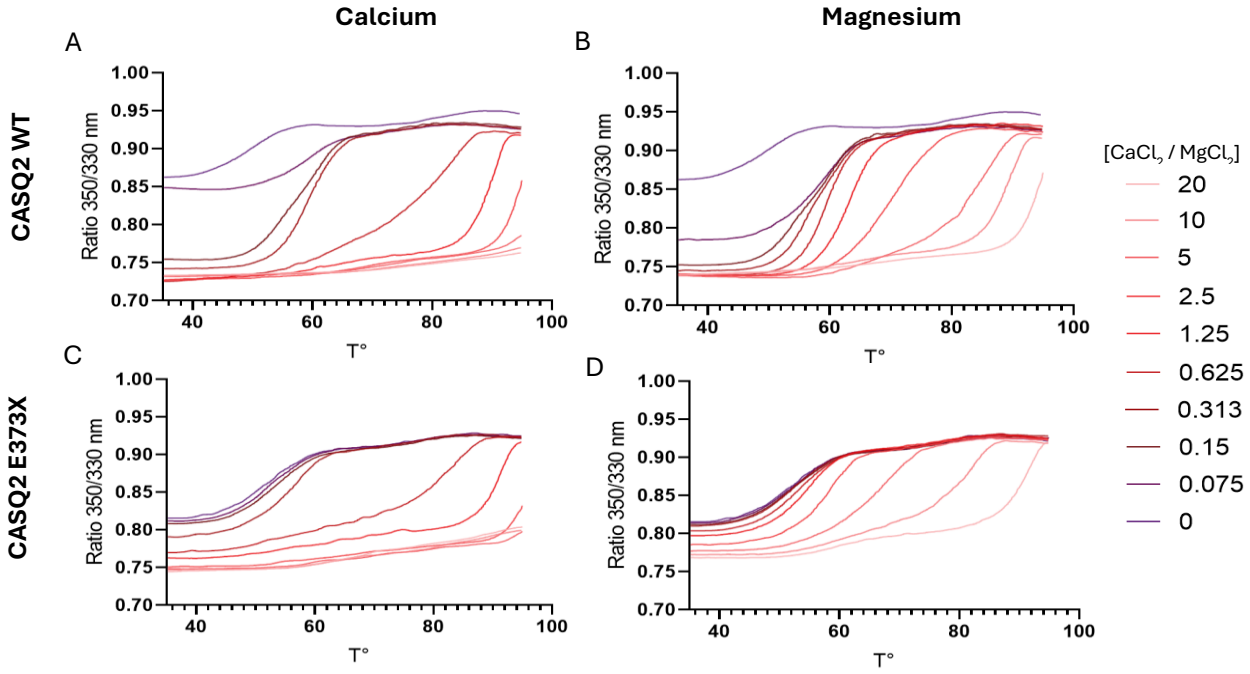

Figure 20. Concentration-dependent modulation of tryptophan microenvironment by Ca^{2+} and Mg^{2+} in wild-type CASQ2 and CASQ2-E373X. Intrinsic tryptophan fluorescence thermal stability assays of wild-type CASQ2 and E373X mutant in the presence of increasing concentrations of $CaCl_2$ (left column) or $MgCl_2$ (right column) from 0 to 20 mM. In wild-type CASQ2 (top row) both Ca^{2+} and Mg^{2+} produce progressive concentration-dependent decreases in the basal fluorescence ratio at 35°C, indicating progressive compaction of the tryptophan microenvironment with increasing divalent cation concentration. Ca^{2+} effects are detectable at 0.075–0.15 mM and Mg^{2+} at comparable concentrations, though Ca^{2+} produces larger shifts at equivalent concentrations throughout the range. At higher concentrations both ions also produce a concentration-dependent increase in thermal stability, reflected as a rightward shift of the unfolding transition, with Ca^{2+} again showing a more pronounced stabilizing effect than Mg^{2+}. In CASQ2-E373X, the concentration-response for both ions is markedly attenuated (bottom row). The basal fluorescence ratio and unfolding transition are largely insensitive to divalent cation addition below approximately 1.25–2.5 mM Ca^{2+} and 2.5–5 mM Mg^{2+}, demonstrating that tail deletion substantially shifts the ion concentration threshold required to produce detectable conformational changes. The attenuation is more pronounced for Mg^{2+} than Ca^{2+}, with E373X retaining a partial Ca^{2+} response at intermediate concentrations while remaining almost entirely unresponsive to Mg^{2+} below 5 mM, confirming that the C-terminal tail contributes disproportionately to Mg^{2+} sensitivity relative to Ca^{2+} sensitivity.

In wild-type CASQ2, a stabilization response is detectable at remarkably low divalent cation concentrations: both Ca^{2+} (Figure 20A) and Mg^{2+} (Figure 20B) produce measurable fluorescence ratio changes already at 0.075–0.15 mM. Within this range, Mg^{2+} consistently produces a larger fluorescence ratio decrease at 0.075 mM than Ca^{2+}, demostrating a clear potency difference between the two ions in modulating the third-domain tryptophan environment in presence of the C-terminal tail. This effect may thus be a consequence of the C-terminus Mg^{2+}-buffering capacity that, especially at low divalent concentrations, has major effects on the globular core Mg^{2+}-binding stability.

In E373X, the concentration-response for both ions is markedly altered. The initial fluorescence ratio remains essentially unchanged relative to the ion-free condition up to substantially higher divalent cation concentrations, approximately 0.15mM Ca^{2+} and 0.3 mM Mg^{2+}, indicating that the C-terminal tail deletion hampers divalent-dependent conformational changes of the third thioredoxin domain. The melting curve progresses towards higher t_m more linearly with increasing concentrations of Mg^{2+}, whereas increasing Ca^{2+} from 0.3 to 0.6 mM produces a large rightward shift. Compared to the wild-type behaviour, the E373X protein E373X retains a partial Ca^{2+} response at intermediate concentrations, with higher Ca^{2+} concentrations stabilizing the hydrophobic environment of the third domain core almost as they do for the wild-type protein. This reflects the ability of the globular core alone to bind Ca^{2+} through its own acidic residues. At the same time, the responsiveness of E373X to physiological amounts of Mg^{2+} (below 2.5 mM) is hampered, and the decrease in 350/330 nm fluorescence emission ratio, symptomatic of core stabilization, is not as strong as for the wild-type. The asymmetry between the responses of E373X to physiological quantities of Ca^{2+} and Mg^{2+} is in line with the findings from turbidimetric analysis in section 4.1 and MD analyses in this section. The C-terminal tail contributes disproportionately more to Mg^{2+} than to Ca^{2+} sensitivity, because Mg^{2+} coordination at the proximal portion of the tail promotes multimerization (supporting a strong shift in the t_m at a threshold concentration), and buffers its recruitment by the structured globular domain (hence an amplified sensitivity to Mg^{2+} of the third thioredoxin domain of the full-length construct). An additional role of the C-terminal tail regards the increased stabilization of the globular core by both Ca^{2+} and Mg^{2+}: in absence of this flexible IDR, the third thioredoxin domain is more stable in absence of divalents, yet it becomes unsensitive to the strong stabilization shift promoted by both Ca^{2+} and Mg^{2+} via conformational rearrangement of the C-terminal tail, which packs against the protein core. Overall, the tail is mechanistically more implied as a Mg^{2+}-sensing element at physiological Mg^{2+} concentrations. Ca^{2+}, which inner-sphere coordination occurs equally at the core and at the less organized tail, retains a partial globular-core-mediated route to tryptophan environment modulation in the absence of the tail.

These observations establish a coherent model for how the C-terminal tail amplifies and directs the conformational consequences of divalent cation binding across the entire CASQ2 dimer. The tail acts as an electrostatic amplifier: its high negative charge density in the ion-free state exerts a tonic repulsive force on the third domain surface, maintaining it in a more open and dynamically accessible conformation than would be adopted in the tail's absence. Divalent cation binding to the tail progressively neutralizes this repulsion, allowing the tail to approach the globular core and relieving the electrostatic pressure on the third domain, a signal that propagates across the dimer as a global reduction in solvent exposure and conformational flexibility. The tail therefore translates changes in ionic composition into a graded mechanical signal that reshapes the conformational landscape of the entire globular structure.

4.5 Potassium, calcium, and magnesium shape the distinct conformational profile of the C-terminal tail.

Having validated that Ca^{2+} and Mg^{2+} produce distinct effects on the C-terminal tail backbone flexibility, spatial positioning, and third-domain conformational openness, we sought to characterize the full thermodynamic and kinetic consequences of these ionic differences at the level of the complete conformational space accessible to the tail. To achieve this, free energy landscapes (FELs) were constructed from principal component analysis (PCA) of the MD simulation trajectories obtained under K^+, Ca^{2+}, and Mg^{2+} conditions. The PCA was performed on the concatenated trajectories of both C-terminal tails of the homodimer, treating the two chains as statistically equivalent samples of the same conformational ensemble, a valid approximation given the symmetry of the homodimer and the equivalence of the two tail sequences. The resulting landscapes were normalized to a shared global energy reference defined as the lowest free energy minimum observed across all three conditions, which corresponds to the Mg^{2+} simulation (F_min = 0.00 kJ/mol). The global minima for Ca^{2+} and K^+ lie at 1.76 kJ/mol and 2.87 kJ/mol above this reference respectively, enabling direct quantitative thermodynamic comparison of the dominant conformational states across the three ionic conditions.

4.5.1 The K^+ landscape: passive thermal exploration

In the presence of K^+ alone (Figure 21A), the FEL of the C-terminal tail is broad, flat, and fragmented into three spatially separated low-energy basins distributed across a wide range of both PC1 and PC2 values, with no single basin clearly dominating the landscape. The basins are shallow and separated

by low energetic barriers, indicating easy interconversion between states and extensive conformational heterogeneity. Structural inspection of the representative conformation at the primary K^+ basin minimum (Figure 21B) reveals that, even in the complete absence of divalent ions, the C-terminal tail does not remain fully extended in solution. Rather, the distal portion of the tail, from Asp395 to Glu399, establishes electrostatic contacts with positively charged residues located on the first and second thioredoxin domains of the opposing monomer (Lys47, Lys43 on domain I; Lys172, Lys210, Lys206, Lys201 on domain II), generating a partially closed dimeric architecture in which the terminal segment is electrostatically anchored to the opposite monomer surface. The central portion of the tail, by contrast, does not establish equivalent contacts and remains at greater average distance from the protein surface, leaving the tail in a partially engaged rather than fully collapsed state.

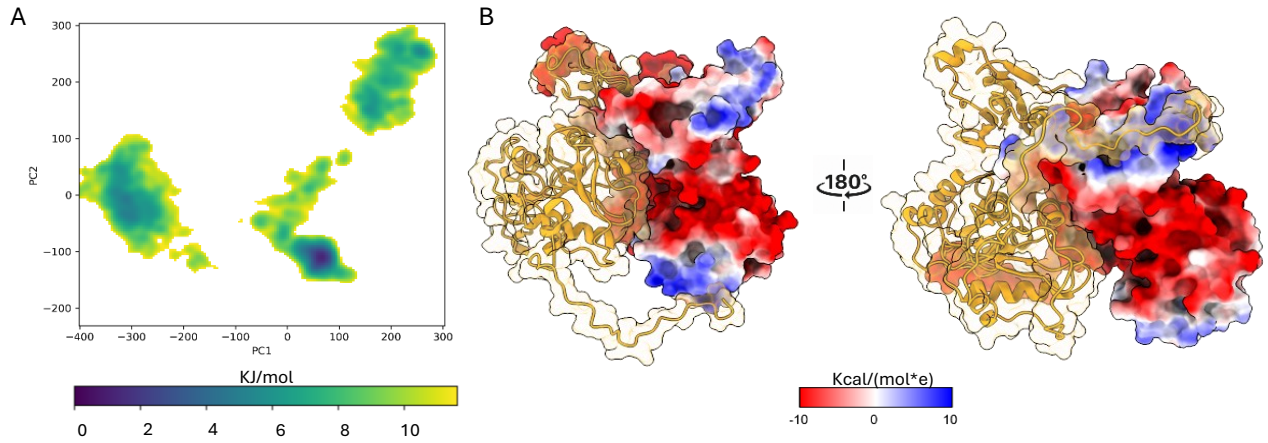

Figure 21. Free energy landscape and representative conformational state of the CASQ2 C-terminal tail under K^+-only conditions. (A) Free energy landscape (FEL) of the CASQ2 C-terminal tail under K^+-only conditions, built from principal component analysis (PCA) of the concatenated MD trajectories of both C-terminal tails of the homodimer. The landscape is projected onto the first two principal components (PC1, PC2) and coloured by free energy (kJ/mol). The FEL displays at least three spatially separated low-energy basins distributed across a wide range of PC1 and PC2 values, with no single basin clearly dominating. The shallow basins and low interconversion barriers indicate extensive conformational heterogeneity and facile exchange between states, consistent with passive thermally driven exploration of conformational space in the absence of divalent ion coordination. (B) Representative structure at the primary K^+ FEL minimum, shown from two opposing views (180° rotation). The CASQ2 homodimer globular core is shown as a gold ribbon, with one monomer's C-terminal tail displayed as a surface coloured by electrostatic potential. The representative conformation reveals that even in the absence of divalent ions the C-terminal tail does not remain fully extended but establishes partial contact with the globular surface of the opposing monomer through electrostatic attraction between the negatively charged distal tail terminus and positively charged surface patches on the first and second thioredoxin domains. The central portion of the tail remains at greater distance from the globular surface, producing a partially engaged rather than fully collapsed conformation driven purely by monovalent ion-screened electrostatics.

This configuration reflects a thermodynamic attractor driven purely by electrostatic attraction between the highly negative tail terminus and the positively charged surface patches of the globular domain, accessible without any divalent ion coordination. The broad and fragmented K^+ FEL reflects

the fact that the tail can reach this partially engaged state through multiple distinct trajectories and orientations, none of which is sufficiently stabilized by monovalent screening alone to dominate the ensemble, and that it continues to exchange freely between these configurations on the nanoseconds timescale of the simulation.

4.5.2 The Ca^{2+} landscape: directed compaction onto the lateral surface.

In the presence of Ca^{2+} the conformational landscape (Figure 22A), is substantially reorganized relative to K^+. A dominant low-energy basin centred near PC1 ≈ +30 and PC2 ≈ −87 constitutes the primary free energy minimum under this condition, with a second higher-energy basin visible in the upper region of the landscape separated by approximately 3–4 kJ/mol. The primary Ca^{2+} basin shows internal complexity, multiple closely spaced sub-minima rather than a single sharp energy well, indicating that the dominant Ca^{2+}-stabilized state encompasses a family of closely related but not identical tail configurations rather than a single rigid geometry. Structural inspection of the representative conformation at the Ca^{2+} primary minimum (Figure 22B) reveals a qualitatively distinct tail arrangement compared to K^+. Rather than only the distal terminus engaging the globular surface, the entire C-terminal tail sequence collapses onto the lateral surface of the dimeric structure. This conformation is stabilized by the carboxylate groups of the tail contacting either directly the positively charged regions on the opposing monomer (Lys201, Lys205, Lys118, Lys87, Lys31) and indirectly through Ca^{2+} coordination bridges. The result is a conformation in which the DEX^n-motif is fully drawn against the dimer surface. The internal complexity of the Ca^{2+} primary basin with its multiple sub-minima, is mechanistically interpretable in terms of Ca^{2+} coordination dynamics. Ca^{2+} drives global compaction of the tail against the lateral surface through its capacity for rapid inner-sphere coordination and inter-residue crosslinking, but its high surface mobility and fast coordination exchange imply that the specific residue-level contacts established at any given moment are continuously reshuffled. The tail is therefore maintained in a surface-attached state by an ensemble of transient coordination bridges rather than by a fixed set of stable contacts, generating the family of closely related surface-attached configurations that populate the primary basin. In this picture, Ca^{2+} functions as a conformational driver where multivalent routes converge to an equivalent result: the same lateral surface interactions that K^+ can only passively and transiently support through thermal fluctuations, become the dominant, reliably occupied state because of Ca^{2+}-mediated crosslinking, regardless of the tail's starting position.

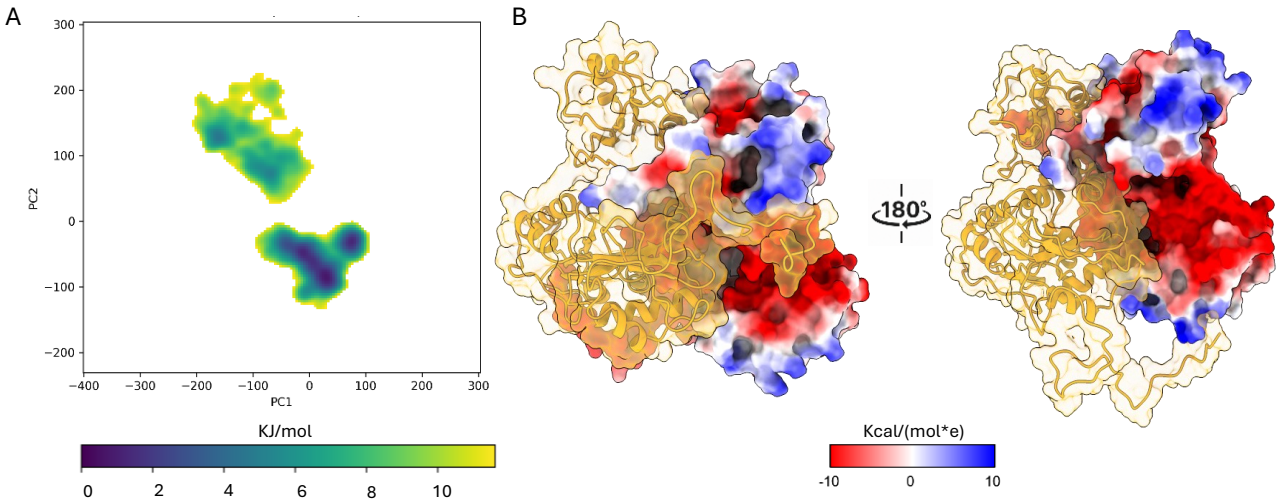

Figure 22. Free energy landscape and representative conformational state of the CASQ2 C-terminal tail under Ca^{2+} conditions. (A) Free energy landscape (FEL) of the CASQ2 C-terminal tail under Ca^{2+} conditions, produced from PCA of the concatenated MD trajectories of both C-terminal tails of the homodimer, projected onto PC1 and PC2 (kJ/mol, colour scale: dark purple = low energy, yellow = high energy). Relative to the K^+-only landscape (Figure 21A), the Ca^{2+} FEL is substantially different: a dominant low-energy basin centred near PC1 ≈ +30, PC2 ≈ −87 constitutes the primary free energy minimum, with a second higher-energy basin separated by approximately 3–4 kJ/mol. The primary basin shows internal complexity with multiple closely spaced sub-minima, reflecting a family of closely related but not identical tail conformations rather than a single rigid geometry. The simplification from the fragmented multi-basin K^+ landscape to a single dominant basin under Ca^{2+} reflects the active directional compaction of the tail toward a preferred surface-attached state driven by Ca^{2+} inner-sphere coordination and inter-residue crosslinking. (B) Representative structure at the Ca^{2+} primary FEL minimum, shown from two opposing views (180° rotation). The CASQ2 homodimer globular core is shown as a gold ribbon, with the C-terminal tail displayed as a surface coloured by electrostatic potential. The representative conformation reveals full-length collapse of the C-terminal tail onto the lateral surface of the dimeric structure, mediated by direct electrostatic contacts with positively charged regions on the opposing monomer and through Ca^{2+} coordination bridges between globular surface residues and tail carboxylate groups.

4.5.3 The Mg^{2+} landscape: history-dependent kinetic trapping.

The Mg^{2+} free energy landscape (Figure 23A) is both the most thermodynamically stable and the most morphologically distinctive of the three conditions. Its primary minimum near PC1 ≈ +123, PC2 ≈ +67 constitutes the global reference of the entire analysis, the deepest energy minimum across all conditions, and its basin is elongated, spanning a broad range of conformational space while remaining energetically connected as a single extended low-energy region. A second basin in the upper-left region at PC1 ≈ −200, PC2 ≈ +160 is separated from the primary minimum by approximately 6 kJ/mol. Structural inspection of the Mg^{2+} primary basin (Figure 23B) reveals an asymmetric configuration of the two C-terminal tails within the homodimer: one tail adopts a conformation closely resembling the Ca^{2+}-stabilized lateral surface attachment, while the other collapses onto the back surface of the globular domain, a region not contacted by the tail under either K^+ or Ca^{2+}. This structural asymmetry between the two nominally equivalent chains of the homodimer requires careful mechanistic consideration of how Mg^{2+} interacts with the tail.

Interestingly, the structural outcome is entirely dependent on the initial position of the tail at the moment Mg^{2+} coordination is established. When a tail is already near the lateral surface, the thermodynamic attractor identified under K^+, Mg^{2+} maintains the tail in that position, similarly to the Ca^{2+}-dependent lateral attachment. However, and differently from the effect of Ca^{2+}, when the tail's starting position is in a more distal or extended configuration, Mg^{2+} guides a slow compaction of the tail itself, which eventually falls into a local energy minimum on the back surface of the globular domain, a metastable trap accessible from its starting position but not from the lateral surface attachment. The back-surface conformation is therefore not a Mg^{2+}-directed structural state. Rather, it is a history-dependent outcome: a reflection of where the tail was, not of where Mg^{2+} wanted it to go. In this perspective, Mg^{2+} acts as a conformational brake, driving the C-terminal tail towards the closest conformational energy minimum.

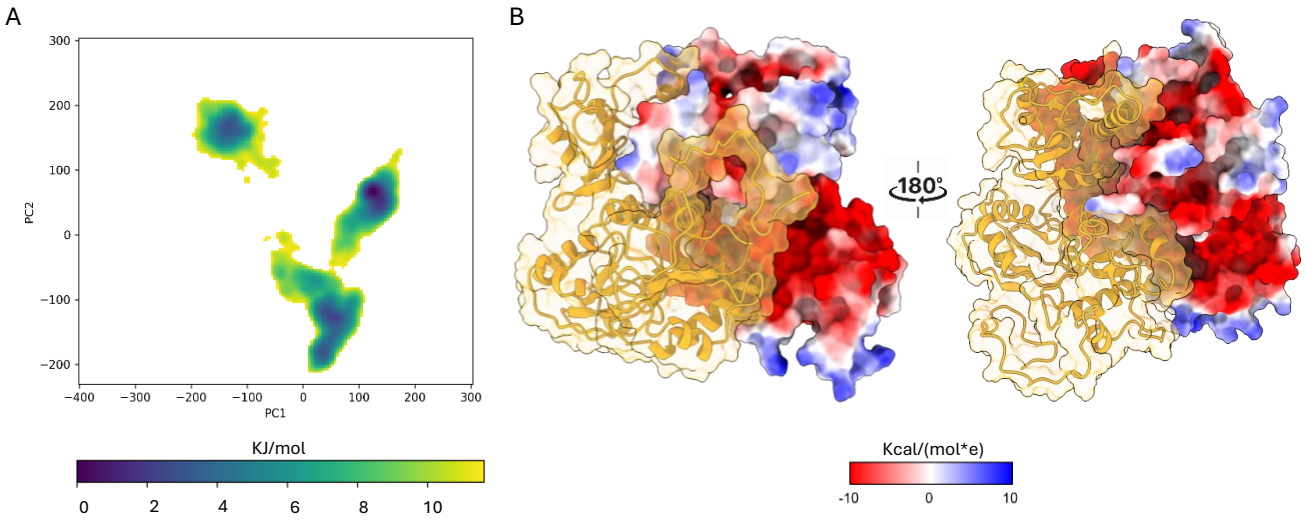

Figure 23. Free energy landscape and representative conformational state of the CASQ2 C-terminal tail under Mg^{2+} conditions. (A) Free energy landscape (FEL) of the CASQ2 C-terminal tail under Mg^{2+} conditions constructed from PCA of the concatenated MD trajectories of both C-terminal tails of the homodimer, projected onto PC1 and PC2 (kJ/mol). The Mg^{2+} FEL is morphologically distinct from both the K^+ (Figure 21A) and Ca^{2+} (Figure 22A) landscapes. The global free energy minimum of the entire analysis resides within this landscape, confirming that Mg^{2+} produces the thermodynamically most stable conformational state across all three ionic conditions. The landscape displays an elongated primary basin spanning a broad range of PC space, and two additional separated low-energy regions. (B) Representative structure at the Mg^{2+} primary FEL minimum, shown from two opposing views (180° rotation). The CASQ2 homodimer globular core is shown as a gold ribbon, with the C-terminal tail displayed as a surface coloured by electrostatic potential. The representative conformation reveals a striking structural asymmetry between the two C-terminal tails of the homodimer: one tail adopts a lateral surface attachment closely resembling the Ca^{2+}-stabilized conformation, while the other collapses onto the back surface of the globular domain, a region not contacted by the tail under either K^+ or Ca^{2+} conditions.

This interpretation explains both the elongated morphology of the Mg^{2+} FEL basin and the partial overlap with the Ca^{2+} landscape in the lower-right PC region. The elongated basin reflects the superposition of history-dependent, yet replicate-independent, trajectories of the tail, rather than a single ion-specific conformation being sampled repeatedly. The partial overlap with Ca^{2+} (Figure 24)

confirms that the lateral surface attachment is accessible in presence of either ion, but only Ca^{2+} drives the tail there reliably and regardless of the tail's starting position. Under Mg^{2+}, reaching the lateral surface attachment is contingent on the tail already being near it. This history-dependence precisely explains the molecular mechanism underlying the conformational memory and Mg^{2+} priming behaviours documented in the turbidimetric experiments in section 4.1: the tail encodes its recent ionic history in its conformational position, and Mg^{2+} preserves that position against entropic decay, acting as a molecular brake.

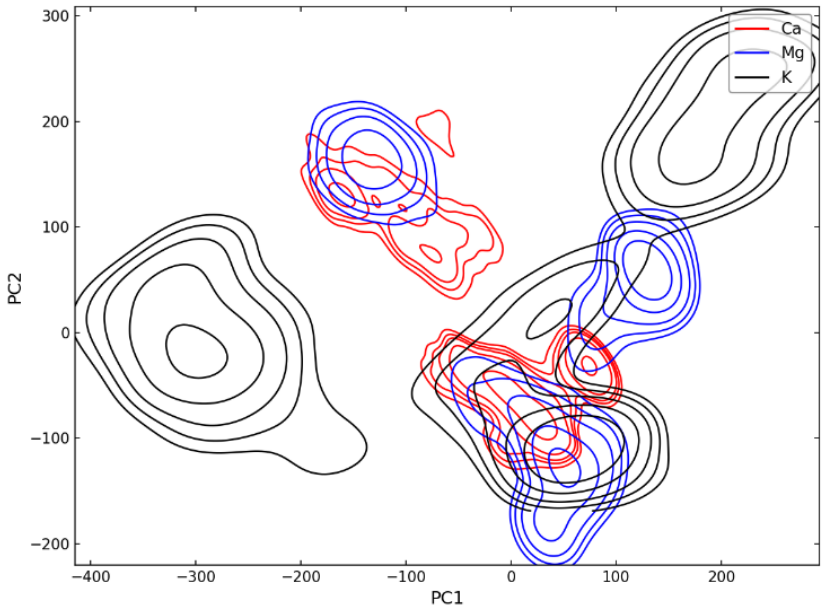

Figure 24. Overlay of conformational landscape contours for K^+, Ca^{2+}, and Mg^{2+} conditions confirm occupation of distinct and partially overlapping conformational spaces. Contour plot overlay of the conformational landscapes of the CASQ2 C-terminal tail under K^+ (black), Ca^{2+} (red), and Mg^{2+} (blue) conditions, projected onto the shared PC1–PC2 space defined by the combined PCA of all three trajectories. Each contour line represents an equal free energy interval, with inner contours corresponding to lower energy states. The three conditions occupy largely distinct regions of conformational space. The K^+ landscape (black) is the most expansive, with two well-separated low-energy basins spanning a wide PC1 range (approximately −400 to −200 and +50 to +200), reflecting the broad and heterogeneous conformational exploration characteristic of passive thermally driven sampling. The Ca^{2+} (red) and Mg^{2+} (blue) landscapes occupy a shared central region of PC space (approximately PC1 = −100 to +200, PC2 = +50 to +200), confirming that both divalent cations direct the tail toward a broadly similar spatial region, the lateral surface attachment. The partial overlap between Ca^{2+} and Mg^{2+} contours confirms that the lateral surface attachment conformation is accessible under both ions. The near-complete separation between the K^+ basins and the Ca^{2+}/Mg^{2+} region confirms that divalent cation coordination, regardless of ion type, produces a qualitatively distinct conformational regime relative to monovalent-only conditions.

4.5.4 Quantifying conformational memory: autocorrelation analysis

The FEL, and the fact that multiple and distinct initial positions of the tail converge to a unique conformational topology (in presence of Ca^{2+}) or may remained trapped also in an alternative energetic state (in presence of Mg^{2+}), raise the question on whether each ion may support one or more defined, intermediate, tail conformations in this process. To address this directly, we measured for

how long a given ensemble of tail conformations, more or less proximal to the globular core, is supported by the presence of Ca^{2+} or Mg^{2+}. More specifically, we computed the normalized autocorrelation function (ACF) of the centre-of-mass (COM) distance between each C-terminal tail and the globular core across three independent simulation replicates for each ionic condition. The integrated autocorrelation time (τ_int), the area under the ACF curve from lag zero to its first zero-crossing, was derived as a direct quantitative measure of the duration of positional memory of the tail (Figures 25A–B). A value of $C(\tau) = 1$ indicates perfect positional memory at lag τ, $C(\tau) = 0$ indicates complete loss of memory, and $C(\tau) < 0$ indicates that the tail has overshot to the opposite side of its mean position.

Under K^+ alone, the ACF decays to zero at a mean lag of approximately 130 ns, yielding τ_int = 34.9 ± 7.5 ns. Under Ca^{2+}, the ACF decays on a closely comparable timescale, with a mean zero-crossing at approximately 113 ns and τ_int = 32.0 ± 3.8 ns. The two values are statistically indistinguishable (not significantly different), confirming that, despite producing structurally distinct outcomes (a fragmented multi-basin landscape under K^+ versus a directed lateral surface attachment under Ca^{2+}), the two conditions support equivalent rates of conformational exchange. The ~30–35 ns conformational memory established under K^+ is therefore not enhanced by Ca^{2+} coordination: the faster and more mobile Ca^{2+} ion drives structural compaction without imparting kinetic persistence to the compacted state.

The Mg^{2+} ACF presents an entirely different picture. The decay is substantially slower across all three replicates, with a mean zero-crossing at approximately 265 ns, more than twice the lag at which either K^+ or Ca^{2+} reach zero, and τ_int = 94.8 ± 9.0 ns, approximately three times larger than either of the other two conditions (Figure 25B). This threefold difference is consistent and reproducible across all three independent replicates, confirming that the kinetic slowing under Mg^{2+} is a robust and replicable property of the system rather than a single-trajectory artefact. Importantly, the Mg^{2+} τ_int values are noted as conservative lower bounds: the ACF did not fully decay within the analysis window for all replicates, indicating that the true conformational memory under Mg^{2+} may extend beyond 94.8 ns, potentially to timescales not accessible within the simulation length. Mg^{2+} therefore slows down the tail conformational rearrangement by approximately threefold relative to either K^+ or Ca^{2+}, without changing the direction of the process but its kinetic only: the defining signature of a conformational brake mechanism.

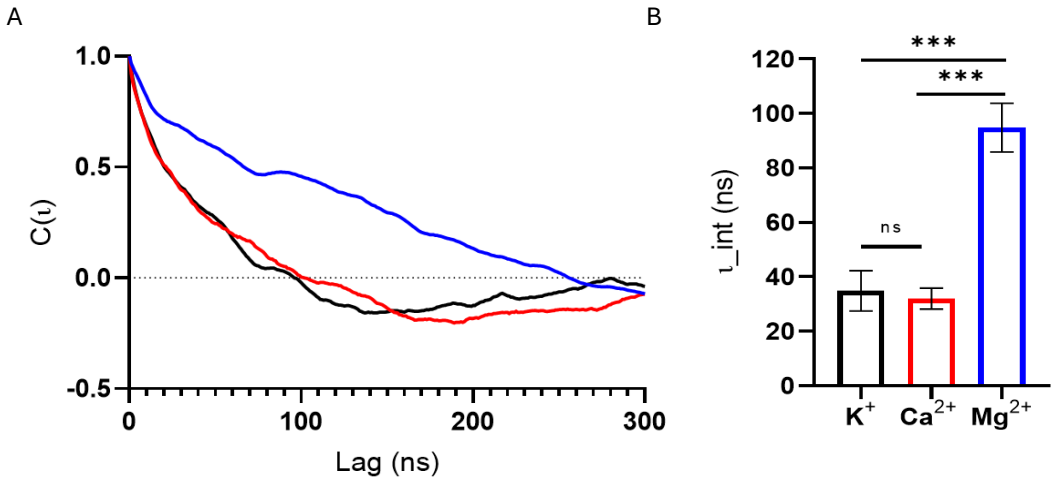

Figure 25. Autocorrelation analysis reveals Mg^{2+}-specific kinetic slowing of C-terminal tail conformational dynamics. (A) Normalized autocorrelation function (ACF, C(τ)) of the centre-of-mass (COM) distance between the C-terminal tail and the globular core, plotted as a function of lag time for K^+ (black), Ca^{2+} (red), and Mg^{2+} (blue) conditions. C(τ) = 1 indicates perfect positional memory, C(τ) = 0 indicates complete loss of memory, and C(τ) < 0 indicates overshoot beyond the mean position. The K^+ and Ca^{2+} ACFs decay to zero on comparable timescales, with mean zero-crossings at approximately 130 ns and 113 ns respectively. The Mg^{2+} ACF decays substantially more slowly, retaining positional memory beyond 265 ns lag, confirming that Mg^{2+} coordination imposes a marked kinetic slowing of tail conformational dynamics not observed for either K^+ or Ca^{2+}. Curves represent the mean across three independent replicates. (B) Integrated autocorrelation time (τ_int) for K^+, Ca^{2+}, and Mg^{2+} conditions, calculated as the area under the ACF from lag zero to its first zero-crossing. K^+ and Ca^{2+} yield statistically indistinguishable τ_int values of 34.9 ± 7.5 ns and 32.0 ± 3.8 ns respectively (ns, not significant). Mg^{2+} yields a τ_int of 94.8 ± 9.0 ns, approximately threefold larger than either K^+ or Ca^{2+} (*** $p < 0.001$ versus both conditions). This threefold difference is consistent across all three independent replicates and identify that Mg^{2+} specifically slows C-terminal tail conformational exchange without altering the structural destination of the tail, the defining quantitative signature of a conformational brake mechanism. Data are mean ± SD across three independent replicates. Significance assessed by unpaired two-tailed Student's t-test; *** $p < 0.001$.

The kinetic interpretation of Mg^{2+} action generates a directly testable experimental prediction: if the Mg^{2+} priming effect is fundamentally a kinetic phenomenon, the preservation of a metastable tail configuration against thermally driven conformational decay, then any physical intervention that reduces the thermal energy available to drive that decay should reproduce the same functional priming outcome, independently of any ion coordination. Reducing temperature is precisely such an intervention: it globally reduces the energy available for conformational exploration without altering the protein's chemical composition or ionic environment. To test this prediction, the Ca^{2+} responsiveness of wild-type and E373X CASQ2 preincubated at 4°C in the absence of Mg^{2+} was compared to the Mg^{2+}-preincubated (20°C) and buffer-only (20°C) conditions (Figure 26). Preincubation at 4°C preserved, in CASQ2 wild-type, the fast-responsive state precisely to the same degree as Mg^{2+} preincubation at 20°C: both conditions produced Ca^{2+} responses that were strikingly nearly identical in both initial rate and final turbidity amplitude. For the CASQ2 E373X mutant, the lower temperature seems to have the opposite effect: slowing down the Ca^{2+} response compared to the conditions in which the protein is allowed to equilibrate at 20°C. This suggests that, in absence of the C-terminal tail, the 4°C condition acts as a pure kinetic inhibitor of globular core calcium-induced

polymerization in E373X, whereas in wild-type it acts as a keeper of the most Ca^{2+}-responsive conformational state of the tail.

Low temperature and Mg^{2+} therefore apparently converge on precisely the same functional priming outcome through entirely independent physical mechanisms: cold temperature by globally reducing thermal fluctuations, Mg^{2+} by imposing specific kinetic trapping through long-lived coordination. This functional equivalence constitutes direct experimental support for the interpretation that the priming function of Mg^{2+} is an anti-entropic mechanism: it reduces the effective thermal exploration rate of the C-terminal tail, preserving conformational states that would otherwise decay through thermally driven exchange on the ~40-minute timescale defined in the equilibration experiments.

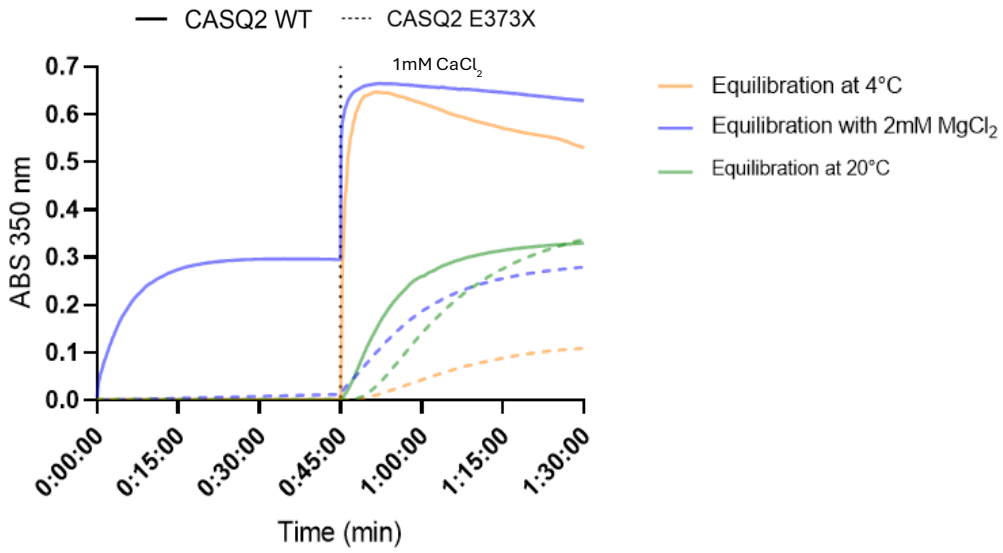

Figure 26. Cold temperature reproduces the Mg^{2+} priming effect in wild-type CASQ2 but inhibits Ca^{2+} responsiveness in CASQ2-E373X. Turbidimetric assays (absorbance at 350 nm) of wild-type CASQ2 (solid lines) and CASQ2-E373X (dashed lines) at 2.5 µM in 50 mM KCl, equilibrated for 45 minutes at 4°C (orange), with 2 mM $MgCl_2$ at 20°C (blue), or in buffer at 20°C (green), prior to addition of 1 mM $CaCl_2$ (dotted vertical line). Data are mean of three independent experiments. In wild-type CASQ2, 4°C preincubation and Mg^{2+} preincubation produce nearly identical Ca^{2+} responses, both substantially larger than the 20°C buffer condition, confirming that cold temperature and Mg^{2+} converge on the same priming outcome through distinct physical mechanisms and supporting the anti-entropic interpretation of Mg^{2+} action. In E373X, 4°C preincubation reduces rather than enhances the Ca^{2+} response relative to 20°C buffer, demonstrating that without the C-terminal tail temperature acts as a generic kinetic inhibitor of globular core polymerization, and confirming that the anti-entropic priming function depends absolutely on the presence of the C-terminal IDR.

A final and important mechanistic point concerns the intriguing, unique capacity of Mg^{2+} in this kinetic "slowing" effect versus Ca^{2+}. Both are divalent cations, both neutralize CASQ2 surface charges, and both are coordinated by the set of same acidic residues, with 93% overlap in contact sites. Yet Ca^{2+} does not increase τ_int beyond the K^+ baseline. The kinetic slowing is specific to Mg^{2+} and arises entirely from its longer coordination residence time, its inability to exchange rapidly

between sites due to the stability of its hydration shell, rather than from its divalent charge *per se*. This dissociation between structural outcome and dynamical timescale is the defining mechanistic signature of the Mg^{2+} effect on the C-terminal tail: Ca^{2+} funnels the tail conformational exploration towards a set of equivalent positions, with no effect on the kinetics of the process, whereas Mg^{2+} is a kinetic and thermodynamic player. Together, the two ions provide complementary and non-redundant control over the conformational landscape of the C-terminal IDR: Ca^{2+} as a conformational driver that sustain the productive assembly-competent state, and Mg^{2+} as a conformational brake that preserves the ionic memory that endows the CASQ2 C-terminal tail its remarkable kinetic function over CASQ2 Ca^{2+}-binding sensitivity and consequent polymerization .

4.6 The C-terminal tail translates the ionic environment signal in different molecular assemblies that retains different properties.

To provide direct structural and biophysical validation of the C-terminal tail-dependent and ionic history-dependent assembly states, two complementary experimental approaches were applied: cryo-electron microscopy imaging of the three CASQ2 variants under physiologically relevant divalent cation conditions, and thermal stability analysis comparing the protein systems generated under distinct ionic history conditions.

4.6.1 CryoEM oligomers qualitative analysis of CASQ2 wild-type C-terminal tail mutant's reveal differences in the assembly's morphology

CryoEM images were acquired from wild-type, E373X, and D383X CASQ2 samples incubated 40 minutes with 2 mM $MgCl_2$, followed by 1 mM $CaCl_2$ addition and vitrified at 2 mg/ml after 40 (Figure 27). The three proteins present qualitatively distinct morphologies under these conditions. Wild-type CASQ2 shows the richest and most structured particle population: multiple oligomeric species are visible, including small compact particles and larger branched assemblies, consistent with a heterogeneous ensemble of dimers, higher-order oligomers, and early polymeric nuclei coexisting in solution. The presence of branched structures is particularly notable as it is consistent with the nodal network polymer architecture described for CASQ in situ[16] and suggests that under Mg^{2+} priming followed by Ca^{2+} addition, wild-type CASQ2 initiates productive, structured polymerization. No large aggregates are detected at inspected magnifications, indicating that this assembly remains soluble and structurally organized rather than collapsing into amorphous precipitates.

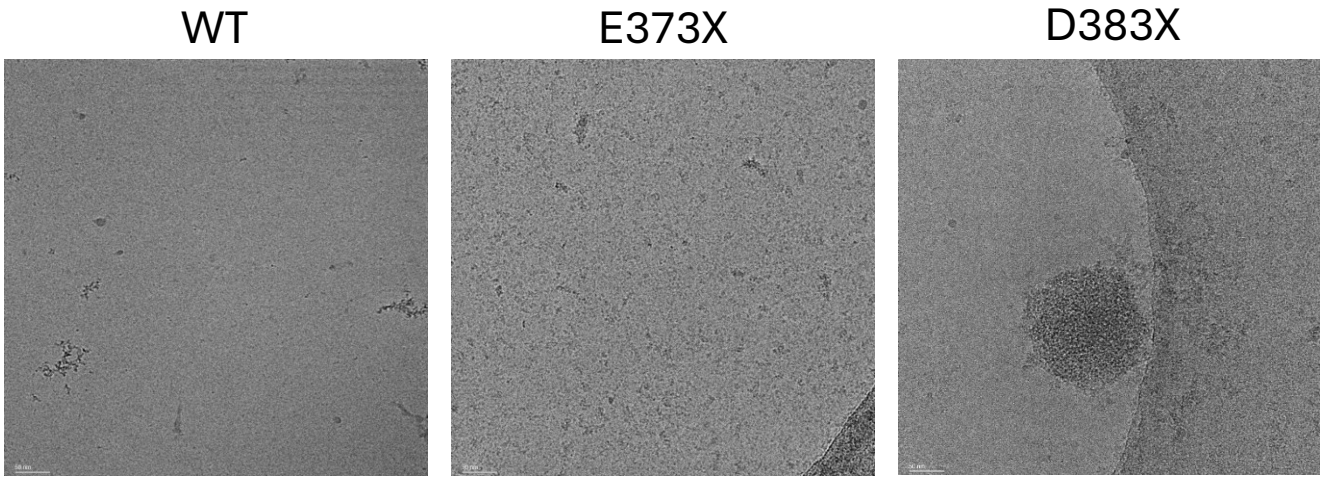

Figure 27. CryoEM imaging of CASQ2 WT, E373X, and D383X under Mg^{2+} preincubation and Ca^{2+} addition conditions reveal distinct assembly morphologies. Representative cryoEM micrographs of wild-type CASQ2, CASQ2-E373X, and CASQ2-D383X at 2 mg/mL prepared in the presence of 2 mM $MgCl_2$ for 40 minutes followed by addition of 1 mM $CaCl_2$. Wild-type CASQ2 (left panel) shows a heterogeneous population of small compact particles and larger branched assemblies distributed across the vitrified field, consistent with a coexisting ensemble of oligomers and early structured polymeric nuclei. E373X (central panel) shows a markedly reduced particle density with fewer and smaller non-branched particles relative to wild-type, consistent with its attenuated Ca^{2+}-driven assembly, though occasional large spherical dense bodies indicative of non-specific aggregation is also detected. D383X (right panel) is dominated by a large, dense irregular aggregate substantially exceeding in size any assembly observed in the wild-type or E373X fields, representing the structural correlate of the exaggerated unregulated Mg^{2+}-driven assembly documented turbidimetrically.

E373X presents a markedly impoverished particle population relative to wild-type: fewer particles are visible, they are smaller and non-branched, and the overall particle density across the field is lower. However, large spherical dense bodies are also detected in some areas of the grid, suggesting that in the absence of the entire C-terminal tail a significant fraction of the protein undergoes non-specific aggregation rather than linear assembly into the branched oligomers seen for the wild-type.

The D383X mutant also presents a dysregulated assembly morphology compared to wildtype. Large, dense, and irregular protein phases are clearly visible in the cryoEM field. This massive aggregate may represent the structural correlate of the unregulated Mg^{2+}-driven assembly observed turbidimetrically for D383X (Figure 11A, section 4.1) and further supports that the proximal Mg^{2+}-sensing segment (residues 373–382), when present without the distal regulatory governor (residues 383–399), drives aberrant large-scale aggregation rather than productive structured polymerization under conditions where both Mg^{2+} and Ca^{2+} are present.

The comparison between E373X and D383X is particularly informative: E373X, lacking the entire tail including the proximal Mg^{2+} sensor, forms smaller non-productive assemblies; D383X, retaining the proximal sensor without the distal governor, forms substantially larger aggregates. This hierarchy directly demonstrates that the proximal segment is the active driver of the aberrant assembly

observed, and that the distal segment is required to constrain and direct productive Ca^{2+}-responsive polymerization rather than uncontrolled aggregation.

4.6.2 The ionic history defines the assembly state of CASQ2

Three ionic history conditions produce equivalent Ca^{2+} responses in turbidimetric assays: i) 0 minutes equilibration, ii) 40-minute equilibration at 4°C, and iii) 40-minute Mg^{2+} incubation. To test whether these also generate equivalent assembled protein systems, Tycho thermal stability analysis was performed on wild-type CASQ2 samples prepared under each condition and analysed immediately after Ca^{2+} addition (Figure 28).

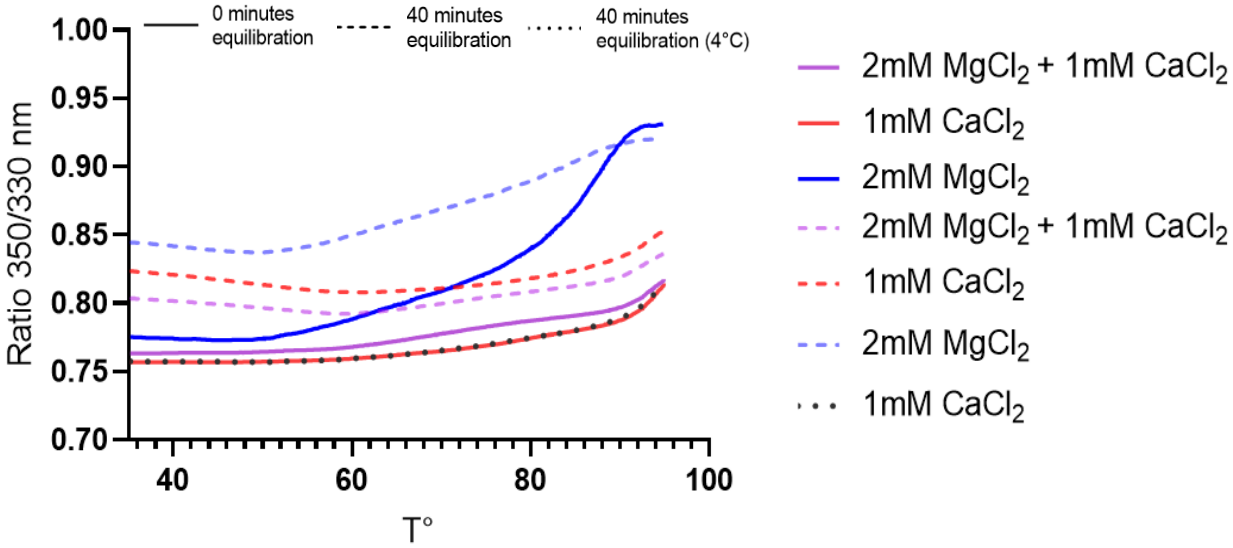

Figure 28. Thermal stability analysis reveals ionic history-dependent assembly states of CASQ2. Tycho intrinsic tryptophan fluorescence thermal stability assay of wild-type CASQ2 at 2.5 µM under nine ionic history conditions combining equilibration time (0 minutes solid, 40 minutes dashed, 40 minutes at 4°C dotted) and ionic composition (2 mM $MgCl_2$ + 1 mM $CaCl_2$ magenta, 1 mM $CaCl_2$ red, 2 mM $MgCl_2$ blue). Fluorescence ratio 350/330 nm is plotted as a function of temperature from 35°C to 100°C. The three conditions producing equivalent Ca^{2+} turbidimetric responses: 0' equilibration + 1mM $CaCl_2$ (solid red), 4°C equilibration + 1mM $CaCl_2$ (dotted black), and 2mM $MgCl_2$ preincubation + 1mM $CaCl_2$ (solid magenta), produce nearly superimposable profiles, confirming that these conditions generate equivalent assembled protein systems. The 40-minute 20°C buffer equilibration + 1mM $CaCl_2$ (dashed red) produces a distinct lower-stability profile. $MgCl_2$-only conditions (solid and dashed blue) generate distinct profiles depending on when $MgCl_2$ is added relative to the conformational relaxation window.

The three conditions produced nearly superimposable fluorescence ratio profiles across the entire temperature range. The near-identical basal fluorescence ratios at 35°C and the overlapping unfolding profiles across all three conditions confirm that the protein systems generated under these three interventions are not only functionally equivalent in terms of Ca^{2+} responsiveness, as established by turbidimetry, but also structurally equivalent as assessed by thermal stability. This convergence across three physically distinct interventions provides strong evidence that the conformational

memory mechanism is relevant at the level of the assembled protein system rather than merely modulating a transient kinetic response.

In contrast, the 40-minute buffer equilibration at 20°C followed by Ca^{2+} addition (dashed red profile in Figure 28) produces a distinct profile with a higher basal fluorescence ratio, confirming that this condition generates a less packed conformation of the third thioredoxin domain, mirroring the less Ca^{2+}-responsive state documented in section 4.1.

The Mg^{2+}-only conditions bring an additional layer of information. Mg^{2+} preincubation alone without subsequent Ca^{2+} addition (solid blue, Figure 28) produces the highest basal fluorescence ratio and the most pronounced unfolding transition observable among all conditions, reflecting the distinct protein system generated by Mg^{2+}-driven assembly in the absence of Ca^{2+}. After 40 minutes of Mg^{2+} equilibration (dashed blue, Figure 28), the profile shifts to higher fluorescence ratios. The fact that Ca^{2+}-only 40-minute equilibration (dashed red, Figure 28) does not recapitulate the profile of the protein exposed to Ca2+ after a 40-minutes Mg^{2+} preincubation following an identical interval in buffer indicates that Mg^{2+} coordination, even when added to a protein that has already undergone conformational relaxation, generates a different assembled system than buffer equilibration alone. The two conditions in which Mg^{2+} is added at different timepoints after dilution therefore produce detectably different protein systems, consistent with the conformational history of the protein at the moment of Mg^{2+} addition determining the nature of the resulting assembly.

Conclusions

CASQ, the most abundant Ca^{2+}-handling protein in the jSR, and critical regulator of ECC in muscles, has traditionally been studied for its Ca^{2+}-related properties only. Recent results published by our laboratory[22] demonstrate that CASQ2 Ca^{2+}-binding and multimerization are strongly sensitive to the ionic environment, with strong implications for the possibility to dissect the distinct molecular effects of pathological recessive and dominant missense mutations. Additional insights from either published and in-house produced data suggest that the key determinant of CASQ2 multi-ionic sensitivity is the C-terminal IDR. This thesis investigated how the intrinsically disordered C-terminal tail of CASQ2 responds to the multi-ionic environment of the junctional sarcoplasmic reticulum (jSR), combining *in vitro* and *in silico* approach. Taken together, the results converge on a single overarching conclusion: the C-terminal tail is not a passive polyanionic scaffold appended to the globular core, but the molecular substrate through which CASQ2 encodes and preserves information about its ionic environment, a form of ionic detector that determines how the protein assembles in response to Ca^{2+}.

The starting experimental observation is that wild-type CASQ2, freshly diluted from a concentrated stock, polymerizes rapidly and extensively in response to Ca^{2+}, but progressively loses this rapid responsiveness when allowed to equilibrate in buffer for tens of minutes before Ca^{2+} addition. This time-dependent relaxation toward a less responsive state is abolished when the C-terminal tail is truncated. Dynamic light scattering confirms that this effect does not rely upon any time-dependent, detectable change in the oligomeric size distribution that nucleates Ca^{2+}-dependent polymerization. The loss of responsiveness is therefore not a redistribution between oligomeric species, but a conformational relaxation taking place within a stable ensemble, and one that is encoded specifically in the C-terminal tail.

A particularly informative result is that, while Ca^{2+} and Mg^{2+} produce identical turbidity responses, these identify with profoundly different responsiveness states with respect to a subsequent Ca^{2+} challenge. Preincubation with Mg^{2+}, which induces a fast Ca^{2+}-responsiveness state, is not an effect that relies simply on the formation of pre-assembled polymers. Rather, the effect of Mg^{2+} on CASQ2 is actually that of preserving the protein from the entropically-dependent relaxation into the low-responsive state, thus preserving the fast, high-amplitude Ca^{2+} response. Mg^{2+} can preserve the responsive state but cannot restore it once relaxation has occurred, and this effect is entirely dependent on the essential presence of the C-terminal tail. Two ionic conditions that appear equivalent at the

level of bulk assembly (presence of millimolar quantities of Ca^{2+} or Mg^{2+}) thus carry different pieces of information forward in time, and these are written in the tail.

This intriguing capacity of such a simple, poly-carboxylate sequence at the C-terminus of CASQ2, in distinguishing between divalent cations, which physiologically relevant concentrations' ratio cycles between systole and diastole, we exploited molecular dynamics approaches. Our simulations demonstrated that both Ca^{2+} and Mg^{2+} are coordinated by the same distributed network of aspartate and glutamate carboxylates, with extensively overlapping contact sites, confirming that CASQ2 does not possess ion-selective binding pockets and behaves as a polyelectrolyte rather than a classical metalloprotein. At the same time, the two ions interact with the tail in fundamentally different ways (Figure 29A). Ca^{2+} coordinates directly with CASQ2 residues through inner-sphere contacts, neutralises charge more efficiently than Mg^{2+} and acts as a conformational driver, actively directing the tail toward a defined docking sites on the globular surface of the protein dimer. Mg^{2+}, which retains its tightly bound octahedral hydration shell and coordinates predominantly through outer-sphere interactions at the flexible tail, is less efficacious in neutralizing CASQ2 solvent-exposed charges but forms markedly longer-lived contacts with the protein surface carboxylates. Rather than directing the tail to a particular position, Mg^{2+} slows its entropic motion: the time required for the tail to escape the starting conformational positioning under Mg^{2+} is roughly threefold longer than that required under either K^+ or Ca^{2+} (with no comparable slowing produced by Ca^{2+} with respect to K^+). The effect of Mg^{2+} is therefore best described as vibrational and kinetic, rather than conformational/structural: it slows and traps the conformational exploration of the tail, independently of the starting position, rather than funnel the conformational exploration of the tail toward a defined minimum. This interpretation was confirmed experimentally by the observation that a simple preincubation of the protein at a lower experimental temperature reproduces the Mg^{2+}-primed state in wild-type CASQ2, exactly as it would be expected if Mg^{2+} would act by restraining thermally driven conformational decay (Figure 29B).

The experimental probes were consistent with this picture. ζ-potential measurements confirmed that Ca^{2+} neutralises the CASQ2 surface charge more efficiently than Mg^{2+}, validating the simulation prediction in which Mg^{2+} sits more stably at a limited number of surface epitopes, impeding formation of a dense solvation layer as Ca^{2+} ions do establish over CASQ2 particles. Also, the tail-less E373X mutant is neutralised by Mg^{2+} faster than wild-type and D383X, indicating that the C-terminal tail itself retains Mg^{2+} in low-efficiency outer-sphere interactions that delay the net neutralisation of the protein surface; as suggested by molecular dynamics simulations, this occurs because Mg^{2+} ions are more prone to bind at the flexible C-terminus rather than at the geometrically more constrained

coordination sites on the structured core. In the absence of the tail, the same Mg^{2+} ions are instead free to neutralise the globular core directly.

The assembled polymeric systems generated by either: i) immediate Ca^{2+} addition, or ii) Ca2+ addition following Mg^{2+} preincubation, or iii) following cold equilibration, share an equivalent thermal denaturation profile, indicative of a similar conformational energy. Because the thermal denaturation pattern reports on how the protein unfolds in the context of oligomeric system, we interpret this convergence as evidence that these three conditions generate the same polymeric lattice. On the opposite, the polymer formed from the relaxed, buffer-equilibrated state is distinct. We propose that the Ca^{2+}-induced polymerization recruits CASQ2 building blocks whose C-terminal tails share a common conformational behaviour, so that ionic histories which preserve the same tail state yield lattices with the same underlying architecture, while a relaxed tail state produces a polymer of different character. Overall, the tail does not switch polymerization on or off: it rather shapes how the lattice is built, and CASQ2 is therefore able to assemble lattices with distinct features depending on the conformational state, and in particular the position of the C-terminal tail at the moment of assembly (Figure 29C).

Globally, our observations cohere into a single mechanistic model: K^{+} permits the tail to explore its conformational space freely allowing the tails to find its energetic minimum; Ca^{2+} drives the tail to a defined, assembly-competent position; and Mg^{2+}, without dictating a position of its own, slows and preserves whatever conformation the tail was occupying. The functional state of CASQ2 at any moment therefore reflects not only which ion is currently present, but the sequence of ionic conditions the protein has experienced. Because the distinct ionic histories produce assemblies with distinct biophysical signatures, the C-terminal tail effectively translates a temporal ionic sequence into a structurally and functionally distinct polymeric outcome. The tail may therefore be referred to as the molecular substrate of an ionic memory: it stores, in its dynamics and position rather than in any fixed fold, a record of the ionic environment that biases the protein's response to future Ca^{2+} signals. This model has direct implications for CASQ2 function in the cardiomyocyte. The jSR lumen is not a simple Ca^{2+} reservoir but a crowded, multi-ionic compartment in which CASQ2 reaches very high local concentrations and is bathed in a stable, non-cycling pool of 0.8-1 mM free Mg^{2+} alongside the Ca^{2+} that rises and falls between 0.3 mM and 1.5 mM with each contraction. The findings of this thesis suggest that this environment is not incidental but functionally necessary to keep CASQ2 in a state capable of responding rapidly to Ca^{2+}.

Comparative analysis of published turbidity assays, and parallel unpublished data from our lab, already suggests that the concentration at which CASQ2 is stored influence the responsiveness to

Ca^2. We hypothesise that in a crowded, highly concentrated environment, like the jSR, the C-terminal tails are held in a conformationally dynamic ensemble, kept away from their energetic minimum by the mutual electrostatic repulsion and steric exclusion of neighbouring molecules, and that it is precisely this out-of-minimum, dynamic state that is competent for a fast Ca^{2+} response. Upon dilution, this constraint is released and the tail is free to relax into its conformational minimum, which the molecular dynamics simulations identify as the distal portion of the tail docked onto the positively charged patches of the globular core. In this view, the loss of responsiveness over time is the physical signature of the tail falling into its energetic minimum, and the role of a persistent Mg^{2+} background is to keep the tail out of that minimum even once Ca^{2+} has been depleted. Maintaining CASQ2 in this fast-responsive state through the C-terminal tail may also be important for its dialogue with the other components of the calcium release unit: Qin et al. demonstrated that the presence of CASQ2 confers RyR2 the ability to distinguish between luminal Ca^{2+} and Mg^{2+} [43], placing CASQ2 as the CRU element able to translate and communicate the different ionic signals to which the jSR is repeatedly subjected. By identifying the C-terminal tail as the structural element that encodes this behaviour, this work also provides a framework for understanding how disruption of the tail, through truncation or through changes in its length and charge organisation rather than single residue substitutions, could compromise the controlled assembly of CASQ2 within the jSR, with potential consequences for the integrity of the calcium release unit and the fidelity of cardiac Ca^{2+} handling. More broadly, the recognition that an intrinsically disordered region can store regulatory information in the timescales of its motion, rather than in a defined structure, adds CASQ2 to the growing set of systems in which protein disorder serves not as an absence of biological function but as a substrate for complex non-linear functions, non-achievable by structured domains.

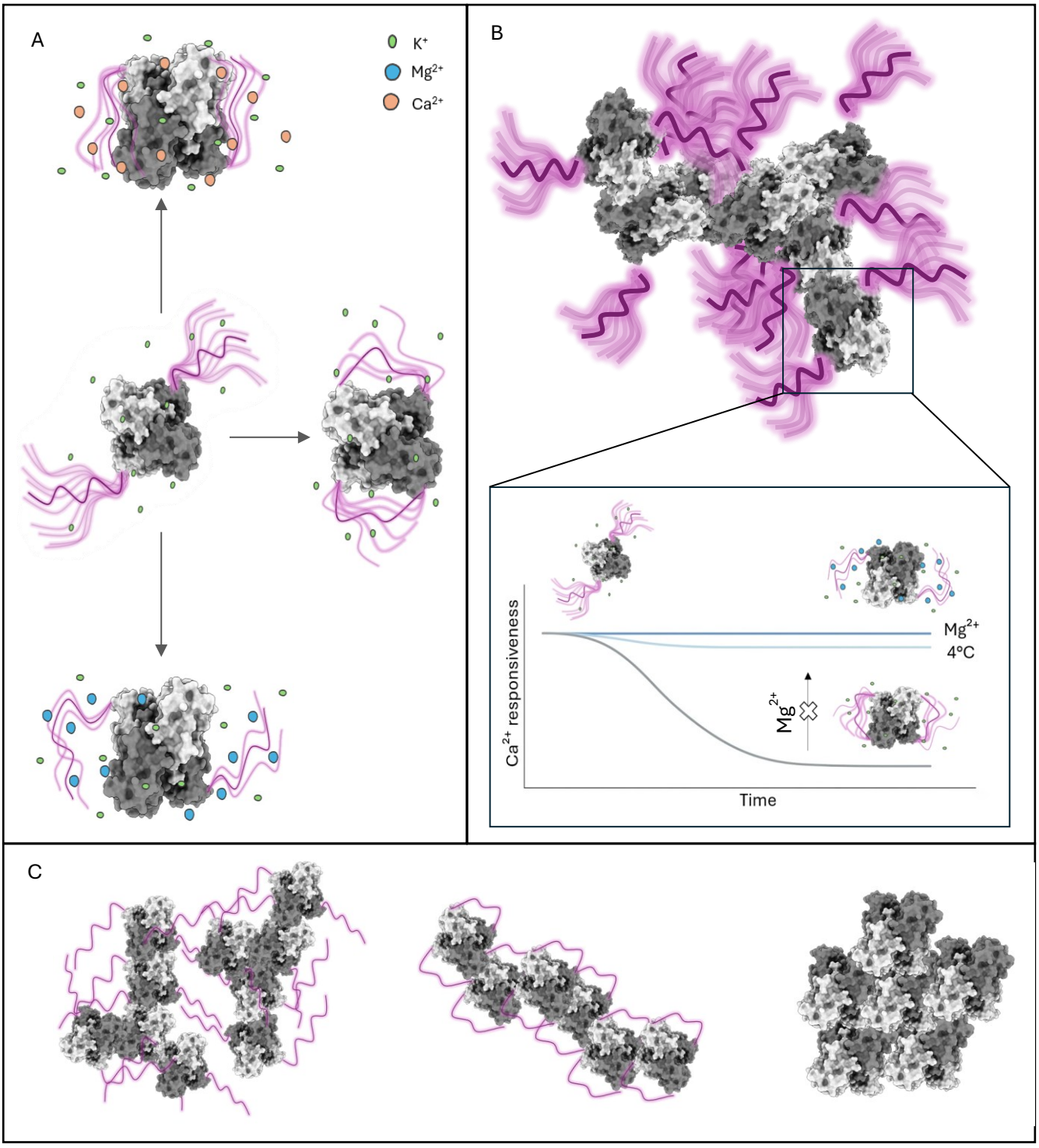

Figure 29. The C-terminal tail of CASQ2 as a substrate of ionic memory: a model.
(A) The three ionic regimes of the tail on the CASQ2 dimer. Under K^+ (centre) the tail freely explores conformational space before settling into its energy minimum along the lateral surface (lateral); Ca^{2+} (top) drives it onto this surface in a defined, assembly-competent yet dynamic state; Mg^{2+} (bottom) it slows its dynamics, kinetically trapping it. K^+ (green), Ca^{2+} (orange), Mg^{2+} (blue). (B) In solution CASQ2 oligomers hold their tails in a fast, Ca^{2+}-responsive dynamic state. Inset: upon dilution this responsiveness decays over time as the tail relaxes into its docked minimum (grey curve), unless preserved by persistent Mg^{2+} or low temperature (4 °C); once lost, it cannot be restored by Mg^{2+}, reflecting the directional, irreversible priming. (C) The conformation and dynamics of the tail at the moment of Ca^{2+}-driven assembly shape the lattice architecture, yielding different assemblies (left, centre). Without the tail (right), this regulation is lost and CASQ2 collapses into a disordered aggregate. All representations are schematic; the modelled tail position derives from Rosetta modelling and MD relaxation and the CASQ2 lattice architecture from cryo-EM images.

Bibliography

(1) Boncompagni, S.; Thomas, M.; Lopez, J. R.; Allen, P. D.; Yuan, Q.; Kranias, E. G.; Franzini-Armstrong, C.; Perez, C. F. Triadin/Junctin Double Null Mouse Reveals a Differential Role for Triadin and Junctin in Anchoring CASQ to the jSR and Regulating Ca2+ Homeostasis. *PLoS ONE* **2012**, *7* (7), e39962. https://doi.org/10.1371/journal.pone.0039962.

(2) Marabelli, C.; Santiago, D. J.; Priori, S. G. The Structural–Functional Crosstalk of the Calsequestrin System: Insights and Pathological Implications. *Biomolecules* **2023**, *13* (12), 1693. https://doi.org/10.3390/biom13121693.

(3) MacLennan, D. H.; Wong, P. T. S. Isolation of a Calcium-Sequestering Protein from Sarcoplasmic Reticulum. *Proc. Natl. Acad. Sci.* **1971**, *68* (6), 1231–1235. https://doi.org/10.1073/pnas.68.6.1231.

(4) Park, H.; Park, I. Y.; Kim, E.; Youn, B.; Fields, K.; Dunker, A. K.; Kang, C. Comparing Skeletal and Cardiac Calsequestrin Structures and Their Calcium Binding. *J. Biol. Chem.* **2004**, *279* (17), 18026–18033. https://doi.org/10.1074/jbc.M311553200.

(5) Wang, Q.; Michalak, M. Calsequestrin. Structure, Function, and Evolution. *Cell Calcium* **2020**. https://doi.org/10.1016/j.ceca.2020.102242.

(6) Bers, D. M. *Excitation-Contraction Coupling and Cardiac Contractile Force*, 2nd ed.; Developments in cardiovascular medicine; Kluwer Academic Publishers: Dordrecht ; Boston, 2001.

(7) Eisner, D. A.; Caldwell, J. L.; Kistamás, K.; Trafford, A. W. Calcium and Excitation-Contraction Coupling in the Heart. *Circ. Res.* **2017**. https://doi.org/10.1161/circresaha.117.310230.

(8) Knollmann, B. C. Casq2 Deletion Causes Sarcoplasmic Reticulum Volume Increase, Premature Ca2+ Release, and Catecholaminergic Polymorphic Ventricular Tachycardia. *J. Clin. Invest.* **2006**, JCI29128. https://doi.org/10.1172/JCI29128.

(9) Biral, D.; Volpe, P.; Damiani, E.; Margreth, A. Coexistence of Two Calsequestrin Isoforms in Rabbit Slow-twitch Skeletal Muscle Fibers. *FEBS Lett.* **1992**. https://doi.org/10.1016/0014-5793(92)80241-8.

(10) Sacchetto, R.; Volpe, P.; Damiani, E.; Margreth, A. Postnatal Development of Rabbit Fast-Twitch Skeletal Muscle: Accumulation, Isoform Transition and Fibre Distribution of Calsequestrin. *J. Muscle Res. Cell Motil.* **1993**, *14* (6), 646–653. https://doi.org/10.1007/BF00141561.

(11) Györke, I.; Hester, N.; Jones, L. R.; Györke, S. The Role of Calsequestrin, Triadin, and Junctin in Conferring Cardiac Ryanodine Receptor Responsiveness to Luminal Calcium. *Biophys. J.* **2004**. https://doi.org/10.1016/s0006-3495(04)74271-x.

(12) Handhle, A.; Ormonde, C. E.; Thomas, N. L.; Bralesford, C.; Williams, A. J.; Lai, F. A.; Zissimopoulos, S. Calsequestrin Interacts Directly with the Cardiac Ryanodine Receptor Luminal Domain. *J. Cell Sci.* **2016**, *129* (21), 3983–3988. https://doi.org/10.1242/jcs.191643.

(13) Franzini-Armstrong, C.; Kenney, L. J.; Varriano-Marston, E. The Structure of Calsequestrin in Triads of Vertebrate Skeletal Muscle: A Deep-Etch Study. *J. Cell Biol.* **1987**, *105* (1), 49–56. https://doi.org/10.1083/jcb.105.1.49.

(14) Johnson, E. A.; Sommer, J. R. A STRAND OF CARDIAC MUSCLE. *J. Cell Biol.* **1967**, *33* (1), 103–129. https://doi.org/10.1083/jcb.33.1.103.

(15) Manno, C.; Figueroa, L. C.; Gillespie, D.; Fitts, R.; Et., A. Calsequestrin Depolymerizes When Calcium Is Depleted in the Sarcoplasmic Reticulum of Working Muscle. *Proc. Natl. Acad. Sci.* **2017**. https://doi.org/10.1073/pnas.1620265114.

(16) Perni, S.; Close, M.; Franzini-Armstrong, C. Novel Details of Calsequestrin Gel Conformation in Situ. *J. Biol. Chem.* **2013**, *288* (43), 31358–31362. https://doi.org/10.1074/jbc.M113.507749.

(17) Titus, E. W.; Deiter, F. H.; Shi, C.; Wojciak, J.; Scheinman, M.; Jura, N.; Deo, R. C. The Structure of a Calsequestrin Filament Reveals Mechanisms of Familial Arrhythmia. *Nat. Struct. Mol. Biol.* **2020**, *27* (12), 1142–1151. https://doi.org/10.1038/s41594-020-0510-9.

(18) Lamb, G. Excitation–Contraction Coupling In Skeletal Muscle: Comparisons With Cardiac Muscle. *Clin. Exp. Pharmacol. Physiol.* **2000**. https://doi.org/10.1046/j.1440-1681.2000.03224.x.

(19) Marabelli, C.; Santiago, D. J.; Priori, S. G. The Yin and Yang of Heartbeats: Magnesium–Calcium Antagonism Is Essential for Cardiac Excitation–Contraction Coupling. *Cells* **2025**, *14* (16), 1280. https://doi.org/10.3390/cells14161280.

(20) Pani, P.; Aich, D.; Kar, B. P.; Giri, M. S.; Swalsingh, G.; Periasamy, M.; Bal, N. C. Isoform-Specific Structure and Function of Calsequestrin: Implications beyond Calcium Buffering in Health and Disease. *Cell Calcium* **2026**, *134*, 103120. https://doi.org/10.1016/j.ceca.2026.103120.

(21) Bal, N. C.; Jena, N.; Sopariwala, D.; Balaraju, T.; Et., A. Probing Cationic Selectivity of Cardiac Calsequestrin and Its CPVT Mutants. *Biochem. J.* **2011**. https://doi.org/10.1042/bj20101771.

(22) Marabelli, C.; Santiago, D. J.; Pirana, E.; Antonio, C. D.; Canciani, A.; Bolognesi, M.; Forneris, F.; Priori, S. G. Cardiac Calsequestrin Is a Physiological Dimer That Polymerizes through a Ca^{2+}-Triggered Cooperative Switch. bioRxiv April 7, 2026, p 2026.04.04.716468. https://doi.org/10.64898/2026.04.04.716468.

(23) Park, H.; Wu, S.; Dunker, A. K.; Kang, C. Polymerization of Calsequestrin. *J. Biol. Chem.* **2003**, *278* (18), 16176–16182. https://doi.org/10.1074/jbc.M300120200.

(24) Bal, N. C.; Sharon, A.; Gupta, S. C.; Jena, N.; Shaikh, S.; Gyorke, S.; Periasamy, M. The Catecholaminergic Polymorphic Ventricular Tachycardia Mutation R33Q Disrupts the N-Terminal Structural Motif That Regulates Reversible Calsequestrin Polymerization. *J. Biol. Chem.* **2010**, *285* (22), 17188–17196. https://doi.org/10.1074/jbc.M109.096354.

(25) Lewis, K.; Munske, G.; Byrd, S.; Kang, J.; Cho, H.-J.; Ríos, E.; Kang, C. Characterization of Post-Translational Modifications to Calsequestrins of Cardiac and Skeletal Muscle. *Int. J. Mol. Sci.* **2016**, *17* (9), 1539. https://doi.org/10.3390/ijms17091539.

(26) Sanchez, E. J.; Lewis, K. M.; Munske, G. R.; Nissen, M. S.; Kang, C. Glycosylation of Skeletal Calsequestrin. *J. Biol. Chem.* **2012**, *287* (5), 3042–3050. https://doi.org/10.1074/jbc.M111.326363.

(27) Pollak, A. J.; Liu, C.; Gudlur, A.; Mayfield, J. E.; Dalton, N. D.; Gu, Y.; Chen, J.; Heller Brown, J.; Hogan, P. G.; Wiley, S. E.; Peterson, K. L.; Dixon, J. E. A Secretory Pathway Kinase Regulates Sarcoplasmic Reticulum Ca2+ Homeostasis and Protects against Heart Failure. *eLife* **2018**, *7*, e41378. https://doi.org/10.7554/eLife.41378.

(28) Cala, S. E.; Jones, L. R. Phosphorylation of Cardiac and Skeletal Muscle Calsequestrin Isoforms by Casein Kinase II. Demonstration of a Cluster of Unique Rapidly Phosphorylated Sites in Cardiac Calsequestrin. *J. Biol. Chem.* **1991**. https://doi.org/10.1016/s0021-9258(18)52447-9.

(29) Bal, N. C.; Jena, N.; Chakravarty, H.; Kumar, A.; Chi, M.; Balaraju, T.; Rawale, S. V.; Rawale, J. S.; Sharon, A.; Periasamy, M. The C-Terminal Calcium-Sensitive Disordered

Motifs Regulate Isoform-Specific Polymerization Characteristics of Calsequestrin. *Biopolymers* **2015**, *103* (1), 15–22. https://doi.org/10.1002/bip.22534.

(30) Holehouse, A. S.; Kragelund, B. B. The Molecular Basis for Cellular Function of Intrinsically Disordered Protein Regions. *Nat. Rev. Mol. Cell Biol.* **2024**, *25* (3), 187–211. https://doi.org/10.1038/s41580-023-00673-0.

(31) Uversky, V. N. Intrinsically Disordered Proteins and Their "Mysterious" (Meta)Physics. *Front. Phys.* **2019**, *7*, 10. https://doi.org/10.3389/fphy.2019.00010.

(32) Flock, T.; Weatheritt, R. J.; Latysheva, N. S.; Babu, M. M. Controlling Entropy to Tune the Functions of Intrinsically Disordered Regions. *Curr. Opin. Struct. Biol.* **2014**. https://doi.org/10.1016/j.sbi.2014.05.007.

(33) Scott, B. T.; Simmerman, H. K.; Collins, J. H.; Nadal-Ginard, B.; Et., A. Complete Amino Acid Sequence of Canine Cardiac Calsequestrin Deduced by cDNA Cloning. *J. Biol. Chem.* **1988**. https://doi.org/10.1016/s0021-9258(18)68401-7.

(34) Beard, N. A.; Wei, L.; Cheung, S. N.; Kimura, T.; Varsányi, M.; Dulhunty, A. F. Phosphorylation of Skeletal Muscle Calsequestrin Enhances Its Ca2+ Binding Capacity and Promotes Its Association with Junctin. *Cell Calcium* **2008**, *44* (4), 363–373. https://doi.org/10.1016/j.ceca.2008.01.005.

(35) Zhang, L.; Kelley, J.; Schmeisser, G.; Kobayashi, Y. M.; Jones, L. R. Complex Formation between Junctin, Triadin, Calsequestrin, and the Ryanodine Receptor. *J. Biol. Chem.* **1997**, *272* (37), 23389–23397. https://doi.org/10.1074/jbc.272.37.23389.

(36) Kobayashi, Y. M.; Alseikhan, B. A.; Jones, L. R. Localization and Characterization of the Calsequestrin-Binding Domain of Triadin 1. *J. Biol. Chem.* **2000**. https://doi.org/10.1074/jbc.m002091200.

(37) Shin, D. W.; Ma, J.; Kim, D. H. The *Asp*-rich Region at the Carboxyl-terminus of Calsequestrin Binds to Ca^{2+} and Interacts with Triadin. *FEBS Lett.* **2000**. https://doi.org/10.1016/s0014-5793(00)02246-8.

(38) Rossi, D.; Lorenzini, S.; Pierantozzi, E.; Van Petegem, F.; Osamwonuyi Amadsun, D.; Sorrentino, V. Multiple Regions within Junctin Drive Its Interaction with Calsequestrin-1 and Its Localization to Triads in Skeletal Muscle. *J. Cell Sci.* **2022**, *135* (2), jcs259185. https://doi.org/10.1242/jcs.259185.

(39) Beard, N. A.; Dulhunty, A. F. C-Terminal Residues of Skeletal Muscle Calsequestrin Are Essential for Calcium Binding and for Skeletal Ryanodine Receptor Inhibition. *Skelet. Muscle* **2015**. https://doi.org/10.1186/s13395-015-0029-7.

(40) Wei, L.; Hanna, A. D.; Beard, N. A.; Dulhunty, A. F. Unique Isoform-Specific Properties of Calsequestrin in the Heart and Skeletal Muscle. *Cell Calcium* **2009**. https://doi.org/10.1016/j.ceca.2009.03.006.

(41) Terentyev, D.; Nori, A.; Santoro, M.; Viatchenko-Karpinski, S.; Kubalova, Z.; Gyorke, I.; Terentyeva, R.; Vedamoorthyrao, S.; Blom, N. A.; Valle, G.; Napolitano, C.; Williams, S. C.; Volpe, P.; Priori, S. G.; Gyorke, S. Abnormal Interactions of Calsequestrin With the Ryanodine Receptor Calcium Release Channel Complex Linked to Exercise-Induced Sudden Cardiac Death. *Circ. Res.* **2006**, *98* (9), 1151–1158. https://doi.org/10.1161/01.RES.0000220647.93982.08.

(42) Rizzi, N.; Liu, N.; Napolitano, C.; Nori, A.; Turcato, F.; Colombi, B.; Bicciato, S.; Arcelli, D.; Spedito, A.; Scelsi, M.; Villani, L.; Esposito, G.; Boncompagni, S.; Protasi, F.; Volpe, P.; Priori, S. G. Unexpected Structural and Functional Consequences of the R33Q Homozygous Mutation in Cardiac Calsequestrin: A Complex Arrhythmogenic Cascade in a Knock In Mouse Model. *Circ. Res.* **2008**, *103* (3), 298–306. https://doi.org/10.1161/CIRCRESAHA.108.171660.

(43) Qin, J.; Valle, G.; Nani, A.; Nori, A.; Et., A. Luminal Ca2+ Regulation of Single Cardiac Ryanodine Receptors: Insights Provided by Calsequestrin and Its Mutants. *J. Gen. Physiol.* **2008**. https://doi.org/10.1085/jgp.200709907.

(44) Priori, S. G.; Mazzanti, A.; Santiago, D. J.; Kukavica, D.; Trancuccio, A.; Kovacic, J. C. Precision Medicine in Catecholaminergic Polymorphic Ventricular Tachycardia. *J. Am. Coll. Cardiol.* **2021**, *77* (20), 2592–2612. https://doi.org/10.1016/j.jacc.2020.12.073.

(45) Priori, S. G.; Chen, S. R. W. Inherited Dysfunction of Sarcoplasmic Reticulum Ca $^{2+}$ Handling and Arrhythmogenesis. *Circ. Res.* **2011**. https://doi.org/10.1161/circresaha.110.226845.

(46) Ng, K.; Titus, E. W.; Lieve, K. V.; Roston, T. M.; Et., A. An International Multicenter Evaluation of Inheritance Patterns, Arrhythmic Risks, and Underlying Mechanisms of *CASQ2* -Catecholaminergic Polymorphic Ventricular Tachycardia. *Circulation* **2020**. https://doi.org/10.1161/circulationaha.120.045723.

(47) Gray, B.; Bagnall, R. D.; Lam, L.; Ingles, J.; Turner, C.; Haan, E.; Davis, A.; Yang, P.-C.; Clancy, C. E.; Sy, R. W.; Semsarian, C. A Novel Heterozygous Mutation in Cardiac Calsequestrin Causes Autosomal Dominant Catecholaminergic Polymorphic Ventricular Tachycardia. *Heart Rhythm* **2016**, *13* (8), 1652–1660. https://doi.org/10.1016/j.hrthm.2016.05.004.

(48) Valle, G.; Galla, D.; Nori, A.; Priori, S. G.; Et., A. Catecholaminergic Polymorphic Ventricular Tachycardia-Related Mutations R33Q and L167H Alter Calcium Sensitivity of Human Cardiac Calsequestrin. *Biochem. J.* **2008**. https://doi.org/10.1042/bj20080163.

(49) Wleklinski, M. J.; Kryshtal, D. O.; Kim, K.; Parikh, S. S.; Blackwell, D. J.; Marty, I.; Iyer, V. R.; Knollmann, B. C. Impaired Dynamic Sarcoplasmic Reticulum Ca Buffering in Autosomal Dominant CPVT2. *Circ. Res.* **2022**, *131* (8), 673–686. https://doi.org/10.1161/CIRCRESAHA.121.320661.

(50) McFarland, T. P.; Milstein, M. L.; Cala, S. E. Rough Endoplasmic Reticulum to Junctional Sarcoplasmic Reticulum Trafficking of Calsequestrin in Adult Cardiomyocytes. *J. Mol. Cell. Cardiol.* **2010**, *49* (4), 556–564. https://doi.org/10.1016/j.yjmcc.2010.05.012.

(51) Hollingsworth, S. A.; Dror, R. O. Molecular Dynamics Simulation for All. *Neuron* **2018**. https://doi.org/10.1016/j.neuron.2018.08.011.

(52) Henriques, J.; Skepö, M. Molecular Dynamics Simulations of Intrinsically Disordered Proteins: On the Accuracy of the TIP4P-D Water Model and the Representativeness of Protein Disorder Models. *J. Chem. Theory Comput.* **2016**, *12* (7), 3407–3415. https://doi.org/10.1021/acs.jctc.6b00429.

(53) Piana, S.; Donchev, A. G.; Robustelli, P.; Shaw, D. E. Water Dispersion Interactions Strongly Influence Simulated Structural Properties of Disordered Protein States. *J. Phys. Chem. B* **2015**, *119* (16), 5113–5123. https://doi.org/10.1021/jp508971m.

(54) Huang, J.; MacKerell, A. D. Force Field Development and Simulations of Intrinsically Disordered Proteins. *Curr. Opin. Struct. Biol.* **2018**. https://doi.org/10.1016/j.sbi.2017.10.008.

(55) Grotz, K. K.; Schwierz, N. Optimized Magnesium Force Field Parameters for Biomolecular Simulations with Accurate Solvation, Ion-Binding, and Water-Exchange Properties in SPC/E, TIP3P-Fb, TIP4P/2005, TIP4P-Ew, and TIP4P-D. *J. Chem. Theory Comput.* **2022**, *18* (1), 526–537. https://doi.org/10.1021/acs.jctc.1c00791.

(56) Kasahara, K.; Terazawa, H.; Takahashi, T.; Higo, J. Studies on Molecular Dynamics of Intrinsically Disordered Proteins and Their Fuzzy Complexes: A Mini-Review. *Comput. Struct. Biotechnol. J.* **2019**, *17*, 712–720. https://doi.org/10.1016/j.csbj.2019.06.009.

(57) Correia, B. E.; Holmes, M. A.; Huang, P.-S.; Strong, R. K.; Schief, W. R. High-Resolution Structure Prediction of a Circular Permutation Loop. *Protein Sci. Publ. Protein Soc.* **2011**, *20* (11), 1929–1934. https://doi.org/10.1002/pro.725.

(58) Phillips, J. C.; Braun, R.; Wang, W.; Gumbart, J.; Tajkhorshid, E.; Villa, E.; Chipot, C.; Skeel, R. D.; Kalé, L.; Schulten, K. Scalable Molecular Dynamics with NAMD. *J. Comput. Chem.* **2005**, *26* (16), 1781–1802. https://doi.org/10.1002/jcc.20289.

(59) Jorgensen, W. L.; Chandrasekhar, J.; Madura, J. D.; Impey, R. W.; Klein, M. L. Comparison of Simple Potential Functions for Simulating Liquid Water. *J. Chem. Phys.* **1983**, *79* (2), 926–935. https://doi.org/10.1063/1.445869.

(60) Humphrey, W.; Dalke, A.; Schulten, K. VMD: Visual Molecular Dynamics. *J. Mol. Graph.* **1996**, *14* (1), 33–38. https://doi.org/10.1016/0263-7855(96)00018-5.

(61) Hopkins, C. W.; Le Grand, S.; Walker, R. C.; Roitberg, A. E. Long-Time-Step Molecular Dynamics through Hydrogen Mass Repartitioning. *J. Chem. Theory Comput.* **2015**, *11* (4), 1864–1874. https://doi.org/10.1021/ct5010406.

(62) Roe, D. R.; Cheatham, T. E. PTRAJ and CPPTRAJ: Software for Processing and Analysis of Molecular Dynamics Trajectory Data. *J. Chem. Theory Comput.* **2013**, *9* (7), 3084–3095. https://doi.org/10.1021/ct400341p.